Technical Report

TR-10-70

Inspection of copper canisters for spent nuclear fuel by means of ultrasound

Algorithms for ultrasonic imaging

Tadeusz Stepinski (editor), Marcus Engholm,
Tomas Olofsson
Uppsala University, Signals and Systems,
Department of Technical Sciences, Sweden

July 2011

Svensk Kärnbränslehantering AB
Swedish Nuclear Fuel
and Waste Management Co

Box 250, SE-101 24 Stockholm
Phone +46 8 459 84 00

ISSN 1404-0344
SKB TR-10-70

Inspection of copper canisters for spent nuclear fuel by means of ultrasound

Algorithms for ultrasonic imaging

Tadeusz Stepinski (editor), Marcus Engholm,
Tomas Olofsson
Uppsala University, Signals and Systems,
Department of Technical Sciences, Sweden

July 2011

Abstract

This report contains research results concerning the use of advanced ultrasound for the inspection of copper canisters for spent nuclear fuel obtained at Signals and Systems, Uppsala University in 2009 and 2010.

The first part of the report deals with ultrasonic imaging of damage in planar structures using Lamb waves. We present results of the first successful attempt to apply an adaptive beamformer for Lamb waves. Our algorithm is an extension of the adaptive beamformer based on minimum variance distortionless response (MVDR) approach to dispersive, multimodal Lamb waves. We present simulation and experimental results illustrating the performance of the MVDR applied to imaging artificial damage in an aluminum plate..

In the second part of the report we present two extensions of the previously proposed 2D phase shift migration algorithms for enhancing resolution in ultrasonic imaging of solid objects. The first extension enables processing 3D data in order to fully utilize the resolution enhancement potential of the technique. The second extension, consists in generalizing the technique to allow for the processing of data acquired using an array instead of a previously concerned single transducer. Robustness issue related to objects having front surfaces that are slightly tilted relative to the scanning axis is also considered.

Contents

Chapter 1

Introduction

by Tadeusz Stepinski

In this report we are presenting our recent research results concerning ultrasonic inspection of copper canisters for spent nuclear fuel.

Our research activity in this project in 2009/10 was split into two separate tasks that are reported in the following chapters:

- Beamforming of Lamb waves using ultrasonic arrays, and
- Computationally efficient 3D image reconstruction using array data.

The first chapter deals with ultrasonic imaging of damage in planar structures using a special type of guided waves, known as Lamb waves. Lamb waves are guided waves that propagate in plate structures; in a plate the two free surfaces of the plate 'guide' the waves within its borders. In general, when a Lamb wave is incident on a structural discontinuity (which has a size comparable to its wavelength), it is scattered in all directions. When the scattered wave field is sensed by a transducer the information about the damage can be extracted from various characteristics of the received signal, such as delay in time of transit, amplitude, frequency content, etc. Lamb waves are very useful for monitoring large areas from a fixed position due to their ability to propagate over a long distance. Lamb waves, however, have disadvantages that stem from their guided nature, they are dispersive and can propagate in the form of multiple modes with different velocities. Those features seriously complicate interpretation of the backscattered signals, which calls for using advanced beamforming techniques for damage detection and characterization. An adaptive beamformer, base on the minimum variance distortionless response (MVDR) approach, modified for the dispersive, multimodal waves is presented in this chapter. We present experimental results of the first successful attempt to apply an adaptive beamformer for Lamb waves. Part of the results from this chapter is included in two papers accepted for publication in two journals: An International Journal of Structural Health Monitoring (Sage), and IEEE Transactions on Ultrasonics, Ferroelectrics and Frequency Control (UFFC), 2010.

In the second chapter we present results of further investigation of phase shift migration presented in our previous report TR-09-28. We implemented migration techniques that were originally developed in seismic exploration for the examination of the Earth's interior, to ultrasonic data. Migration is an advanced postprocessing technique which offers possibility of improving spatial resolution when imaging multilayered media. We consider the immersion ultrasonic test setup for which time domain methods, such as SAFT, are cumbersome to use due to the refraction at the layer interfaces. Previously, we considered phase shift migration for 2D reconstructions using a single scanned transducer. Here, we extend our algorithm from 2D to 3D data in order to fully utilize the resolution enhancement potential of the technique. Part of the results from this chapter is included in the paper that has been accepted for publication in IEEE Transactions on UFFC, 2010

Chapter 2

Beamforming of Lamb waves using ultrasonic arrays

by Marcus Engholm, Tadeusz Stepinski and Tomas Olofsson

2.1 Introduction

Guided waves in structures allow inspection of large areas from a fixed position. Areas which are not accessible using traditional NDT methods, such as eddy current or bulk wave pulse-echo ultrasound, can potentially be inspected or monitored using guided waves. Examples of applications for guided waves are the inspection of piping [1] and plates [2].

Guided waves in plates, also known as Lamb waves, share fundamental properties with other types of guided waves, such as, dispersion and the existence of multiple propagating modes. Dispersion causes the signal to spread out which reduces the spatial and temporal resolution of the received unprocessed data, a significant issue in applications where range is to be estimated. Furthermore, Lamb modes differ in dispersion characteristics and propagate at different velocities making interpretation of backscattered signals complicated in the presence of multiple modes. Overlapping modes can make identification of small defects and time-of-flight estimation difficult.

During the last decade the use of active Lamb wave arrays for imaging of larger plate areas has been proposed by several authors [3–8]. One or more elements in the array generate a pulse that propagates along the plate. The backscattered signals from defects and other discontinuities are received by the array and post-processed to form an image of the reflectors in the plate. As for other guided wave applications, reduction of interference from other modes is of major importance. Proper design of transducers used for excitation and detection in combination with careful frequency selection can significantly reduce the influence from interfering modes. Omni-directionality is essential for most array applications and requires special consideration in the array element design. Some examples presented in the field include the use of electro-mechanical acoustic transducers (EMAT) [5, 9], and piezoelectric transducers [6, 10]. The drawback of these approaches is that they require limited bandwidth input signals to work efficiently. Limited bandwidth leads to reduced range resolution since the length of the signal increases.

The effect of dispersion can be reduced by selecting a frequency region with relatively low dispersion or using dispersion compensation scheme. Wilcox showed that by using theoretically calculated dispersion curves, time domain data can be transformed into dispersion compensated spatial domain data over a wider frequency range for a single mode [5, 11].

The above cited works, in common with most other work presented in the literature concerning array processing of Lamb waves, have been focused on the standard beamformer (SBF). The standard beamformer is robust, easy to implement, and computationally simple. However, compared to more advanced array processing methods it suffers from poor resolution and high sidelobes. In [5] a deconvolution approach based on the simulated point-spread function was used to reduce the sidelobe level. A more general approach to beamformer design was proposed by Velichko and Wilcox in [12]. However, neither of these methods are data dependent and will therefore assume the worst case scenario: signals are assumed to impinging from all directions. This will lead to a suboptimal use of the available degrees of freedom in the weight vector. If knowledge of the actual interferers was available, an optimal weight vector could be derived to much more efficiently cancel interferers. Such methods are known as adaptive beamformers, and have not been used in Lamb wave applications.

Adaptive beamformers have been successfully utilized in, for example, radar, sonar, and medical ultrasound applications, resulting in improved resolution and interference suppression compared to the SBF. Contrary to the SBF, an adaptive beamformer is optimized based on some data criterion, such as minimizing the influence of interfering signals in the received data. One of the most commonly used adaptive beamformers is based on the minimum variance distortionless response (MVDR) approach. Previous work on the MVDR approach in the medical ultrasound field include Wang [13] et al., Sasso and Cohen-Bacrie [14], and Synnevåg et al. [15]. Another,

but not entirely related, approach using the MVDR method for Lamb wave processing was proposed by Michaels et al. [16] for processing change based data from a distributed array in a tomographic setup.

In [17–19], the MVDR approach was compared by the authors to a SBF for passive direction-of-arrival (DOA) estimation of Lamb waves, which showed that the MVDR approach performs much better in terms of resolution and sidelobe level. The work was extended to a complete active imaging procedure [20], where a single transmitter and a fixed array of receivers was used to inspect a plate. The MVDR beamformer (MVBF) showed much better resolution and suppression of the interfering Lamb modes compared to the SBF. The improved suppression of interfering Lamb modes, may relax requirements on array element design and bandwidth of the input signals. However, the most significant drawback of the MVDR approach is its inability to handle correlated sources. This is especially true for active imaging setups, where the backscattered signals are likely to be highly correlated. This in turn puts some constraints on the geometry of the array and limited the effective aperture size.

In this chapter a MVDR approach for Lamb wave imaging is introduced capable of working in the highly correlated environment of an active setup. The basic steps of the method follows the approach used in medical ultrasound by Sasso and Cohen-Bacrie [14], Synnevåg et al. [15], and others. Here, the technique is extended to handle dispersion and two-dimensional arrays. The motivation for using this approach is its high resolution and its ability to adaptively suppress interfering signals from other defects and from other propagating Lamb modes. Efficient suppression of interfering modes may relax the requirements on transducer design and limitations in signal bandwidth. Setups with single transmitter and multiple transmitters array are considered separately. The approach employing a single transmitter, requires certain preprocessing to achieve the desired result. The use of multiple transmitters avoids the need for preprocessing, which enables more flexibility in array design, and can lead to improved performance compared to single transmitter setups.

The chapter is organized as follows: the problem is formulated in Sec. 2.2, where a short overview of the relevant properties of Lamb waves along with an introduction to the MVDR approach is also presented. Details concerning the MVDR algorithms are given in Sec. 2.4. The performance of the proposed method compared to the SBF is evaluated in Sec. 2.5. Two scenarios are considered: first, simulation results of the mode suppression capabilities of three different array configurations are presented, followed by the simulation and experimental results of a plate inspection scenario. Finally, conclusions are formulated in Sec. 2.6.

2.2 Problem formulation

This work considers the monitoring of thin plates through pulse-echo ultrasonic imaging using guided Lamb waves. The imaging covers 360°, in both near-field and far-field using a rectangular array. Two cases illustrated in Fig. 2.1 are considered:

- A single transmitter located at $\mathbf{z}_t = [x_t, y_t]^T$, that may be an array element or a separate transducer, insonifies the plate using a short pulse or a time-windowed sinusoid. The resulting waves are reflected back from boundaries and defects and the backscattered field is acquired by all array elements.
- Elements of a 2D array capable of generation and reception of Lamb waves are used sequentially to insonifiy the plate using a short pulse or a time-windowed sinusoid. Data are acquired from the successive excitations of the transmitting elements in the array and the reception is performed using all the receiving array elements.

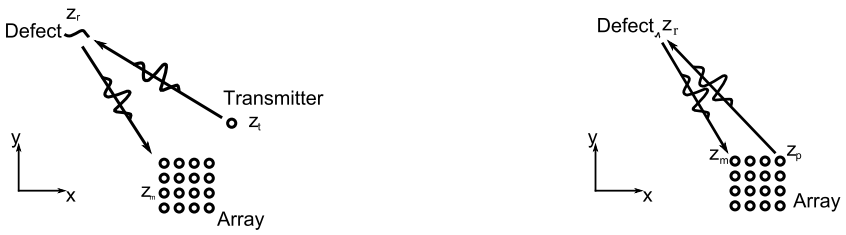

Figure 2.1: Overview of the imaging problem. Single transmitter and 4x4 rectangular matrix of receivers (left) and 4x4 rectangular active array with current transmitter $\mathbf{z}_p$ and receiver $\mathbf{z}_m$ (right). A scatterer is located at $\mathbf{z}_r$.

The objective in both cases is to detect and estimate the size of defects in a plate structure. The acquired data allows an estimation of the reflected power in each point $\mathbf{z} = [x, y]^T$ in the region of interest (ROI) located in the vicinity of the array.

Let $g_{p,m}(t)$ denote the received signal for the p:th transmitter and m:th receiver (for the first case p is equal to 1). Each of the P transmitting elements is excited separately, but the backscattered signals are received by all M receiving elements either simultaneously or multiplexed through repeated transmitter excitation. The approach is general in the sense that either an active array (pulse-echo mode), or a combination of transmitting and receiving arrays (pitch-catch), can be considered. It is assumed that $g_{p,m}(t)$ is an analytic (complex) signal, hence, all negative frequency components are zero.

The dispersive and multi-modal properties of the propagating Lamb waves need to be addressed to achieve adequate results. Omni-directional coverage in both near- and far-field of the array is desirable to fully utilize the array. The results presented below have been acquired using uniform rectangular arrays (URAs). However, the method is not restricted to any particular array configuration.

2.3 Theoretical background

2.3.1 Lamb waves

To perform imaging using Lamb waves over a wide frequency band, the dispersive properties of the Lamb waves need to be addressed. A necessary step in both simulation and compensation of dispersion is the estimation of the theoretical dispersion characteristics of the monitored structure. If accurate estimates of the material properties of the object are available, the dispersion characteristics can be determined by solving the Rayleigh-Lamb frequency equations. For homogeneous isotropic plates the wavenumber at angular frequency ω, $k(\omega)$, can be calculated by solving the Rayleigh-Lamb frequency equations [21],

$$\frac{\tan(qd/2)}{\tan(pd/2)} = -\frac{4k^2(\omega)pq}{(q^2 - k^2(\omega))^2} \quad \text{for symmectric modes,} \tag{2.1}$$

$$\frac{\tan(qd/2)}{\tan(pd/2)} = -\frac{(q^2 - k^2(\omega))^2}{4k^2(\omega)pq} \quad \text{for antisymmectric modes,} \tag{2.2}$$

where d is the thickness of the plate, $p^2 = (\omega/c_L)^2 - k^2(\omega)$, and $q^2 = (\omega/c_S)^2 - k^2(\omega)$, c_L is the longitudinal bulk wave velocity and c_S is the shear bulk wave velocity of the material. An

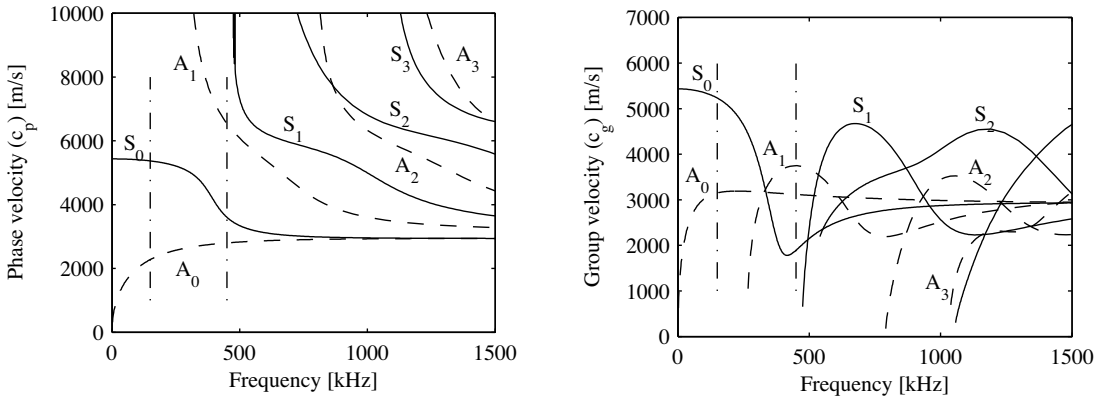

Figure 2.2: Dispersion curves for a 6 mm Al plate. Phase velocity (left) and group velocity (right). Solid lines (S_0,S_1, ...) - symmetric modes. Dashed line (A_0,A_1, ...) - asymmetric modes. Dash-dot lines show the frequency band of the signal used in experiments in Sec. 2.5.

example of the theoretical dispersion curves calculated for the 6 mm aluminium plate is shown in Figure 2.2.

Another possibility is to experimentally estimate the dispersion using, for example, the 2D FFT approach proposed by Alleyne and Cawley [22]. This can be particularly valuable for complex structures, and for evaluating the response of the array elements in terms of mode excitation.

Depending on the frequency of the signal and the thickness of the plate, the number of Lamb modes may range from two to infinity. The Lamb modes are named S_0, S_1, ... for symmetric modes, and A_0, A_1, ... for antisymmetric modes. In the following sections a simple index, $n = 0, 1, 2, 3, \ldots$, is used to identify modes S_0, A_0, S_1, A_1, ... The frequency dependent wavenumber of the n-th mode is denoted $k_n(\omega)$.

Directionality of arrays

Arrays are commonly used as spatial filters enabling directional resolution. 1D arrays, such as uniform linear arrays (ULA), where all array elements are uniformly distributed on a line, offer at best 180° azimuthal coverage. Furthermore, the performance of a ULA in terms of angular resolution is highly dependent on the azimuth. 2D arrays on the other hand, offer 360° azimuthal coverage. Examples of most common 2D array configurations are circular and rectangular arrays.

The most fundamental model of an array is the *array steering vector* or the *array manifold vector*. The steering vector consists of phasors producing the phase-shifts corresponding to the propagation over the array for a particular wavenumber (k_x, k_y). Thus, the steering vectors represent an array for a single mode at a particular frequency and incident angle.

Although the steering vector is not used explicitly in the algorithm, it will be used as when describing the basic theory of the MVBF. The steering vector for a rectangular array can be constructed by stacking rows of ULA steering vectors [23]. Let the steering vector for the m_r:th row be

$$\mathbf{a}_{m_r}(k_x, k_y) = \left[e^{jm_r k_y d} \quad e^{j(k_x d + m_r k_y d)} \quad \ldots \quad e^{j((M_c-1)k_x d + m_r k_y d)} \right]^T. \tag{2.3}$$

where d is the element spacing and M_c the number of columns.

For a URA built of M_c columns and M_r rows, the stacked steering vector takes the following

form

$$\mathbf{a}(k_x, k_y) = \begin{bmatrix} \mathbf{a}_0(k_x, k_y) \\ \vdots \\ \mathbf{a}_{M_r-1}(k_x, k_y) \end{bmatrix}. \tag{2.4}$$

For Lamb waves, array steering is performed by matching the phase shifts corresponding to a particular mode's dispersion characteristics for a given frequency. The signals from the array elements are aligned to coherently sum signals that match a selected direction and mode. Other modes and directions will not add up constructively which should result in their suppression.

The normalized output from a SBF to wavenumber (k_x, k_y), assuming a narrowband[1] signal is

$$y(t) = \frac{1}{M}\mathbf{a}^H(k_x, k_y)\mathbf{x}(t), \tag{2.5}$$

where $\mathbf{x}(t) = [x_0(t)\, x_1(t)\, \ldots\, x_M(t)]^T$ contains the signals received by the M array elements, and ^{H} denotes the conjugate transpose. For SBFs it is common to apply some weight function on the array elements to reduce the sidelobe level, so called apodization. Therefore a more general description of the beamformer is

$$y(t) = \mathbf{w}^H\mathbf{x}(t) \tag{2.6}$$

where $\mathbf{w}$ is the weight (apodization) vector. Apodization is normally used in beamformers to suppress sidelobes. The weight vector of a SBF is simply a weighted steering vector, which is completely independent of the received signal. By contrast, adaptive beamformers, such as the MVBF, form data dependent weight vectors according to some predefined criterion.

Beamforming of broadband signals is performed either in time domain, where delays are used to align the signals from a particular direction, or by processing each frequency component separately and superimposing the results.

Mode suppression

Besides dispersion, the interference from multiple propagating modes creates difficulties when interpreting Lamb wave measurement data. The backscattered signal from a defect can consist of multiple dispersed modes arriving at different times, which could be misinterpreted as defects, overlap weaker defects, and make time-of-flight estimation difficult.

As discussed earlier, a 2D array is required for 360° coverage, but as it will be explained below, 2D arrays offer another advantage over 1D arrays which is highly relevant for Lamb waves.

Consider two different overlapping plane wave Lamb modes impinging on a ULA from 0°, as illustrated in Fig. 2.3. The modes have different wavenumbers and propagate at different velocities. Unless there is *a priori* information available concerning the shape and propagation of the modes, these are obviously impossible to separate for any beamformer. The reason is that all the array elements are approximately at the same distance to the source, in other words, all modes have the same steering vector for this angle, the unit vector $\mathbf{1}$. A 2D array, on the other hand, allows separation since its elements are at different distances from the target and non-focused modes will therefore not add up coherently. SBFs rely completely on this concept which, to work efficiently, requires relatively many array elements. The benefits of using adaptive beamformers is that they allow much more efficient use of the limited array size. Examples illustrating this are presented in Section 2.5.

[1] An impinging signal is considered narrowband if the signal's complex envelope is approximately constant during its propagation over the array.

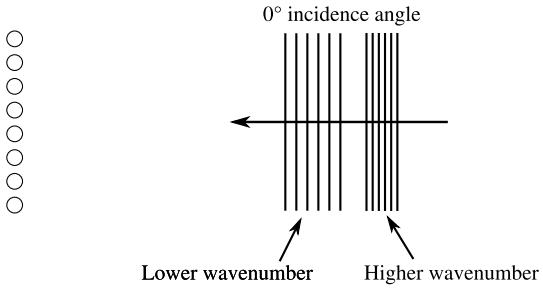

Figure 2.3: Two Lamb modes with different wavenumber impinging on a ULA.

Mode conversion

When a Lamb wave is reflected or transmitted at a boundary, some of the energy of the particular incoming Lamb mode may be converted into other modes. Depending on the characteristics of the boundary, and the frequency content of the impinging Lamb wave, the conversion is possible between modes of different order, e.g. A_0 to A_1, as well as between antisymmetric and symmetric modes [21]. Thus, a signal received as a particular mode may be the result of any other mode propagating from the transmitting transducer to the boundary at a different velocity. A few simulation examples featuring mode conversion will also be presented in Section 2.5.

Simulation model

To enable evaluation of the MVBF compared to the SBF under ideal conditions, a simplified simulation model has been used. The model simulates multiple reflections of two propagating modes impinging on the array, the S_0 and A_0 mode.

In practice, the excitation of a particular mode depends both on the transducer and the excitation frequency. Here, it is simply assumed that both modes have been excited and the resulting out-of-plane surface displacement is $T(\omega)$ for both modes. Further, assume that there are R pointscatterers in the plate that scatter incident waves equally in all directions and that no secondary scattering occurs. The transmitting elements $p = 1 \dots P$, act as omnidirectional pointsources, and are excited individually. Let $G_{p,m}(\omega)$ denote the signal received by array element m from an excitation of transmitter p. The received signals from a scatterer are given by the sum of the two modes and the corresponding phase-shifts due to dispersion in the path from the transmitting array element p, to the reflector r, and back to the receiving element m. The resulting signals are superpositions of the contributions from the R reflectors

$$G_m(\omega) = \sum_{r=1}^{R} \sum_{n=0}^{1} \frac{1}{\sqrt{z_{r,p} z_{r,m}}} R_{r,n} T(\omega) e^{-jk_n(\omega),(z_{r,p}+z_{r,m})} \tag{2.7}$$

where the distances, $z_{r,p} = \|\mathbf{z}_r - \mathbf{z}_p\|$, and $z_{r,m} = \|\mathbf{z}_r - \mathbf{z}_m\|$, are the scatterer–transmitter and scatterer-receiver distance, respectively, and $\mathbf{z}_r$, $\mathbf{z}_m$, and $\mathbf{z}_p$, shown in Fig. 2.1, are the positions of the scatterer, the receiver, and the transmitter, respectively. The frequency independent reflection coefficient for reflector r and mode n is denoted $R_{r,n}$. The first factor in (2.7) is due to the divergence of the cylindrical waves from the point-sources and point-scatterers.

For the case with mode conversion, where some of the power of mode n is converted into another mode n' at the reflector, the expression in the sum (2.7) becomes

$$R_{r,nn'} T(\omega) e^{-j(k_n(\omega) z_{r,p} + k_{n'}(\omega) z_{r,m})} \tag{2.8}$$

where $R_{r,nn'}$ is the amplitude of the converted mode at reflector r, and $k_{n'}(\omega)$ the wavenumber of mode n'.

2.3.2 Minimum Variance Distortionless Response beamformer

Contrary to the SBF explained in Sec 2.3.1, the MVBF beamformer is capable of adaptive suppression of interfering signals and modes. To achieve this it requires information on the noise and interference environment in the form of the spatial covariance matrix. The elements of the spatial covariance matrix are the interelement covariance estimates of the signals received by the array. The estimation of the covariance matrix is the most critical step in the MVDR approach and its accuracy has significant impact on the final result.

Before proceeding to the broadband implementation of the MVBF used in this work, the narrowband MVBF is reviewed. A narrowband signal assumption leads to the basic formulation of the MVBF, which is the most common in the literature.

A covariance matrix estimate using N_s samples of the vector $\mathbf{x}(t)$ is given by

$$\widehat{\mathbf{R}} = \frac{1}{N_s} \sum_{t=1}^{N_s} \mathbf{x}(t)\mathbf{x}^H(t). \tag{2.9}$$

The MVDR method, also known as Capon's method, was originally proposed for frequency-wavenumber estimation of seismic waves [24]. The MVDR method sets a data dependent weight vector which minimizes the influence of interfering signals while passing the desired signal undistorted.

The weight vector $\mathbf{w}$ of the MVBF is designed so that the signals with the wavenumber (k_x, k_y) are to be passed with gain 1, i.e., $\mathbf{w}^H\mathbf{a}(k_x, k_y) = 1$, while the output power from the array, $P(k_x, k_y) = \mathbf{w}^H\mathbf{R}\mathbf{w}$ is minimized. This means that the resulting weight vector will minimize the influence of interferers. The solution to this optimization problem is simply [25]

$$\mathbf{w}(k_x, k_y) = \frac{\widehat{\mathbf{R}}^{-1}\mathbf{a}(k_x, k_y)}{\mathbf{a}^H(k_x, k_y)\widehat{\mathbf{R}}^{-1}\mathbf{a}(k_x, k_y)}, \tag{2.10}$$

and the corresponding estimated power of the signal with the wavenumber (k_x, k_y) is

$$P_{MVDR}(k_x, k_y) = \frac{1}{\mathbf{a}^H(k_x, k_y)\widehat{\mathbf{R}}^{-1}\mathbf{a}(k_x, k_y)}. \tag{2.11}$$

The MVBF in its standard form, similarly to many other advanced array processing methods, assumes narrowband signals. Furthermore, it is not able to separate backscattered signals, since they are typically correlated, which may result in so-called signal cancellation [26]. This manifests itself as the suppression and spatial perturbation of the relevant signal by the beamformer. Another major disadvantage of the MVBF is that it is sensitive to errors in the steering vector, where even small errors can lead to suppression of the desired signal [27]. The following sections will address those issues.

2.4 Methods

Generally, there are two ways of obtaining high range resolution in imaging: either using using short pulses or long pseudo-random sequences. The first way, which is most commonly used in ultrasonic imaging, requires transmitting broadband signals that, when scattered are received by

the array elements. However, many array processing methods, such as MVBF, are formulated for narrowband signals. Thus, the most straightforward and most commonly used approach to handle broadband signals is to perform the estimation for each frequency separately using the frequency domain version of the covariance matrix, that is, the spectral matrix. The drawback of such an approach is that the correlation between different frequencies of the signal is not utilized. Additionally, a poor signal-to-noise ratio (SNR) leads to high variance in the estimates of the individual narrowband spectral matrices [28]. Furthermore, since broadband signals are typically limited in time, there is a trade-off between the frequency resolution and the number of snapshots used for averaging, which also has a negative impact on the individual spectral matrix estimates. To utilize the broadband nature of the signal a number of preprocessing procedures have been proposed in the literature, for example, the coherent subspace approach [29] and the steered covariance matrix [28].

Signal cancellation can be reduced by using, for example, spatial smoothing [30], which decorrelates the signals and also reduces the variance of the estimated covariance matrix. Spatial smoothing can only be applied on arrays with regular geometries that can be divided into a set of identical subarrays. Furthermore, spatial smoothing reduces the effective aperture size to that of the subarray.

The decorrelating preprocessing step is necessary in passive scenarios, or for setups consisting of only one transmitter, such as the first setup defined in Sec. 2.2. For active arrays setups, where each element can be excited separately, such as the second setup defined in Sec. 2.2, this problem is avoided. The multiple and slightly different snapshots created by the separate element excitations have the same effect as the subarray averaging of the spatial smoothing approach [31], without the reduction in effective aperture size. For setups having significantly fewer transmitters than receivers, a combination of multiple transmitters and spatial smoothing may be considered.

2.4.1 Steered pseudo-covariance matrix

To take advantage of the bandwidth of broadband signals, the steered covariance matrix approach was introduced by Krolik [28] for far-field broadband source localization. The idea is to pre-steer the received data before estimating the covariance matrix (2.9). What is gained by doing so is that all frequency components of a potential broadband signal from the steered direction will have a unit steering vector, $\mathbf{1}$, which allows for a direct application of (2.10) to calculate a broadband adaptive weight vector.

The basic concept of this approach has been applied on near-field data for adaptive beamforming of linear arrays in medical ultrasound by Wang [13] et al., Sasso and Cohen-Bacrie [14] and Synnevåg et al. [15]. In this work this approach is extended to 2D arrays and dispersive signals.

For non-dispersive signals, such as those in the acoustical environment of medical ultrasound, the steering of the received signals prior to calculation of the covariance matrix is performed using delays. The delays are chosen to align potential reflections from a particular point $\mathbf{z}$,

$$\mathbf{h}_p(\mathbf{z}) = \begin{bmatrix} g_0(\tau_0(\mathbf{z})) & g_1(\tau_1(\mathbf{z})) & \cdots & g_{M-1}(\tau_{M-1}(\mathbf{z})) \end{bmatrix}^T, \tag{2.12}$$

where $\tau_m(\mathbf{z})$ is the delay corresponding to the propagation time from the transmit element p to the point $\mathbf{z}$, and back to the receiver m.

Using time delays for broadband dispersive Lamb waves will not lead to coherent alignment the signals since the frequency components propagate at different phase velocities. Instead, the

alignment is obtained by backpropagating the signal $g_{p,m}(t)$, for a particular mode n as [11]

$$h_{p,m,n}(\mathbf{z}) = \sqrt{z_{r,p} z_{r,m}} \sum_{\omega_s} G_{p,m}(\omega_s) e^{jk_n(\omega_s)(z_{r,p}+z_{r,m})} \tag{2.13}$$

where $G_{p,m}(\omega_s)$ is the Fourier transform of the received signal $g_{p,m}(t)$, p denotes the transmitter, and $z_{r,p} = \|\mathbf{z}_r - \mathbf{z}_p\|$ and $z_{r,m} = \|\mathbf{z}_r - \mathbf{z}_m\|$. The first factor compensates for the divergence and the exponential introduces the proper phase-shift to compensate for the dispersion and propagation.

The procedure only compensates for the dispersion and propagation of one mode. Other, interfering modes are not aligned. In the sequel it is assumed that a particular mode is selected, hence the mode index, n, is dropped for notional convenience.

To avoid spatial aliasing, the frequencies used in (2.13) should be limited so that the minimum wavelength for any mode is at least twice the element distance in the array. Assuming that $g_{p,m}(t)$ is a complex (analytical) signal, spectral components above the Nyquist frequency in the discrete Fourier transform are zero. Note that there is risk that other modes wrap-around due to the phase shifts and in such cases the received signals should be zero-padded before processing.

Potential wave attenuation is not compensated for since it is assumed to be small. However, if the attenuation is significant and known, it is straightforward to include a compensating term in (2.13).

To estimate the reflected power from a focus point $\mathbf{z}$, the received signals from all array elements are phase-shifted according to (2.13) to compensate for the propagation and dispersion corresponding to the distance between the transmitter p, the focus point $\mathbf{z}$ and the receiver m. This results in a focused vector

$$\mathbf{h}_p(\mathbf{z}) = [h_{p,1}(\mathbf{z})\ h_{p,2}(\mathbf{z})\ \cdots\ h_{p,M}(\mathbf{z})]^T, \tag{2.14}$$

for each transmitter p. A rank one covariance matrix for transmitter p is

$$\widehat{\mathbf{R}}_p(\mathbf{z}) = \mathbf{h}_p(\mathbf{z})\mathbf{h}_p^H(\mathbf{z}). \tag{2.15}$$

In order to get proper estimate of the covariance matrix is is necessary to have several snapshots. One option is to average over nearby points, analogous to (2.9). However, since broadband signals are considered, which will be spatially confined around the actual scatterer, this may not improve the estimate. A better approach is to utilize the multiple snapshots acquired over the successive transmitter excitations. In addition to improving the estimate of the covariance matrix, it will lead to a decorrelation of the backscattered signals, which was discussed in the beginning of this section.

Let the matrix $\mathbf{H}(\mathbf{z})$ be defined as

$$\mathbf{H}(\mathbf{z}) = [\mathbf{h}_1(\mathbf{z})\ \mathbf{h}_2(\mathbf{z})\ \cdots\ \mathbf{h}_P(\mathbf{z})]. \tag{2.16}$$

The focused covariance matrix can then be estimated as the average of all rank *1* covariance matrices from each transmitter, $\mathbf{h}_p(\mathbf{z})\mathbf{h}_p^H(\mathbf{z})$, as

$$\widehat{\mathbf{R}}(\mathbf{z}) = \frac{1}{P}\mathbf{H}(\mathbf{z})\mathbf{H}^H(\mathbf{z}). \tag{2.17}$$

Thus, each point in the ROI requires a separate covariance matrix which results in more computational effort compared to a conventional covariance matrix. The advantage, however, is that this approach enables processing of dispersed near-field broadband signals, which is not possible using the standard MVDR approach in (2.10).

2.4.2 MVBF

Since the proper phase shifts for steering and dispersion compensation for each frequency are already applied in the steered covariance matrix $\widehat{\mathbf{R}}(\mathbf{z})$, the steering vector for point $\mathbf{z}$ takes simply the form of the unit vector $\mathbf{1}$, which results in the following MVBF weight vector

$$\mathbf{w}(\mathbf{z}) = \frac{\widehat{\mathbf{R}}^{-\mathbf{1}}(\mathbf{z})\mathbf{1}}{\mathbf{1^T}\widehat{\mathbf{R}}^{-\mathbf{1}}(\mathbf{z})\mathbf{1}}. \tag{2.18}$$

Note that if the number of transmitters P is less than the number of receivers M, the covariance matrix (2.17) will be non-invertible. This will be addressed in Section 2.4.4.

The weight vector $\mathbf{w}(\mathbf{z})$ is then applied on the received signals from each excitation and the outputs are subsequently averaged

$$y(\mathbf{z}) = \frac{1}{P}\sum_{p=1}^{P} \mathbf{w}^{\mathrm{H}}(\mathbf{z})\mathbf{h}_{\mathrm{p}}(\mathbf{z}). \tag{2.19}$$

The backpropagation step in (2.13) has already aligned the signals for the particular mode, making the SBF output simply the average of the focused signals

$$y(\mathbf{z}) = \frac{1}{P}\sum_{p=1}^{P} \mathbf{1}^{\mathrm{H}}\mathbf{h}_{\mathrm{p}}(\mathbf{z}). \tag{2.20}$$

Note that apodization can be applied to the SBF by replacing the unit vector by a suitable weight vector.

The steering vector for the steered covariance matrix is constructed with an assumption of equal amplitude over the array elements for the signal of interest. This assumption will affect the behavior of the MVBF approach compared to the SBF in the presence of near-field defects that reflect the transmitted waves in a way that leads to significantly different amplitudes over the array elements. This could typically occur when a defect is oriented in such a way that the reflected energy only reaches some array elements. The SBF will simply produce an output based on the average over the array, while the MVBF could in the worst case cancel the signal. The diagonal loading approach described below, will to some degree increase the MVBF's tolerance to such signals.

2.4.3 Focusing regions

When performing the focusing operation for each element pair $h_{p,m,n}(\mathbf{z})$ in both directions (i.e., transmitter-receiver and receiver-transmitter), the focused range forms an ellipse intersecting the focus point $\mathbf{z}$, where the elements are located in the focal points of each ellipse. Each pair of elements forms a different ellipse, which leads to the problem that the focused signals from different element pairs can potentially contain contributions from different defects. Furthermore, because of the different angles between the transmitters, the scatterers, and the receivers it is possible that a single interfering defect spreads out spatially, which limits the performance of the MVBF. Therefore, the near-field covariance matrices, $\widehat{\mathbf{R}}_p(z)$, from each transmitter p, are not realizations of the same interference environment, which calls for a more appropriate name, a pseudo-covariance matrix. Two examples of such ellipses are illustrated in Fig 2.4.

Although each transmission improves the estimate of the covariance matrix close to the point in focus, the resulting data could include more interferers that could actually reduce the

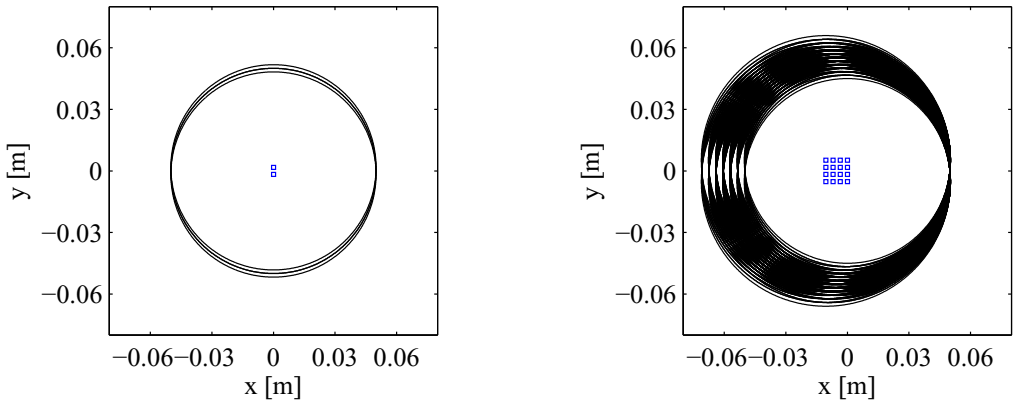

Figure 2.4: Elliptic focusing regions for 2x1 (a) and 4x4 (b) array.

performance of the MVBF. The MVBF is most efficient when there are only a few spatially confined interferers. When the number of interferers increases, it is likely that the adaptive performance is also reduced. This effect can be seen in the simulation results.

Since this issue is aggravated by an increase in the number of transmitters used for averaging in (2.17), one approach to mitigate the problem is to divide the transmitters into L subarrays and perform the estimation using each transmitting subarray l separately. Thus, a weight vector $\mathbf{w}_l(\mathbf{z})$ is calculated using a covariance matrix estimate from only a subset of the transmitters. The outputs, using received data and the weights from the covariance matrix estimates of each subarray, are then averaged

$$y(\mathbf{z}) = \sum_{l=1}^{L} y_l(\mathbf{z}). \tag{2.21}$$

2.4.4 Robustness and rank issues

It is well known that steering vector errors can have a severe effect on the estimate of the MVDR algorithm [27]. This can cause the resulting weight vector to suppress the actual signal instead of the intended unit gain. A common approach to balance adaptive performance and robustness is through diagonal loading of the sample covariance matrix. This is performed by adding a positive constant to the diagonal elements of the covariance matrix

$$\widehat{\mathbf{R}}_{load} = \widehat{\mathbf{R}} + \alpha\mathbf{I}. \tag{2.22}$$

The difficulty is to determine the amount of loading that is appropriate. Using the same approach as in [15], α is set as

$$\alpha = \frac{1}{\epsilon M} tr\{\widehat{\mathbf{R}}(\mathbf{z})\} \tag{2.23}$$

where ϵ scales the amount of loading and $tr\{\}$ is the trace. Eq. (2.22) makes the loading proportional to the average power of the focused signals. Although this is desirable since it adds less absolute loading to points where the signals are weak, ϵ is still a user parameter. The increase in robustness comes at the cost of lower adaptivity. The diagonal loading also makes the MVBF less sensitive to differences in amplitude over the array caused by directional near-field defects.

Another issue which is common in practical applications is that the covariance matrix does not have full rank or is poorly conditioned. Rank deficiency occurs, for example, when the number of transmitters is less than the number of receivers. Sufficient diagonal loading ensures that the pseudo-covariance matrix is well-conditioned.

2.4.5 The Algorithm

The previous sections explained in detail the proposed method. The whole procedure can be summarized in the following steps performed for each point $\mathbf{z}$ in the region of interest for a particular Lamb mode n :

1. Compensate for dispersion using the dispersion characteristics of mode n, $k_n(\omega)$, (2.13)
2. Create focused vector for point $\mathbf{z}$, (2.16)
3. Calculate averaged covariance matrix (2.17)
4. Apply diagonal loading (2.22) - (2.23)
5. Calculate the MVBF weight vector and estimate the power (2.18) - (2.19)

Forming a dispersion compensated SBF only requires steps 1 and 2 and its output estimate is then given by (2.20).

2.5 Results

In this section the results of comparison of the proposed MVDF with SBF DAS beamformer will be presented. The MVDF method was evaluated using both simulated and experimental data using an aluminium plate with artificial defects.

2.5.1 The imaging object

The object used for the evaluation was a 6 mm thick, 750x750 mm aluminum plate (6082-T6) with artificial defects. The artificial defects included pairs of drilled-through holes, a 1 cm wide notch, and some artificial pits with depths 1 to 3 mm. Due to difficulties in creating realistic simulation models for the notch and the pits, only the circular holes were used in the simulation model. The layout of the defects and the positions of the array and the transmitter are shown in Fig. 2.5. The pairs of holes are labeled A, B and C. Pair A consists of two holes, 7 mm in diameter, 28 mm apart while pair B and C consists of two 5 mm holes each, located 21 and 10 mm apart, respectively.

The dispersion characteristics

To experimentally determine the amplitude of the transmitted Lamb modes and to validate the theoretically determined dispersion curves, a single transmitter/receiver pair was used to perform measurements allowing the calculation of a spatio-temporal FFT [22]. In this experiment the transmitting transducer was excited by a single square pulse, 1 μs long with amplitude 16 V. The receiving transducer was shifted along a 75 mm line in 1 mm intervals, resulting in 75 signals. The spatio-temporal FFT resulted in a multi-mode signal that can be seen in the frequency-wavenumber power spectrum shown in Fig. 2.6.

From the Fig. 2.6 it can be seen that the received S_0 mode had a higher amplitude than the A_0 mode around 350 kHz. The initially used longitudinal and transversal velocities for

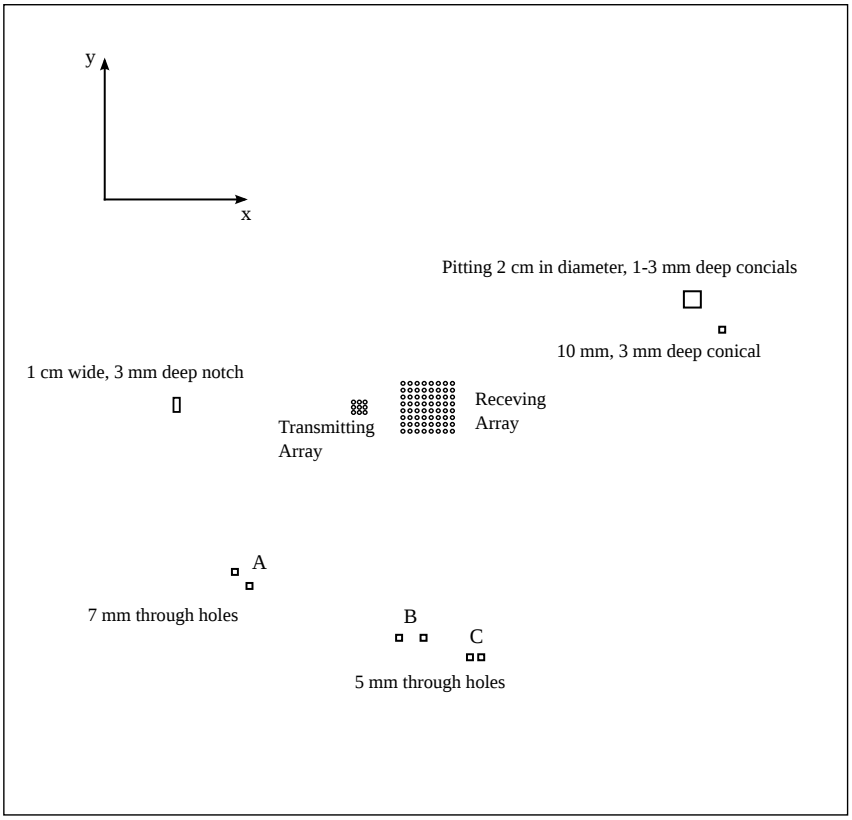

Figure 2.5: Layout of the inspected aluminum plate. The labels A,B,C identify three pairs of closely spaced holes. Both arrays are virtual. The transmitting array is created by moving a single transducer (pinducer). The receiving array is created by moving a linear array consisting of 8 pinducers.

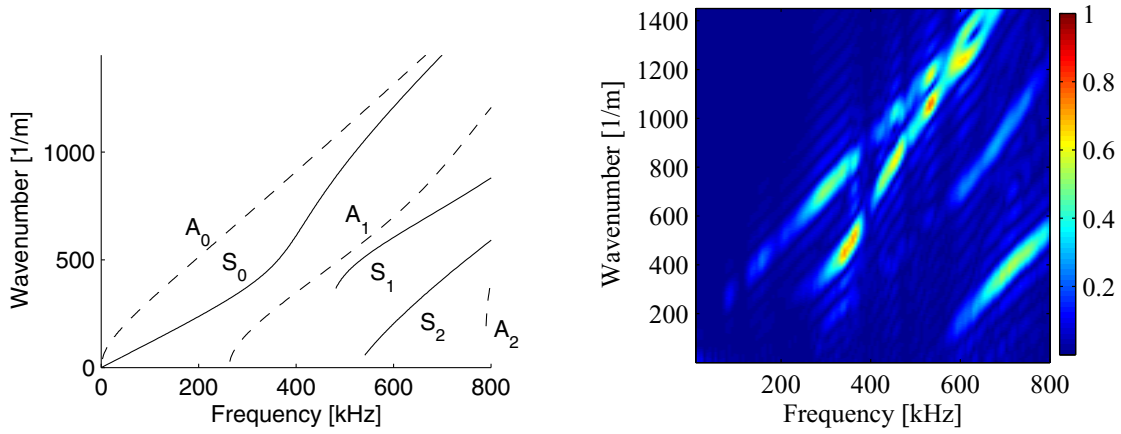

Figure 2.6: Theoretically (a) and experimentally (b) determined dispersion curves for the 6 mm aluminum plate.

calculating the theoretical dispersion curves did not result in a sufficiently good agreement with the experimentally determined curves. The best match for the A_0 mode was achieved when setting the longitudinal wave velocity to 6198 m/s and the shear wave velocity to 3158 m/s. The resulting theoretically determined dispersion curve is shown in Fig. 2.6.

Ideally, all received modes should be processed and used as a basis for the evaluation of the structure. Due to the shorter wavelength of the A_0 mode compared to the S_0 mode, and poor agreement between simulated and measured dispersion characteristics for the S_0 mode, only results from focusing using the A_0 mode dispersion characteristics are presented here. For the frequency range used in the experiments, the A_0 mode had wavelengths down to 7 mm. To avoid spatial aliasing, this required an array element spacing of a maximum of 3.5 mm.

2.5.2 The test setups

The imaging performance of the proposed method was evaluated separately for two setups specified in Sec 2.2:

1. A single stand-alone transducer was used for the excitation and the back-scattered signals were received by two different rectangular arrays: Array 1 formed of 8x8 elements with 3.5 mm element spacing, and Array 2 formed of 8x8 elements with 7 mm element spacing.

2. Repeated measurements were performed with the transmitting transducer at 9 different positions, and the backscattered signal received by the 8 element linear array at 8 different positions for each transmitter position.

Small *pinducers* from Valpey Fisher Corp were used both as receivers and transmitter. The pinducers had a diameter of 1.5 mm and a resonance frequency of 1.1 MHz, which was well above the frequency range used in the experiments. The pinducers were coupled to the plates through a thin layer of oil which limited the detection and generation to out-of-plane displacement.

To limit the influence of aliasing, the element spacing in the array should be no larger than 3.5 mm. However, the shape of the pinducers allowed a minimum element distance of 7 mm, which is comparable to the minimum wavelength of the A_0 mode. Furthermore, limitations in the number of available pinducers and the electronics allowed only an 8 element linear array and a single transmitter to be used simultaneously in the setup.

The receiving arrays were formed virtually by repeated measurements performed using a linear uniform array with 8 pinducers with 7 mm spacing. To form the Array 2 the measurements were repeated with the linear receiving array shifted at 8 different positions. Array 1 with 3.5 mm element spacing was formed by taking measurements at 2x8 different positions using 4 elements of the receiving array.

2.5.3 Simulation results

The simulated results are separated into two parts: a simulation study evaluating the mode suppression capabilities of the proposed method, and the results comparing imaging performance.

Mode suppression

The mode suppression performance of the SBF and MVBF was evaluated using simulated datasets from three different, fully active, array configurations illustrated in Fig. 2.7. The array configurations are subsets of the 8x8 array, where the 1x8 and 2x8 are the top rows of

the larger array. The datasets were generated using the model described in Sec 2.3.1 with the dispersion characteristics of the 6 mm aluminium plate shown in Fig. 2.2.

Two Lamb modes were simulated, the A_0 and S_0 modes, which were reflected from a single reflector located 375 mm from the center of the 8x8 array. Both modes were reflected with unit reflection coefficient. All array elements were excited sequentially and the back-scattered signals were calculated for each array element. The element spacing was 3.5 mm, which was approximately half the minimum wavelength of the A_0 mode in the frequency range used. The input signal was a 1 cycle 300 kHz sinusoid which was bandpass filtered to a bandwidth of 260 kHz. No apodization was applied on the SBF.

In this step no mode conversions were simulated. The focusing was performed using the dispersion characteristics of the A_0 and S_0 modes. The results obtained using a single 8 element linear array, a 2x8 array and the full 8x8 array, when focusing on the A_0 and S_0 mode, are presented in Figs 2.8 and 2.9, respectively. In the frequency range of the simulated signals, the A_0 mode is only slightly dispersive. By contrast, the S_0 mode is highly dispersive, which can be seen in Fig. 2.8 where it is smeared over a wide range. In Fig. 2.9 the dispersion compensation of the S_0 has the reverse effect on the A_0 mode, it becomes dispersed.

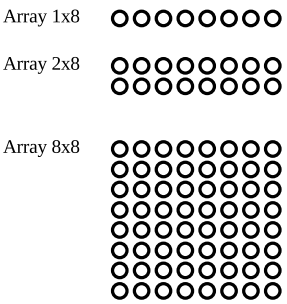

Figure 2.7: Array configurations used for mode suppression evaluation.

In the second step the suppression capabilities of the compared methods were evaluated including mode conversion in the simulation. The same array configurations as in the previous simulations were used but this time a single reflection caused mode conversion between the A_0 and S_0 modes. Figure 2.10 shows the results for the three considered array configurations and for two reflected modes. The S_0 mode was converted into a S_0 and an A_0 mode, where the power was divided equally between both modes. For simplicity the A_0 mode was assumed to result in a pure A_0 mode on reflection.

The simulated results in Figs. 2.8 - 2.10 show that the MVBF can be very efficient in suppressing interfering modes. In terms of angular resolution, the MVBF clearly outperforms the SBF. As expected, the single row array completely fails to suppress the interfering mode, but with only a two row array, the MVBF performed very well in suppressing the interfering mode. For the eight rows array, both approaches showed reasonable performance in mode suppression, although the MVBF offers much better resolution.

The mode converted signals in Fig. 2.10 proved to be more difficult to suppress and the SBF performed significantly worse in this case. From the algorithm's point of view, mode conversion does not differ from that for the non-converted case. However, in this case there are two interfering signals to suppress, the unconverted and the converted S_0 mode, which leads to poorer performance when only two rows are available.

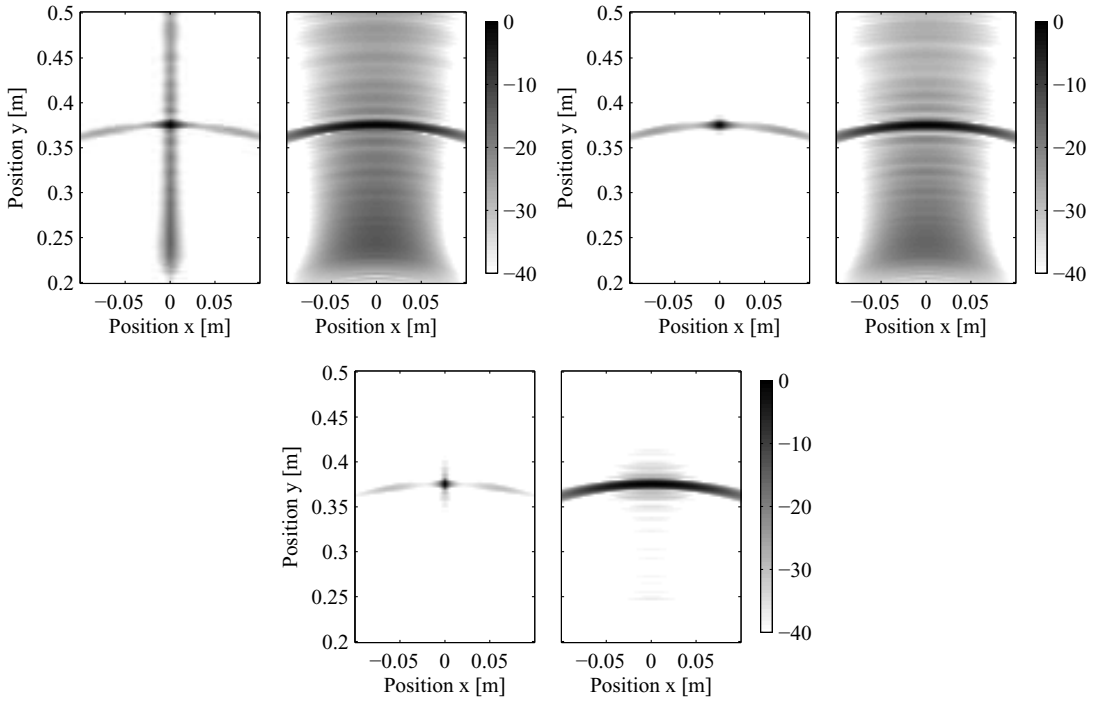

Figure 2.8: Simulated results illustrating the capability of suppressing the S_0 mode when focusing on the A_0 mode of the reflected $S_0 - A_0$ modes using 1x8, 2x8 and 8x8 array. MVBF (left) and SBF (right) in each pair. The MVBF performs well using only two rows.

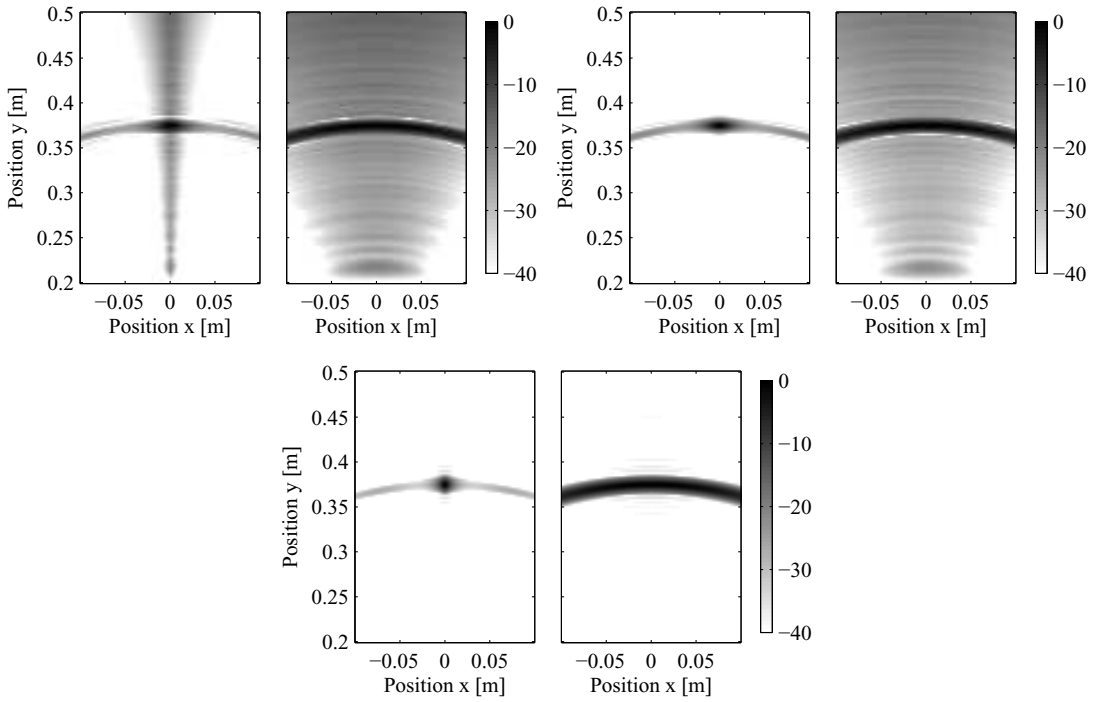

Figure 2.9: Simulated results illustrating the capability of suppressing the A_0 mode when focusing on the S_0 mode of the reflected $S_0 - A_0$ modes using 1x8, 2x8 and 8x8 array. MVBF (left) and SBF (right) in each pair.

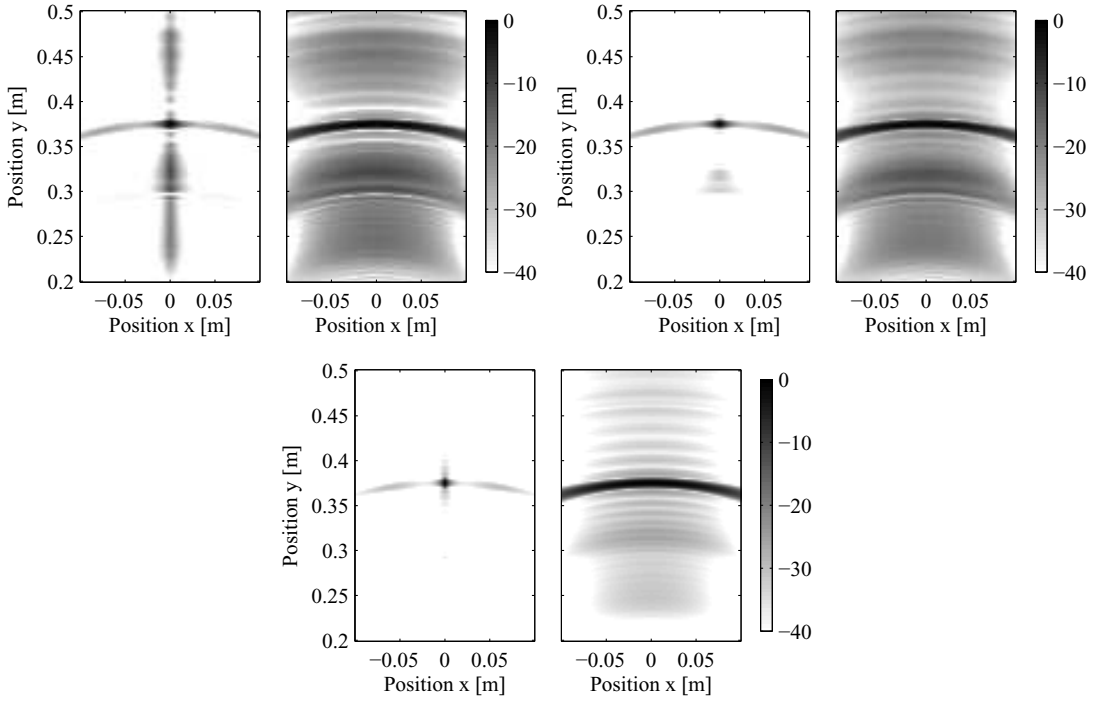

Figure 2.10: Simulated results of suppression capabilities of S_0 mode and mode-converted $S_0 - A_0$ mode when focusing on the A_0 mode using 1x8, 2x8 and 8x8 array. MVBF (left) and SBF (right) in each pair. Again, the MVBF performs very well compared to the SBF.

Simulated imaging results

Comparison of the imaging performance of the proposed method, evaluated for both setups specified in Sec 2.5.2 with the SBF DAS beamformer is presented below.

Two Lamb modes were included in the simulations, the S_0 and the A_0 mode. Only the holes, edges, and corners, were included and were simulated as point-scatterers, with a positive real frequency independent reflection coefficient. The reflection coefficients were proportional to the diameter of the holes. For simplicity, the edge and corner reflections were also simulated as point-scatterers, with reflection coefficients 10 times that of the smallest holes. No multiple scattering or mode conversions were assumed. The notch and pits were not included in the simulation.

Since the transducers were coupled to the plate using oil the transducer-plate interaction was modeled assuming out-of-plane components only. The transfer functions used for this purpose were calculated using the model described in Section 2.3.1. The input signal was a 300 kHz, single cycle sinusoid, bandpass filtered to a bandwidth of 260 kHz. White Gaussian noise was added to the simulated received signals giving a signal-to-noise ratio (SNR) of 25 dB.

The theoretical level of relative excitation between the S_0 and A_0 modes, expressed as a normalized $|H_n(\omega)|$, is shown in Fig. 2.11. It can be seen that the A_0 mode has a higher excitability than the S_0 mode around 300 kHz. Since this transfer function operates on the input signal, the slope of the curve shifts the center frequency of resulting A_0 mode from 300 kHz to 280 kHz, maintaining approximately the same bandwidth. The wavelength of the A_0 mode is 10.5 mm at 280 kHz.

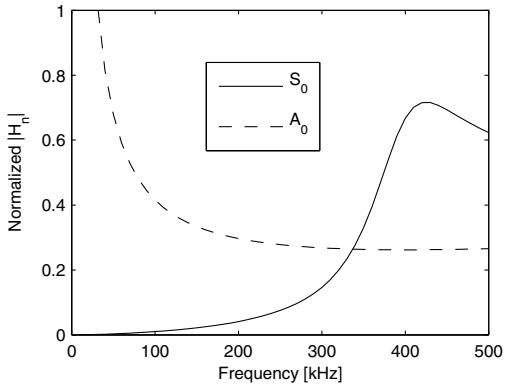

Figure 2.11: Normalized excitability of the S_0 and A_0 modes.

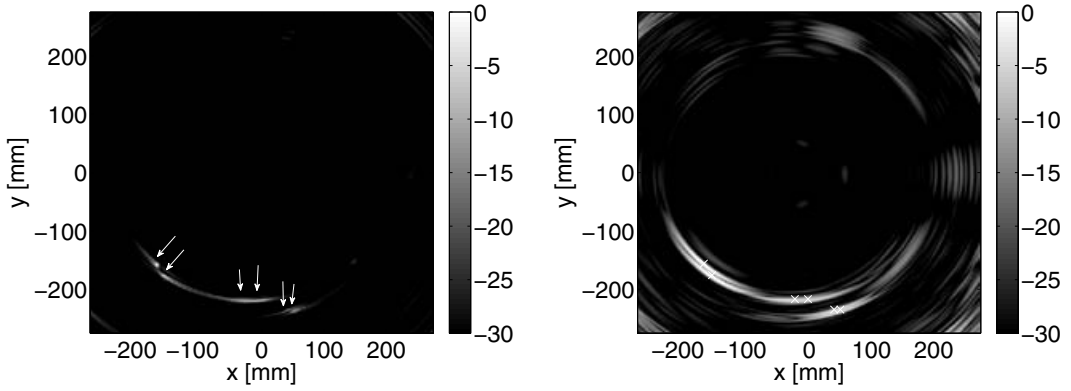

(a) (b)

Figure 2.12: Simulation results from 6 mm plate for Array 1, $\epsilon = 50$. MVDR (a) and SBF (b) focusing on the A_0 mode. Holes are indicated by white crosses or arrows. Note that the arrows do not point at the exact position of the defect. Log scale cut at -30 dB.

Setup 1 – single transmitter

Fig. 2.12 shows the result from the MVDR and the SBF on signals obtained through the simulation of Array 1. Reflections from the hole pairs A, B and C can be seen in the lower part of the images. The true hole positions are marked either with white crosses or arrows. The results from Array 2 are shown in Fig. 2.13.

Fig. 2.14 shows the angle and range resolvability of the pair of holes A obtained for the results presented in Fig. 2.13. The projections were created by taking the maximum values in range and angle, respectively, in the vicinity of the defects. Note that the transmitter position outside the array in conjunction with the holes locations in the near field of the array, leads to elliptic shaped beams, where the transmitter and the center of the array are in the focus points of the ellipses. This makes angle and range resolution somewhat distorted when plotting range and angle from the the center of the array. The projections were therefore created using a point between the center of the array and the transmitter as a reference for the range and angle.

From the profiles in Fig. 2.14 it is clear that the MVDR approach yields higher resolution than the SBF method on simulated data. Underestimation can be seen in the results where the SBF correctly estimates the same amplitude on both defects, while the MVDR underestimates the amplitude of one of the holes.

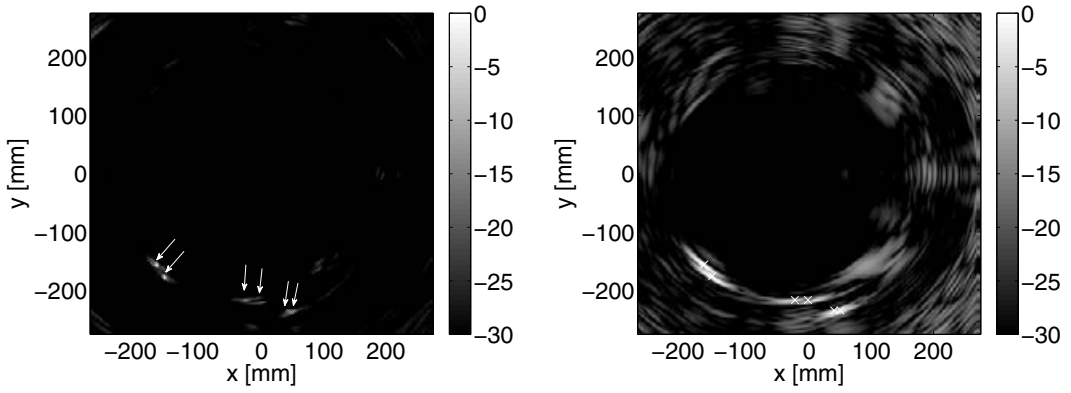

(a) (b)

Figure 2.13: Simulation results from 6 mm plate for Array 2, $\epsilon = 20$. MVDR (a) and SBF (b) focusing on the A_0 mode. Holes are indicated by white crosses or arrows. Note that the arrows do not point at the exact position of the defect. Log scale cut at -30 dB.

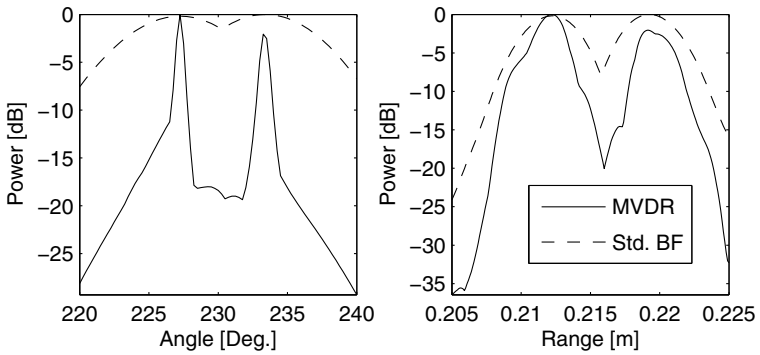

Figure 2.14: Angle and range resolvability of hole pair A using the MVDR and SBF on simulated data from Array 2 on 6 mm plate.

Signal cancellation due to closely spaced defects is an important issue for the MVDR algorithm. In the simulation results using Array 2 in Fig. 2.13, the reflections from the pair of holes labeled C seem to cancel, which leads to underestimation of their amplitude. The cancellation was much less severe when using Array 1 even with less diagonal loading, see Fig. 2.12.

Setup 2 – multiple transmitters

The simplified simulation model in Section 2.3.1 was used along with the estimated dispersion characteristics to create datasets for three different active array sizes, a 4x4, a 6x6 and an 8x8 rectangular array, positioned at the center of the plate in the geometrical setup in Fig. 2.5.

A full dataset of transmitter - receiver combinations was generated. Figs 2.15, 2.16 and 2.17 show the resulting images for the active uniform rectangular arrays. No apodization was applied on the SBF.

Since the focusing is performed using the A_0 mode dispersion characteristics, the interfering dispersed S_0 mode from edge and corner reflections can be seen at even 45° angles, particularly for the 4x4 array. The larger arrays yield higher resolution and weaker S_0 mode, which is to be expected. The hole pair B was not resolved by any of the arrays. A false echo can be seen in the lower right quadrant of the images. It is not caused by aliasing, but is due to the combined contributions from the defects and the corner reflected S_0 mode. This is related to the discussion on focusing effects in Sec 2.4.3 above.

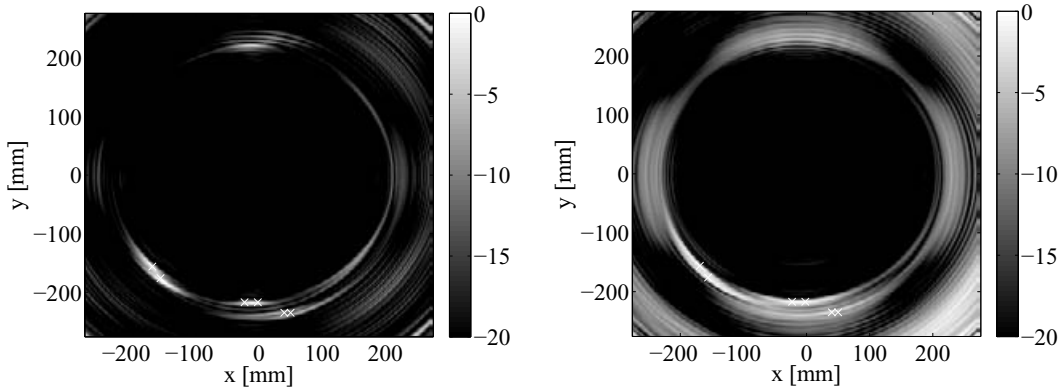

Figure 2.15: Simulated results using a 4x4 array. MVBF (left) and SBF (right).

The MVBF was not capable of suppressing the false echo and even though it appears less smeared than that for the SBF, it has, at least relatively, slightly higher amplitude. The problem could be reduced by using only a subset of the transmitters in each covariance matrix estimate.

If no reciprocity between the transmit-receive pairs is assumed, the 8x8 array will produce 64x64 combinations. The 8x8 array was divided into four 4x4 non-overlapping transmit subarrays. Using only the transmitters from each subarray for estimation lead to four sets of 16x64 received signals. This results in four weight vectors calculated using the covariance matrices from each transmitting subarray. The outputs from the array using the different weight vectors were then averaged. The results from the procedure are shown in Fig. 2.18.

Generally, from the simulated results of the plate inspection it is apparent that the MVBF approach performs much better than the SBF, especially in terms of resolution. For the 4x4 array in Fig. 2.15, the effects from edge and corner reflections of the S_0 mode can be clearly seen at 45° intervals for both the SBF and the MVBF, although the MVBF was much more efficient in suppressing these effects. In the ideal simulation environment, where there is no uncertainty of

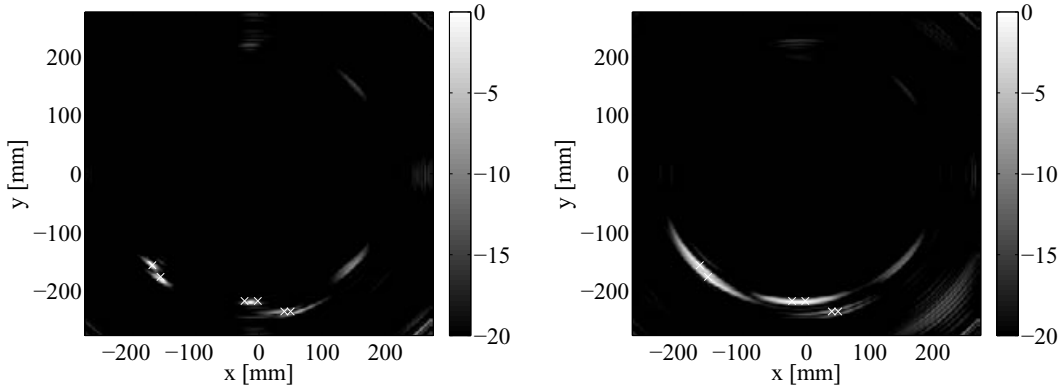

Figure 2.16: Simulated results using a 6x6 array. MVBF (left) and SBF (right).

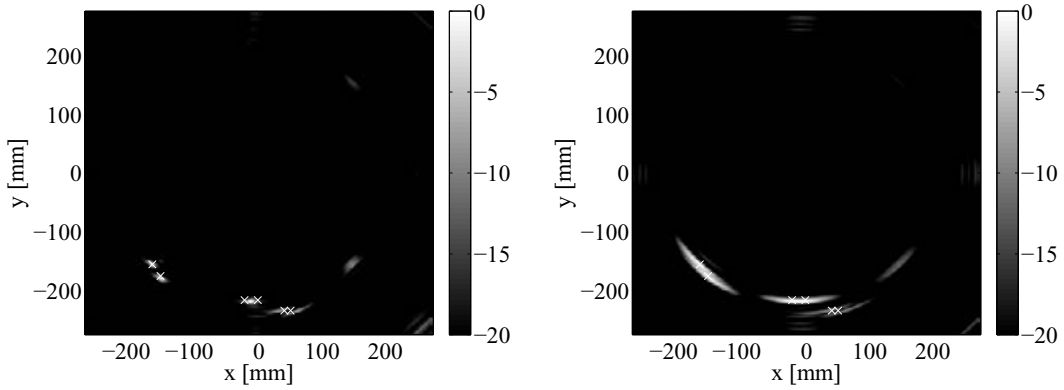

Figure 2.17: Simulated results using a 8x8 array. MVBF (left) and SBF (right).

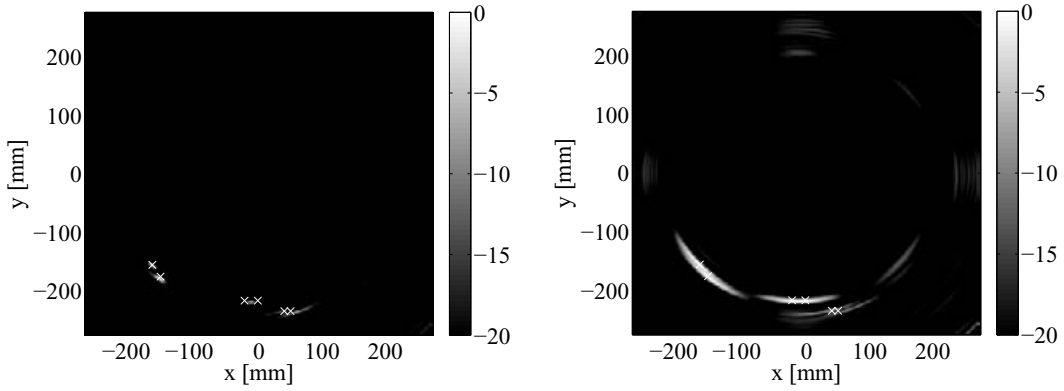

Figure 2.18: Simulated results using a 8x8 array with 4 transmitter subarrays. MVBF (left) and SBF (right).

element positions or dispersion characteristics, even the 4x4 array using the MVBF outperforms the 8x8 array using SBF in terms of resolution. Because of the relatively small array sizes, the holes in pair B were not resolved in any of the simulation examples. However, the holes in pair C were resolved on all array sizes for the MVBF, and on the 6x6 and 8x8 arrays for the SBF, even though the distance between the holes in pair C were smaller than pair B. This is simply because pair C are at different distances from the center of the array and are therefore resolved in time.

The false echo seen in the center of the lower right quadrant of all the simulated image results, except for Fig. 2.18, is due to the multiple transmitter excitation. As discussed in Section 2.4.1, the covariance matrices formed by each transmission do not cover the same interference environment. It can be seen in the images that the false echo is in approximately the same range as the other defects, which is the reason for its appearance. Fig. 2.18 shows that using fewer transmitters for each estimation can reduce these problems, at the cost of increased signal cancellation. Furthermore, hole pair B were underestimated compared to the SBF, and also compared the images in Figs. 2.15–2.17, where the full set of transmitters were used.

2.5.4 Experimental imaging results

Experimental verification of imaging has been until now performed for a single transmitter only; experiments with multiple transmitter array will be carried out when a new multi-output instrument will be delivered.

Due to the limited number of available transducers and limitations of the electronics only an 8 element uniform linear array was used simultaneously for the reception. The array pinducers were connected to an Agilent Infiniium oscilloscope through a custom built multiplexing box followed by an AD8335 amplifier from Analog Devices. The sampling rate of the oscilloscope was set to 25 MHz. Due to the limited resolution of the oscilloscope (8 bits), the received edge reflections had to be saturated to get sufficient resolution of the weaker defect reflections. The received signal from each element was averaged 16 times. The direct signal from the transmitter to the array was removed before processing the signals. The input signal, a single square pulse, 1 μs long with amplitude 16 V, was generated by a HP8116 function generator.

Diagonal loading was applied to all MVBF results according to (2.22).

A comparison between the SBF and the MVDR approaches using Array 1 and 2 can be seen in Figs 2.19 and 2.20, respectively. Due to poor SNR the log scale is cut at -12 dB compared to -18 dB for Array 1. The holes are well pronounced in the lower part of the images where their true positions are marked with white crosses, or where necessary, arrows. The pit and the notch are seen at 0° and 180°, respectively.

Similarly to the simulated results in Fig. 2.14, Fig. 2.21 shows the angle and range resolvability of hole pair A obtained for the results presented in Fig. 2.20. The effect from the elliptic shaped beams also applies to the experimental results.

From the profiles in Fig. 2.21 it is clear that the MVDR approach yields higher resolution than the SBF method on both simulated and experimental data. Underestimation of the MVDR is less clearly seen than in the simulated results.

Signal cancellation due to closely spaced defects is an important issue for the MVDR algorithm. In the experimental results the underestimation problem was most severe for Array 1 as can be seen from Fig. 2.19. Both methods yield different amplitudes for the holes A but show reasonable accuracy in position. The MVDR has significant problems with both power and position of pair B and C. The SBF approach yields more reasonable amplitude estimates but it is very difficult to determine the positions of the defects.

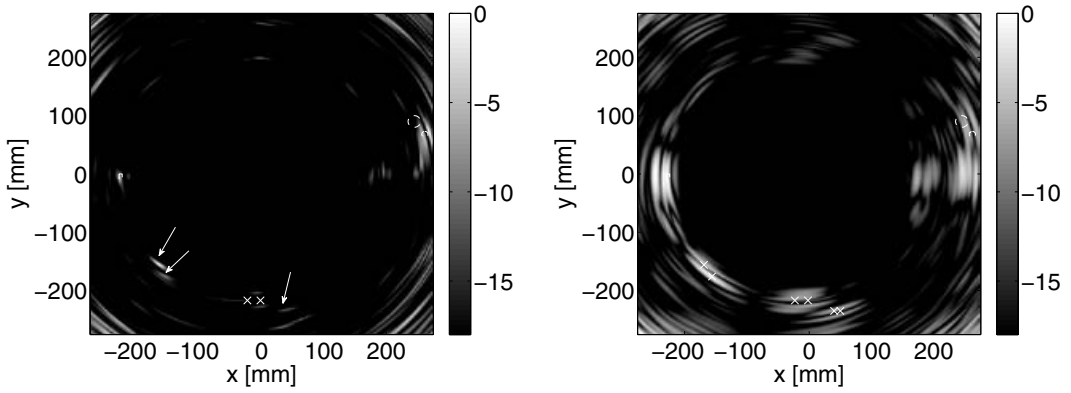

(a) (b)

Figure 2.19: Measurement results from 6 mm plate for Array 1, $\epsilon = 50$. MVDR (a) and SBF (b) focusing on the A_0 mode. Defects are indicated by white crosses or arrows (holes, lower part of the image), and dashed lines (pittings and notch, at 0° and 180°, respectively). Note that the arrows do not point at the exact position of the defect. Log scale was cut at -18 dB.

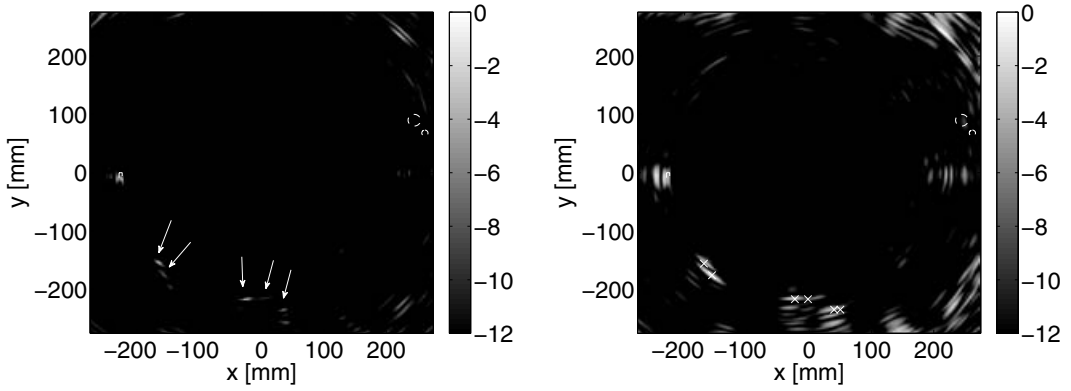

(a) (b)

Figure 2.20: Measurement results from 6 mm plate for Array 2, $\epsilon = 5$. MVDR (a) and SBF (b) focusing on the A_0 mode. True positions of the defects are indicated by white crosses or arrows (holes, lower part of the image), and dashed lines (pittings and notch, at 0° and 180°, respectively). Note that the arrows do not point at the exact position of the defect. Log scale was cut at -12 dB.

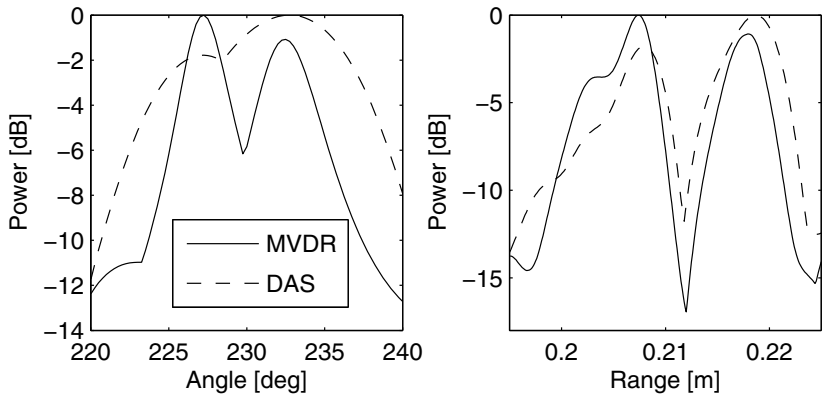

Figure 2.21: Angle and range resolvability of hole pair A using the MVDR and SBF on measured data from Array 2 on 6 mm plate..

In the results for Array 2 presented in Fig. 2.20, both holes in pair B are detected. Although both methods estimate the amplitude of the right hole lower than for the left, its position is too far to the right. Pair C can not be resolved and is detected as a single defect. Both methods underestimate the amplitude but the MVDR more severely. Since both methods have problems with pairs B and C it can not be concluded that this is an effect related to the MVDR approach.

The saturation of the edge reflections created significant amount of noise in post-processed data from both algorithms in the areas closer than 100 mm to the edges, which is the reason for not showing images covering the whole plate. After increasing the amplitude range of the oscilloscope, and thereby avoiding saturation, these problems disappeared. Unfortunately, the insufficient dynamic range made the much weaker signals from the defects undetectable using either of the algorithms.

An obvious limitation of the measurement setup is the simultaneous use of only 8 array elements, which hindered assessing the potential effects of interelement scattering that may be encountered for a full 2D array.

2.6 Conclusions

A method for adaptive beamforming of Lamb waves has been presented in this chapter. The dispersion of the Lamb modes was compensated using theoretically predicted dispersion curves. Dispersion compensated data was processed using both a standard SBF beamformer and the MVDR beamformer. Simulated and experimental results show that the MVDR approach can yield better performance compared to the standard SBF approach in terms of higher resolution and better suppression of interfering Lamb modes.

Signal cancellation that may result in the underestimation of the signal amplitudes, is an issue that needs to be addressed when working with the MVDR algorithm. Increasing the number of subarrays used for spatial smoothing can reduce signal cancellation effects and increase robustness at the cost of lower resolution and adaptivity of the filter. Diagonal loading also reduces signal cancellation to some degree and improves robustness of the estimation.

The MVDR algorithm, presented in the paper can be easily generalized to an active array with multiple transmitters.

Bibliography

[1] W. Mohr and P. Höller. On inspection of thin-walled tubes for transverse and longitudinal flaws by guided ultrasonic waves. *IEEE Transactions on Sonics and Ultrasonics*, 23:369–374, 1976.

[2] E. Lehfeldt and P. Höller. Lamb waves and lamination detection. *Ultrasonics*, 5:255–257, 1967.

[3] P.D. Wilcox, M.J.S. Lowe, and P. Cawley. Lamb and SH wave transducer arrays for the inspection of large areas of thick plates. In *Annual Review of Progress in QNDE*, volume 19A, pages 1049 – 56, 2000.

[4] V. Giurgiutiu and J. Bao. Embedded Ultrasonic Structural Radar for the Nondestructive Evaluation of Thin-Wall Structures. In *Proceedings of the 2002 ASME International Mechanical Engineering Congress*, pages 17–22, 2002.

[5] P.D. Wilcox. Omni-directional guided wave transducer arrays for the rapid inspection of large areas of plate structures. *IEEE Transactions on Ultrasonics, Ferroelectrics and Frequency Control*, 50(6):699 – 709, 2003.

[6] P. Fromme, P.D. Wilcox, M.J.S. Lowe, and P. Cawley. On the development and testing of a guided ultrasonic wave array for structural integrity monitoring. *IEEE Transactions on Ultrasonics, Ferroelectrics and Frequency Control*, 53(4):777 – 85, 2006.

[7] J. Rajagopalan, K. Balasubramaniam, and C.V. Krishnamurthy. A phase reconstruction algorithm for Lamb wave based structural health monitoring of anisotropic multilayered composite plates. *Journal of the Acoustical Society of America*, 119:872, 2006.

[8] F. Yan, R.L. Royer jr, and J.L. Rose. Ultrasonic guided wave imaging techniques in structural health monitoring. *Journal of Intelligent Material Systems and Structures*, 21(3):377, 2010.

[9] P.D. Wilcox, M. Lowe, and P. Cawley. Omnidirectional guided wave inspection of large metallic plate structures using an EMAT array. *IEEE Transactions on Ultrasonics, Ferroelectrics and Frequency Control*, 52(4):653–665, 2005.

[10] V. Giurgiutiu. Tuned Lamb wave excitation and detection with piezoelectric wafer active sensors for structural health monitoring. *Journal of Intelligent Material Systems and Structures*, 16(2):291 – 305, 2005.

[11] P.D. Wilcox. A rapid signal processing technique to remove the effect of dispersion from guided wave signals. *IEEE Transaction on Ultrasonics, Ferroelectrics and Frequency Control*, 50(4):419–427, 2003.

[12] A. Velichko and P.D. Wilcox. Guided wave arrays for high resolution inspection. *Journal of the Acoustical Society of America*, 123(1):186 – 196, 2008.

[13] Z. Wang, J. Li, and R. Wu. Time-delay-and time-reversal-based robust Capon beamformers for ultrasound imaging. *IEEE Transactions on Medical Imaging*, 24(10):1308–1322, 2005.

[14] M. Sasso and C. Cohen-Bacrie. Medical ultrasound imaging using the fully adaptive beamformer. In *IEEE International Conference on Acoustics, Speech and Signal Processing, 2005.*, volume 2, pages 489–492, 2005.

[15] J.F. Synnevåg, A. Austeng, and S. Holm. Adaptive beamforming applied to medical ultrasound imaging. *IEEE Transactions on Ultrasonics, Ferroelectrics and Frequency Control*, 54(8):1606–1613, 2007.

[16] J.E. Michaels, J.S. Hall, and T.E. Michaels. Adaptive imaging of damage from changes in guided wave signals recorded from spatially distributed arrays. In *Proceedings of SPIE*, volume 7295, page 729515, 2009.

[17] T. Stepinski and M. Engholm. On the development and testing of an uniform circular array for structural health monitoring of planar structures. In *Proc. of the Fourth European Workshop on Structural Health Monitoring*, Krakow, Poland, July 2008.

[18] T. Stepinski and M. Engholm. Piezoelectric circular array for structural health monitoring using plate waves. In *7th International Workshop on Structural Health Monitoring*, Stanford, CA USA, September 2009.

[19] M. Engholm and T. Stepinski. Direction of arrival estimation of Lamb waves using circular arrays. *accepted for publication in Structural Health Monitoring*, 2010.

[20] M. Engholm and T. Stepinski. Adaptive beamforming for array imaging of plate structures using lamb wave. *Submitted to IEEE Transactions on Ultrasonics, Ferroelectrics and Frequency Control, December 2009*.

[21] J. L. Rose. *Ultrasonic Waves in Solid Media*. Cambridge University Press, 1999.

[22] D. Alleyne and P. Cawley. A two-dimensional fourier transform method for the measurement of propagating multimode signals. *Journal of the Acoustical Society of America*, 89(3):1159 – 1168, 1991.

[23] H. L. Van Trees. *Optimum Array Processing*, volume 4 of *Detection, Estimation, and Modulation Theory*. Wiley-Interscience, New York, 1 edition, 2002.

[24] J. Capon. High-resolution frequency-wavenumber spectrum analysis. *Proceedings of the IEEE*, 57(8):1408 – 1418, 1969.

[25] P. Stoica and R.L. Moses. *Introduction to spectral analysis*. Prentice Hall Upper Saddle River, New Jersey, 1997.

[26] B. Widrow, K. Duvall, R. Gooch, and W. Newman. Signal cancellation phenomena in adaptive antennas: Causes and cures. *IEEE Transactions on Antennas and Propagation*, 30(3):469–478, 1982.

[27] J. Li, P. Stoica, and Z. Wang. On robust capon beamforming and diagonal loading. *IEEE Transactions on Signal Processing*, 51(7):1702 – 1715, 2003.

[28] J. Krolik and D. Swingler. Multiple broad-band source location using steered covariance matrices. *IEEE Transactions on Acoustics, Speech and Signal Processing*, 37(10):1481 – 1494, 1989.

[29] H. Hung and M. Kaveh. Focussing matrices for coherent signal-subspace processing. *IEEE Transactions on Acoustics, Speech, and Signal Processing*, 36(8):1272 – 1281, 1988.

[30] T.J. Shan, M. Wax, and T. Kailath. On spatial smoothing for directon-of-arrival estimation of coherent signals. *IEEE Transactions on Acoustics, Speech, and Signal Processing*, 33(4):806 – 811, 1985.

[31] M. Papazoglou and J. L. Krolik. High resolution adaptive beamforming for three-dimensional acoustic imaging of zooplankton. *The Journal of the Acoustical Society of America*, 100(6):3621–3630, 1996.

Chapter 3

Computationally efficient 3D image reconstruction using array data

by Tomas Olofsson

This chapter concerns the use of migration techniques, originally developed in seismic exploration for the examination of the Earth's interior, to ultrasonic data. In particular, we consider the immersion test setup for which time domain methods such as SAFT are cumbersome to use due to the refraction at the layer interfaces. The particular form of migration considered in the work, the so-called phase shift migration, is well suited for treating this problem since it provides simple means for focusing through media consisting of several horizontal layers and it has, in addition, computational advantages since it operates in the frequency domain and, thus, benefit from the computational efficiency of the fast Fourier transform.

In a previous study [1], we considered phase shift migration for 2D reconstructions using a single scanned transducer. For ease of reference, a version of this work is presented in Section 3.1 in the form of an article that has been accepted for publication in IEEE Transactions on Ultrasonics and Ferroelectrics, 2010. In the remaining of this chapter, two extensions of this work are then presented. The first of these, presented in Section 3.2, is to go from 2D to 3D data in order to fully utilize the resolution enhancement potential of the technique. This section also gives a more detailed algorithm description and complexity analysis, as well as an examination of the resolution of the reconstructed images.

The second extension, which is presented in Section 3.3, consists in generalizing the technique to allow for the processing of data acquired using an array. Finally, in Section 3.4, a robustness issue related to objects having front surfaces that are slightly tilted relative to the scanning axis is considered and a solution to the problem in proposed.

3.1 Phase shift migration for imaging layered objects and objects immersed in water

Here the use of phase shift migration for ultrasonic imaging of layered objects and objects immersed in water is proposed. The method, which was developed in reflection seismology, is a frequency domain technique that in a computationally efficient way restores images of objects that are isotropic and homogeneous in the lateral direction but inhomogeneous in depth. The performance of the proposed method was evaluated using immersion test data from a block with side drilled holes with an additional scatterer residing in water. In this way, the method's capability of simultaneously imaging scatterers in different media and at different depths was investigated. The method was also applied to a copper block with flat bottom holes. The results altogether verify that the proposed method is capable of producing high resolution and low noise images for layered or immersed objects.

3.1.1 Introduction

One important imaging method in ultrasonic testing is the synthetic aperture focusing technique (SAFT), which was introduced in ultrasonic nondestructive testing (NDT) in the early 1970s [2, 3] and that has been in wide use since the late 1980s. In basic SAFT, a synthetic array is emulated in post-processing using pulse-echo data acquired with a physically scanned single-element transducer. The post-processing consists of delay-and-sum beamforming and the resulting images generally have far better lateral resolution than the B-scans from which they are constructed. Moreover, the lateral resolution is independent of depth. The coherent summation also yields an increase in signal-to-noise ratio resulting in an improved depth-of-field.

The early versions of SAFT were time domain implementations, followed later by implementations in the frequency domain [4–7], evolving from acoustical holography [8] and diffraction tomography. The frequency domain implementations are particularly attractive if the sound speed is constant throughout the entire propagation medium, something which holds when a homogeneous and isotropic object is tested in contact. Then SAFT can be implemented in a computationally very efficient form using a method that was first proposed in geophysics [9], called Stolt migration or the frequency wavenumber method [5, 6, 10].

Practical drawbacks with contact testing are transducer wear and potentially poor or nonuniform acoustical coupling between transducer and test object due to rough surfaces. Therefore, immersion testing is often preferred in NDT. Note that the above mentioned assumption of having constant sound speed in the propagating medium then no longer holds since the propagation involves, at least, two sound speeds, one in water and one in the solid. Thus, unfortunately, the conditions required by the frequency wavenumber method do not hold. In time domain SAFT, the problem manifests itself in that the refraction at the liquid-solid interface complicates the computation of the travel times required in the algorithm. Such complications are of course present in any situation having test objects consisting of layers with different sound speeds.

Despite the above mentioned difficulties, which to some extent have prevented the use of SAFT for immersion test data, various methods have been proposed to treat the immersion case. One such, which is restricted to one refracting layer only, is to use transducers that are focused on the object's surface, see e.g. [11], in this way emulating a scenario similar to contact testing with a transducer having a diameter of the size of the focal diameter. Note, however, that diffraction causes the acoustical field emitted from a focused transducer to take a form that may deviate from the spherical wave anticipated from a small transducer [12], thus to some extent violating the assumptions on which SAFT rely and thereby limiting the usefulness of the approach.

More generally, in inhomogeneous materials, the travel times required in time domain SAFT can be calculated using ray tracing techniques [13–15] that typically are time consuming, thus, limiting their practical usefulness. For the special case of horizontally layered materials, travel time approximations can be obtained more efficiently by means of so-called root-mean-squared (RMS) velocities [16], provided that the sound speed differences between layers are relatively small. This holds in many cases in reflection seismology where it is often used and in medical ultrasound where it has recently been used in the context of aberration correction [17]. When testing metals in immersion, the sound speed contrast is typically high and the RMS-velocity approach has this far not been used in the NDT community.

In reflection seismology, the case of objects consisting of horizontal homogenous layers has been treated extensively. There, a method called phase shift migration [18] has been developed for treating this scenario. Together with Stolt migration it has become an important tool for analyzing the Earth's interior structure [19] and it has been generalized in different ways, for instance, to admit also some lateral variations in sound speed [20]. Phase shift migration is a frequency domain approach that makes explicit use of the wave equation in the processing. Viewing the measured signals at the sensors as a boundary condition for the wave equation, the field is extrapolated using a phase-shift operator in the frequency domain to "hypothetical measurements" of the field at a set of different depths. From these, the image can be obtained in a fairly straightforward manner, see Section 3.1.2.

Due to its iterative nature, the method is computationally less efficient than Stolt migration but, on the other hand, phase shift migration can treat the more complicated scenario of having a sound speed that is constant in the lateral direction but varying in depth.

In this work, we investigate phase shift migration for imaging data acquired using immersion

testing, which is an application that is particularly well suited for phase shift migration since the sound speeds necessary in the processing typically are known to a great accuracy. The application used for illustration is immersion testing of copper blocks using a single scanned transducer and the experiments aim at demonstrating the potential of phase shift migration for this application. Note however that there are other potential important applications of the method. One such is inspection, in contact or in immersion, of metal objects with a protective stainless steel overlay having a different sound speed than the backing material.

Phase shift migration has been used earlier for ultrasonic imaging in [21]. Furthermore, the image formation equations in [7] are essentially identical to those in phase shift migration. However, in neither of these two references, the potential of allowing vertical sound speed variations was exploited. This was done in [8] but the imaging was performed using monochromatic signals.

Here we limit the work to concern only 2D migration and postpone an extension to full 3D migration to Section 3.2. The theory and the algorithm are given in Section 3.1.2 below. Experiments illustrating the approach are presented in Section 3.1.3 and, finally, conclusions and a discussion are given in Section 3.1.4.

3.1.2 Theory

In this section, a derivation of the reconstruction algorithm used in the work is given. The derivation presented below is based on what in geophysics is traditionally called the "exploding reflector" model [19, 22]. The reader should note that this model does not describe the single transducer scanned pulse-echo measurements scenario, hereafter called the monostatic[1] case, it is rather an analogous physical scenario for which a simple imaging algorithm can be developed. The idea is thus to first solve the imaging problem for this simple case and then show how the monostatic case can be transformed to it by simple means.

In the exploding reflector model, the reflectors in the medium are assumed to "explode" simultaneously at time $t = 0$, each with a strength that is proportional to its reflectivity, creating a field that is simultaneously measured using an array of sensors. The model neglects multiple reflections between layers and only up-going waves are considered. Furthermore, transmission losses at layer interfaces are neglected, see Appendix 3.A.1 for comments on this.

The derivation deviates from those found in the classical references, such as [18], in the respect that the vertical sound speed variations are introduced early in the model and not appearing as a last modification of a solution developed for a medium with constant sound speed, see [23] for comments on such inconsistencies.

The derivation is followed by a description of the steps necessary for adapting the monostatic case to an analogous exploding reflector scenario and a summary of the algorithm is subsequently given.

Phase shift migration for the "exploding reflector" scenario

In the following, we consider propagation of longitudinal waves in a medium illustrated in Fig. 3.1. It consists of L horizontal isotropic layers with thicknesses $d_1, ..., d_L$ and sound speeds, $c_1, ..., c_L$, respectively. The coordinate axes x and z point in the horizontal and vertical directions, respectively, with z pointing downwards. We let Z_l denote the z-coordinate of the lower side of layer l, i.e., $Z_l = \sum_{q=1}^{l} d_q$ and $Z_0 = 0$.

[1] The term *monostatic* is borrowed from the radar community.

Let $p(x, z, t)$ denote the field resulting from the reflectors in the medium, exploding simultaneously at $t = 0$. This field is observed along the horizontal line $Z_0 = 0$ and our aim is to extrapolate this observed field to lines at other depths within the medium. As will be described later, these can then be used straightforwardly to create an image of the media.

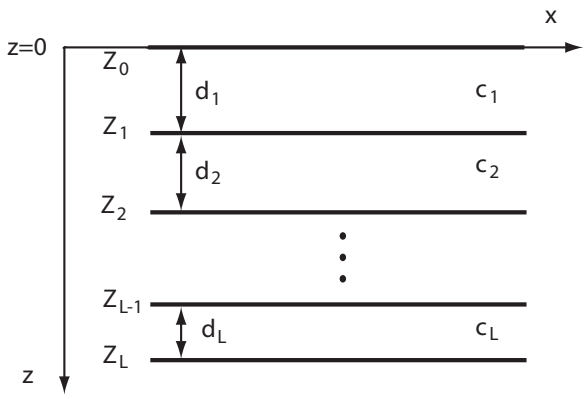

Figure 3.1: The layered media considered in the derivation.

The field extrapolation can be done by decomposing the field into a set of up-going harmonic plane wave components and performing the extrapolation separately for each component and superimposing the results. Consider one such up-going harmonic component within the l:th layer. It can be written as

$$p_l(x, z, t) = P_l(k_x, \omega) \exp(j(k_x x + k_{l,z}(z - Z_{l-1}) - \omega t)), \tag{3.1}$$

where ω is the angular frequency, k_x and $k_{l,z}$ are components of the wave number vector in the lth layer, and $P_l(k_x, \omega)$ is the complex amplitude of the component. We have here used Snell's law that states that k_x is preserved at a refracting interface that is parallel to the x-axis. Thus, we write k_x without a layer index, l. Note that writing the component's z-dependence as a function of the difference $z - Z_{l-1}$ instead of z merely serves the purpose of simplifying the notation in the following.

For a point belonging to the lth layer, the 2D scalar lossless wave equation states that

$$\left[\frac{\partial^2}{\partial x^2} + \frac{\partial^2}{\partial z^2} - \frac{1}{c_l^2}\frac{\partial^2}{\partial t^2}\right] p(x, z, t) = 0. \tag{3.2}$$

By inserting (3.1) into (3.2) we get

$$\left(-k_x^2 - k_{l,z}^2 + \frac{\omega^2}{c_l^2}\right) p_l(x, z, t) = 0, \tag{3.3}$$

and for a non-trivial solution, the dispersion relation

$$k_x^2 + k_{l,z}^2 = \frac{\omega^2}{c_l^2} \tag{3.4}$$

must be fulfilled. From this we can obtain $k_{l,z}$ as a function of ω, c_l, and k_x. If we consider only propagating, i.e., non-evanescent, waves we have that

$$k_{l,z} = -\sqrt{\frac{\omega^2}{c_l^2} - k_x^2}, \quad \text{with } \frac{\omega^2}{c_l^2} \geq k_x^2, \tag{3.5}$$

where we have used that $k_{l,z}$ is negative for an up-going wave component.

By inserting (3.5) into (3.1) we obtain

$$p_l(x,z,t) = P_l(k_x,z,\omega)\exp\left(j(k_x x - \omega t)\right), \tag{3.6}$$

with

$$P_l(k_x,z,\omega) = P_l(k_x,\omega)\alpha_l(k_x,z-Z_{l-1},\omega), \tag{3.7}$$

where $\alpha_l(k_x,\zeta,\omega)$ is defined as

$$\alpha_l(k_x,\zeta,\omega) = e^{-j\zeta\sqrt{\frac{\omega^2}{c_l^2}-k_x^2}}. \tag{3.8}$$

To find $P_l(k_x,\omega)$, first consider layer $l=1$. Note that at $z=0$, the component $p_1(x,z,t)$ is simply

$$p_1(x,z=0,t) = P_1(k_x,\omega)\exp(j(k_x x-\omega t)) \tag{3.9}$$

and, since the exponent is the conjugate of the kernel in a 2D Fourier transform[2] over x and t, the complex amplitude $P_1(k_x,\omega)$ must simply be the Fourier coefficient for the pair (k_x,ω) which we obtain by a 2D Fourier transformation of the field measured at Z_0.

For a point within layer $l=2$, the field extrapolated to depth Z_1 is used as the boundary condition defining the solution within the layer. This gives us the solution

$$p_2(x,z,t) = P_2(k_x,z,\omega)\exp(j(k_x x-\omega t)), \tag{3.10}$$

with

$$P_2(k_x,z,\omega) = P_1(k_x,\omega)\alpha_1(k_x,d_1,\omega)\alpha_2(k_x,z-Z_1,\omega). \tag{3.11}$$

By proceeding in a similar way for the remaining layers, we find that the component can be extrapolated to a general point within layer l using eq. (3.6) with

$$P_l(k_x,z,\omega) = P_1(k_x,\omega)\alpha_l(k_x,z-Z_{l-1},\omega)\prod_{q=1}^{l-1}\alpha_q(k_x,d_q,\omega). \tag{3.12}$$

Note again that transmission losses at the interfaces are neglected. A correction for these can easily be included in the model but for the purpose of imaging and with the relatively small angle of divergence for the transducer used in this work, such a correction is of limited value; see further comments in Appendix 3.A.1.

The multiplication by $\alpha(\cdot)$ represents a phase shift and it is from this relation *phase shift migration* has gotten its name. Eq. (3.12) describes the relation between the 2D Fourier transform of the field observed at $Z_0=0$, and the 2D Fourier transform of the field that would have been measured at $z\neq 0$, had the sensors been placed at that particular depth instead of Z_0. Thus, $p_l(x,z,t)$ can be recovered by a 2D inverse Fourier transform.

Consider now an exploding reflector at the particular depth, z, identical with the depth of a hypothetical sensor plane. Since the vertical distance between the sensor plane and the reflector then is zero, the contribution from the reflector will appear at $t=0$. Moreover, compared to any other observation time, the field originating from the reflector will be maximally concentrated in space at $t=0$. This holds regardless of x-position and we realize that by simply reading out the field at time $t=0$ from $p_l(x,z,t)$ for all points at the same depth, z, we will obtain a

[2]See Appendix 3.A.2 concerning the sign conventions used in the Fourier transform.

horizontal image line that has optimal lateral resolution. Time $t = 0$ is sometimes called the *imaging condition* for this scenario.

The inverse Fourier transform for obtaining $p(x, z, t = 0)$ is

$$p_l(x, z, t = 0) = \int\int P_l(k_x, z, \omega) e^{jk_x x} dk_x d\omega, \tag{3.13}$$

where we have used that $e^{-j\omega t} = 1$ for $t = 0$. The integral can be evaluated by first integrating $P_l(k_x, z, \omega)$ over ω, followed by a 1D inverse Fourier transform over k_x.

Finally, note that eq. (3.12) allows for an efficient recursive computation within each layer. If we have $P_l(k_x, z, \omega)$, we can obtain $P_l(k_x, z + \Delta z, \omega)$ with z and $z + \Delta z$ using

$$P_l(k_x, z + \Delta z, \omega) = P_l(k_x, z, \omega)\alpha_l(k_x, \Delta z, \omega) \tag{3.14}$$

so if we choose an image grid that is regular in z, the factor $\alpha_l(k_x, \Delta z, \omega)$ will be the same for each image line within layer l, meaning that it can be pre-calculated and stored in a lookup table to speed up the computations.

Adaptations to the case of pulse-echo measurements.

The phase shift migration equations were derived assuming an exploding reflector model and this model must be adapted to the monostatic case. The sound paths in the pulse-echo measurements are twice as long as those in an exploding reflector scenario so the pulse-echo measurements can be translated into an analogous exploding reflector scenario by simply dividing the physical sound speed by two.

As a consequence, the phase shift factor should for the monostatic case be redefined as

$$\alpha_l(k_x, \zeta, \omega) = \exp\left\{-j\zeta\sqrt{\frac{4\omega^2}{c_l^2} - k_x^2}\right\}. \tag{3.15}$$

Another deviation from the above presented theory is that the field measurements are influenced by the transducer characteristics. The electro-acoustical properties of the transducer affect the measured signal both at transmission and reception and the overall effect is that the received signals become band pass filtered and, more importantly, phase delayed. If these delays are not compensated for, the imaging condition $t = 0$ will be poorly synchronized with the waves resulting from a scatter at z, and this will cause a deterioration of the lateral resolution.

A simple way to compensate for these phase delays is to correlate the received signals with the double path impulse response of the transducer[3] which is the method chosen here. After the correlation, the maximum peak of an echo from a small reflector at a certain range will appear correctly synchronized with the two-way travel time predicted by the range. A good approximation of this impulse response used in the correlation is obtained by measuring the response from a reflector in the far field, parallel to the transducer surface [24], and the correlation is conveniently performed in the frequency domain for each acquired signal, $s(x_n, Z_0, t)$, as

$$P_C(x_n, Z_0, \omega) = S(x_n, Z_0, \omega)H_{tr}^*(\omega), \tag{3.16}$$

where $S(x_n, Z_0, \omega)$ is the Fourier transform of $s(x_n, Z_0, t)$ and $H_{tr}^*(\omega)$ is the complex conjugate of the Fourier transform of the double path transducer impulse response, $h_{tr}(t)$.

[3]The double path impulse response is a convolution between the electro-mechanical impulse response in transmit and the mechanical-electrical in receive.

We should note yet another deviation between reality and the assumptions used in the derivation. Since the diameter of the planar transducer is larger then the involved wave lengths, only the field from a limited set of angles centered around the normal to the transducer surface is sensed. Thus, the field that is processed is not the true field at the scanning surface but a spatially filtered version of it. Since the resolution in the reconstructed image is inversely proportional to the spatial bandwidth, and this bandwidth, in turn, is inversely proportional to the aperture of the sensor, the resolution will be proportional to the aperture. This is in accordance with the results presented in [25], showing that the resolution in synthetic aperture imaging is approximately $D/2$ where D is the aperture of the sensor. See Appendix 3.A.3 for further details on the theoretically predicted resolution.

Summary of the algorithm

The algorithm summarized in this section aims at reconstructing an $N_z \times N_x$ image from points on a regular grid in a region of interest (ROI) that is defined as the rectangle $z \in [z_{min}, z_{max}]$, $x \in [x_{min}, x_{max}]$. In the following we let z^p denote the z-coordinates of the pth horizontal image line.[4] These lines are separated by a distance $\Delta z = (z_{max} - z_{min})/(N_z - 1)$ and we have that $z^p = z_{min} + (p-1)\Delta z$. In a similar way, the N_x vertical image lines are separated by the spatial sampling distance Δx.

Let $p_C(x_n, Z_0, t)$ denote a signal acquired at the transducer position x_n, which has been correlated to the transducer double path impulse response as described in eq. (3.16). The 2D phase shift migration algorithm can be summarized as follows:

1. Apply a 2D fast Fourier transform (FFT) to the data:
   $P_1(k_x, \omega) = P_1(k_x, Z_0, \omega) \leftarrow \mathrm{FFT}_{tx}\{p_C(x, Z_0, t)\}$, where the subscripts on the FFT indicates which variables are transformed.
2. If z_{min} is not zero, use eq. (3.12) to compute $P(k_x, z_{min}, \omega)$.
3. Set $z^1 = z_{min}$ and do the following for all image lines $p = 1$ to N_z:
   (a) Compute $p(x, z^p, t = 0)$ by first summing $P(k_x, z^p, \omega)$ over ω,
   $$P(k_x, z^p) = \sum_{\omega} P(k_x, z^p, \omega) \tag{3.17}$$
   followed by a 1D inverse fast Fourier transform:
   $$p(x, z^p, t = 0) \leftarrow \mathrm{IFFT}_x\{P(k_x, z^p)\}, \tag{3.18}$$
   and assign $p(x, z^p, t = 0)$ to the p:th horizontal image line.
   (b) If z^p and z^{p+1} both belong to the same layer, l, use eq. (3.14) to compute $P(k_x, z^{p+1}, \omega)$ for all values of k_x and ω. Else, if z^p belongs to l and z^{p+1} belongs to $l+1$, compute $P(k_x, z^{p+1}, \omega)$ in two steps as
   $P(k_x, z^{p+1}, \omega) = P(k_x, Z_l, \omega)\alpha_{l+1}(k_x, z^{p+1} - Z_l, \omega)$ with
   $P(k_x, Z_l, \omega) = P(k_x, z^p, \omega)\alpha_l(k_x, Z_l - z^p, \omega)$.

Again note that the phase factors, $\alpha(\cdot)$, appearing in steps 2 and 3(b) should be for the monostatic case as defined in eq. (3.15).

Since going from continuous to discrete data may introduce aliasing problem, zero-padding is generally required to avoid this. See Appendix 3.A.4 for a discussion on aliasing issues in both the temporal and spatial domains.

[4] Please note the distinction between superscripts identifying the image lines and the subscripts used to identify layer interface coordinates

3.1.3 Experiments

Two experiments were performed. The first aimed at demonstrating the method's ability to treat a scenario with scatterers residing in two layers having different sound speeds. This experiment was performed with a copper block immersed in water and containing a number of side drilled holes (SDHs). A wire target was placed in the water in front of the block, in this way creating a scenario with scatterers present both in the slow water media, with $c_1 = 1480$ m/s, and in the fast copper media, with $c_2 = 4690$ m/s. The second experiment aimed at demonstrating how the method can be used with immersion test data to improve the resolution in C-scans and improve the amplitude contrast between isolated reflectors and the contributions from grain scattering. In this experiment the test object was a copper block with flat bottom holes (FBHs).

Immersion measurements of copper block with SDHs and a wire target in water

The immersion test setup used in the first experiment is shown in Fig. 3.2. A planar circular 2.25 MHz transducer from Panametrics with 10 mm diameter was scanned along the x-axis and pulse-echo measurements were acquired at positions $x_1, ..., x_{210}$ that were separated by $\Delta x = 1$ mm. The inspected object containing SDHs was placed with its front surface in the horizontal plane.

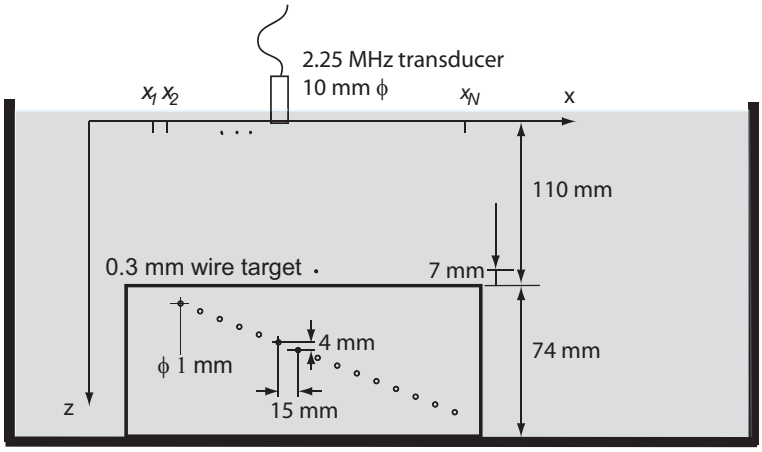

Figure 3.2: Schematic setup for immersion testing of the copper block containing SDHs. The ultrasonic transducer was scanned in the x-direction and pulse-echo measurements were performed at discrete locations $x_1, ..., x_N$ that were separated by $\Delta x = 1$ mm.

The acquired data is presented in Fig. 3.3(a) as an envelope B-scan, obtained by Hilbert transformation of the raw data. The front surface echo is seen at approximately $t = 150\,\mu s$ corresponding to the water path of approximately 110 mm and the wire target can be seen at $x = 110$ mm at $t = 140\,\mu s$. A secondary echo from the wire is also seen at $t = 160\,\mu s$ at the same scanning position. It corresponds to a sound path transducer-Cu-wire-Cu-transducer. The SDHs are seen as hyperbolic patterns at various depths.

In Fig. 3.3(b), the image reconstructed using phase shift migration is presented. In this image, in which the horizontal image lines are separated by $\Delta z = 0.1$ mm, the responses from the SDHs are concentrated to small spots and the same holds for the wire target. Note that a geometrical correction is obtained through the migration since the method takes into account the different sound speeds at different layers. Thus, the wire target's distance between to the front surface of the block can be correctly measured in the image to be 7 mm. Due to the shorter wavelength in water, the wire target has a better vertical resolution than the SDHs in

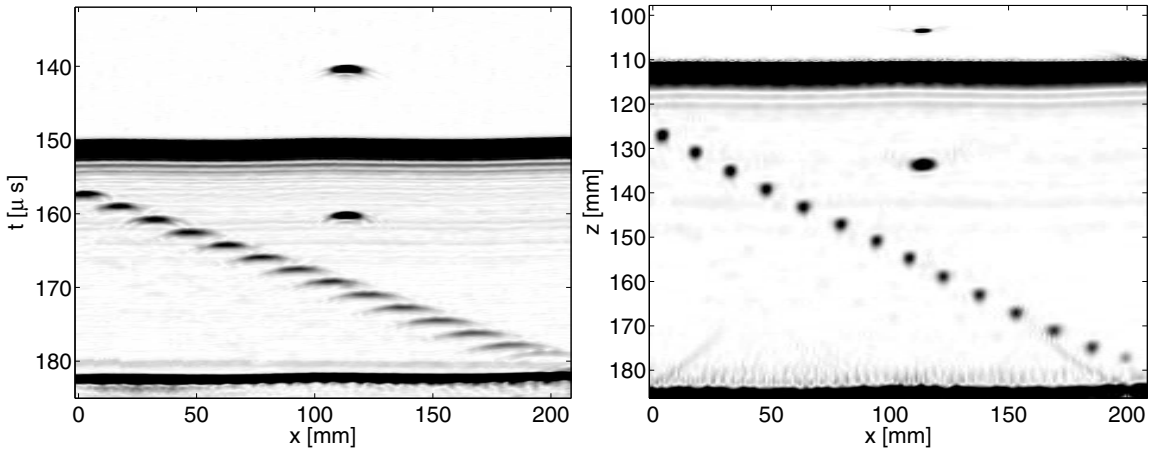

(a) (b)

Figure 3.3: (a) The B-scan from the copper block with SDHs and with a wire target in front of the upper surface. (b) Result from phase shift migration.

the copper block. Note also that the lateral resolution of the SDHs is approximately uniform throughout the entire object.

The diffuse spot centered at $x = 110$ mm and $z = 132$ mm corresponds the above mentioned double reflection Cu-wire-Cu. Since multiple reflections are not taken into account in the development of the method, such echoes generally lead to blurred artifacts as the one seen here.

The lateral resolution can be further examined in Fig. 3.4, where local profile plots for the SDHs as well as the wire target are shown both for the B-scan and the reconstructed image. These profiles were obtained by calculating the maximum amplitudes within a depth interval covering the target of interest and projecting the values onto the x-axis. For ease of comparison, the profiles have been normalized to the same maximum amplitudes.

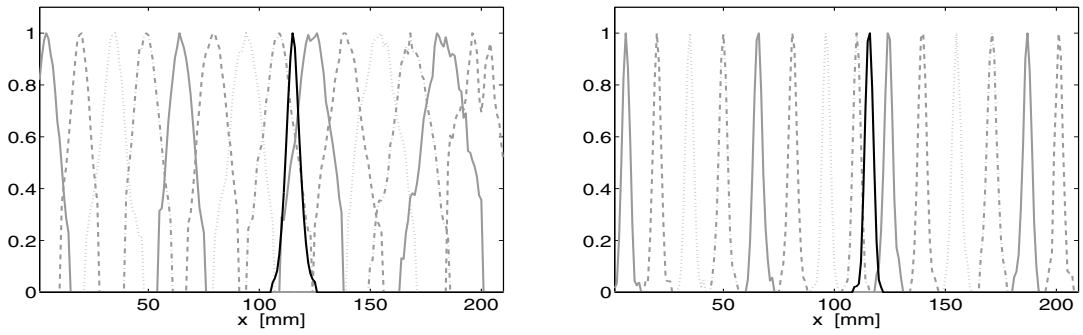

(a) B-scan (b) Phase shift migration

Figure 3.4: Profile plots of the SDHs and the wire target in (a) the original B-scan and (b) the reconstructed image. The profiles of SDHs are shown grey with various line styles to separate visually and the wire target is shown as a solid black line.

Inspection of the profile plots confirms the conclusion that the lateral resolution in the reconstructed image is practically independent of the depth. This holds also for the wire target which is surrounded by a medium with a different sound speed than the SDHs. If we define the resolution to be the length of the cross section at 50% of the maximum of the amplitude, we get a resolution that is approximately 5 mm for both the holes and the wire target. This is

in accordance with the results for synthetic aperture imaging [25], stating the resolution to be approximately $D/2$ for a sensor with an aperture of D. Here we have $D = 10$ mm.

Immersion test of copper block with FBHs

In the second experiment, a volume scan of a copper block with FBHs was performed. The dimensions of the block are shown in Fig. 3.5 and the scanning was conducted at a distance of 41 mm above the block. The purpose of the experiment was to illustrate the improvements in detectability and lateral resolution that can be achieved through the method. The block had a grainy structure that caused both strong back scattering noise as well as sound attenuation and the responses of the FBHs were therefore relatively difficult to detect in standard B-scans. Only the 4 mm diameter FBH gave a response strong enough to be easily detected in those images.

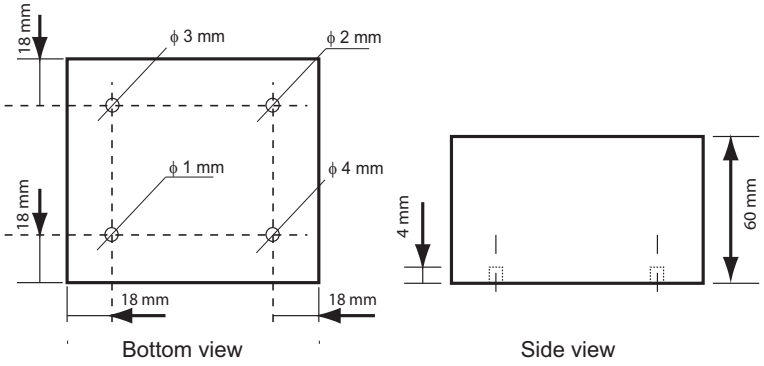

Figure 3.5: Copper block with four FBHs.

Figures 3.6 and 3.7 show two examples of envelope B-scans from the data set along with the corresponding reconstructed images. Fig. 3.6 shows an extracted B-scan over the 1 mm and 4 mm FBHs. The 1 mm hole is not seen at all but the response from the 4 mm FBH can be seen at an interval around $x = 82$ mm and $t = 82\mu s$. Note that the width of the response is approximately 15 mm. In the corresponding reconstructed image, the response from the 4 mm FBH at around $z = 97$ mm[5] is reduced in size significantly.

Fig. 3.7 shows an extracted B-scan over the 2 mm and 3 mm holes and we can see weak responses from these holes at around $t = 82\mu s$, for x around 18 mm and 80 mm, respectively. The 3 mm and 2 mm FBHs at around $z = 97$ mm in the corresponding reconstructed image are better localized in the x-direction thus providing better conditions for extracting a C-scan.

C-scan images from the depth interval covering the FBHs in the Cu-block were extracted from the raw data as well as from the reconstructed images by projecting the maximum amplitude values within the interval onto the $x - y$ plane. The depth interval of interest corresponds to the interval $z \in [95, 99]$ mm when the water path is taken into account. In the C-scans that are presented in Fig. 3.8, the FBHs of diameters 2, 3, and 4 mm are visible in both C-scans but the resolution is much improved in the C-scan based on the migrated data. In particular, the 3 mm diameter FBH is in the original C-scan partly masked by disturbances caused by early parts of the back wall echo entering the time window of interest. In the migrated C-scan, these disturbances are less prominent and the true position of the FBH is more easily found.

Note that the improvement in resolution only concerns the direction of migration; the migration has not significantly improved the resolution in the y-direction.

[5]Note that the water path is included in the z measure.

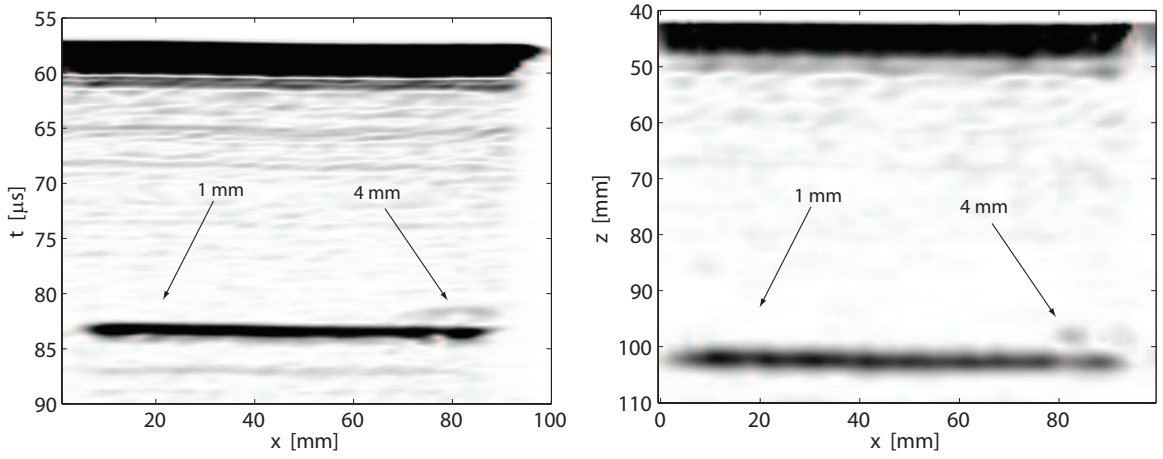

(a) (b)

Figure 3.6: (a) Original B-scan acquired at $y = 18$ mm passing over the 1 mm and 4 mm FBHs. (b) Image resulting from phase shift migration. The response of the 1mm FBH is too weak to be seen.

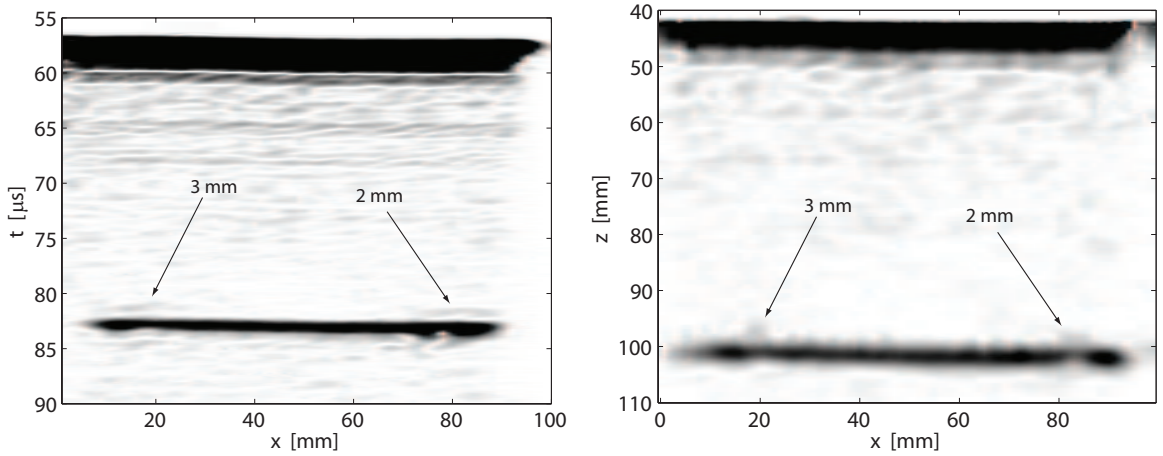

(a) (b)

Figure 3.7: (a) Original B-scan acquired at $y = 63$ mm passing over the 3 mm and 2 mm FBHs. (b) Image obtained by migration of the B-scan.

Both C-scans in Fig. 3.8 have been normalized with respect to their maximum pixel value providing a fair comparison of the noise level in the images and we note that phase shift migration has improved the signal-to-noise ratio, resulting in a better contrast.

3.1.4 Conclusions and discussion

Phase shift migration has been proposed for ultrasonic imaging of objects immersed in water and the algorithm has been demonstrated to correctly treat media with different sound speeds and to yield images with an improved lateral resolution under such conditions.

The experiment with the copper block with SDHs, showed that the lateral resolution in the reconstructed image is independent of depth to a good approximation. It was also demonstrated using data from a block with FBHs that the phase shift migration, along with the improvement in resolution, helps in improving the amplitude contrast between isolated reflectors and the

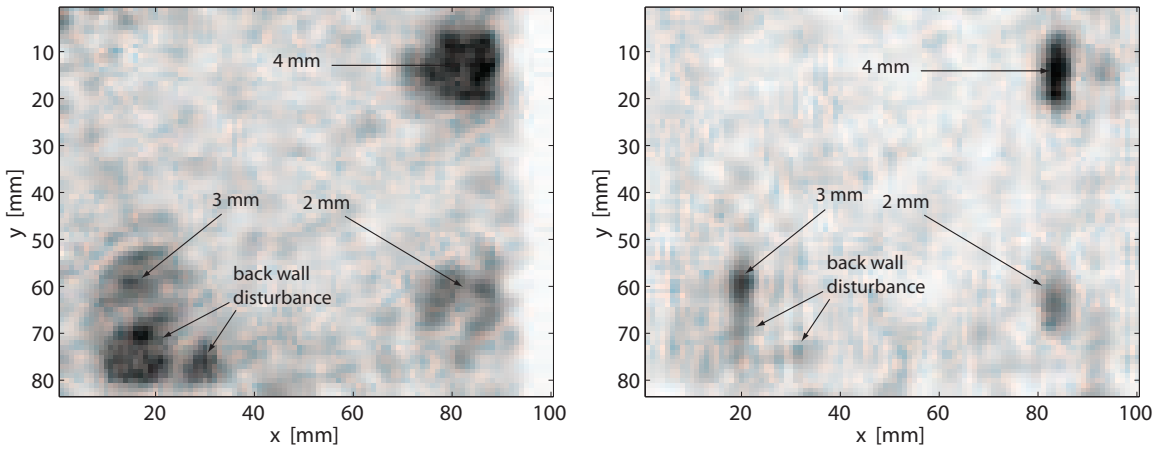

(a) (b)

Figure 3.8: C-scan based on (a) raw data and (b) migrated data. Note that the C-scans are seen from a top view with the 4 mm diameter FBH seen at the upper right corner.

contributions from grain scattering and, thus, is a useful tool for the detection of defects that are buried deeply in grainy materials.

The method considers longitudinal propagation only and any contribution associated with shear waves are neglected. Two facts motivate this approximation: First, the velocity of shear waves is around half of the velocity of the longitudinal which means that the contributions from the two modes appear well separated in time, at least for deeply buried reflectors. Second, the echo transmittance for shear waves is very small compared to the longitudinal. See Appendix 3.A.1 for numerical examples of the relative strengths of the mode components for the experiments presented in the paper.

The algorithm is implemented using FFT routines and the current implementation allows processing of the B-scans that takes less time than the data acquisition. As an example, the acquisition time of the B-scan, of size 1325×210, used in the experiments presented in the first part Section 3.1.3 was approximately 3 minutes whereas the processing time was 3.5 s on a dual core 2.80 GHz laptop. Finally, we note that the method can be straightforwardly extended to processing of 3D data, thus allowing for simultaneous improvement in both the lateral dimensions.

3.2 Extension to 3D data

The material presented in Section 3.1 was restricted to the migration of 2D data only. The migration concept can, however, straightforwardly be extended to 3D data and this extension is described here. 3D data is collected by acquiring A-scans at a scanning grid in the xy-plane and the extension to processing 3D data has the benefit of improving the resolution in both these lateral directions. This, however, comes at the cost of increased computational and memory demands. By organizing the computations in different ways, it turns out that we can trade between computational efficiency and memory requirements and we here propose two different algorithm implementations of which the first is suitable for fast processing on a powerful computer with a large internal memory and the second is slower but more memory efficient and can be run on most commonly available computers.

Due to the close relation between 2D and 3D migration, there is some overlap between the presentation here and that given in Section 3.1, both regarding theory and experiments. However, in this section, more algorithmic details are given and the computational complexity as well as the image resolution are examined in more detail.

The steps for modifying the 2D phase shift migration to the 3D case are given below in Section 3.2.1. This is followed in Section 3.2.2 by a summary of the two proposed algorithm implementations together with an analysis of the asymptotic computational complexity of these. A series of experiments are presented in Section 3.2.3 and the results from these are concluded in Section 3.2.4.

3.2.1 Extending the 2D algorithm to 3D

We here consider a scenario similar to that described in Section 3.1.2, but with the exception that the field is a function of all three space coordinates, i.e., we here represent the field by $p(x, y, z, t)$. Within the l:th layer, the scalar wave equation can be written as

$$\left[\frac{\partial^2}{\partial x^2} + \frac{\partial^2}{\partial y^2} + \frac{\partial^2}{\partial z^2} - \frac{1}{c_l^2}\frac{\partial^2}{\partial t^2}\right] p(x, y, z, t) = 0. \tag{3.19}$$

By decomposing the field into plane harmonic wave components, which now depend on wave number components k_y also, and following the same line of arguments as those leading to eqs. (3.3) and (3.4), we obtain the dispersion relation

$$k_{l,z} = -\sqrt{\frac{\omega^2}{c_l^2} - k_x^2 - k_y^2}, \quad \text{with } \frac{\omega^2}{c_l^2} \geq k_x^2 + k_y^2. \tag{3.20}$$

Thus, the wave number component $k_{l,z}$ in the 3D case depends on ω, k_x and k_y instead of only ω and k_x, as in the 2D case and the basic field extrapolation relation for 3D becomes[6]

$$P_l(k_x, k_y, z, \omega) = P_1(k_x, k_y, \omega)\alpha_l(k_x, k_y, z - z_{l-1}, \omega) \prod_{q=1}^{l-1} \alpha_q(k_x, k_y, d_q, \omega), \tag{3.21}$$

where $\alpha(\cdot)$ in the 3D case is defined as

$$\alpha_l(k_x, k_y, \zeta, \omega) = \exp\left\{-j\zeta\sqrt{\frac{4\omega^2}{c_l^2} - k_x^2 - k_y^2}\right\}, \tag{3.22}$$

[6] c.f. eq. (3.12)

if we take into account the adaptation to the pulse-echo scenario, as in eq. (3.15). Note again that since we only restrict our attention to propagating waves, only triplets of ω, k_x, and k_y that yield a positive expression inside the square root in eq. (3.22) are considered. The remaining are nulled out in the processing.

Similar to the 2D case, the imaging condition is $t = 0$. The difference is that we now, for each depth z, obtain an image cross section instead of a line. This cross section is obtained as

$$p_l(x, y, z, t = 0) = \int\int\int P_l(k_x, k_y, z, \omega) e^{jk_x x} e^{jk_y y} dk_x dk_y d\omega, \tag{3.23}$$

for z belonging to layer l.

Finally, a somewhat more refined analysis of the resolution than that given in Section 3.1, taking into account the circular shape of the transducer, leads to the following theoretically predicted lateral resolution in the restored images:

$$\delta_{x,y} = \frac{D}{2 \cdot 1.22} \approx 0.41D \tag{3.24}$$

where D is the diameter of the transducer. See Appendix 3.A.3 for details.

3.2.2 Algorithm implementations

The computation involved in the phase shift migration can be organized in several ways, leading to different implementations. We here present two different implementations of 3D phase shift migration algorithms. The first of these requires a large data set to be stored in memory during processing but is computationally faster, making it suitable for powerful computers with large internal memory. The second is computationally slower, but more memory efficient. Apart from possible differences caused by numerical round-off errors, the two algorithms give identical results.

The algorithms both take advantage of the the fact that the transmitted pulses and, thus, the received signals are limited to a frequency pass band between f_{low} and f_{high}. Furthermore, the computations are performed on negative frequencies only[7]; the positive frequencies are nulled out.

We let $s(x_m, y_n, Z_0, t_i)$ denote the A-scan acquired at transducer position (x_m, y_n, Z_0), for $0 \leq i \leq N_t - 1$, where N_t is the number of time samples recorded in each A-scan. The sampling period is denoted by Δt. The A-scans are stored in a three dimensional array of size $N_x \cdot N_y \cdot N_t$, where N_x and N_y are the number of points in the $x-$ and $y-$ directions, respectively. These points are separated by the spatial sampling distances Δx and Δy. The reconstruction results in a new data block of size $N_x \cdot N_y \cdot N_z$, where the number of z-values, N_z, can be chosen arbitrarily. These are separated in depth by Δz, which is also chosen by the user. Together, N_z and Δz determine the height of the ROI.

As in the 2D case, zero-padding must be applied to avoid aliasing, and a correlation between the A-scan and the double path transducer impulse response, $h_{tr}(k)$, should be performed in order to compensate for the phase delays introduced to the signals by the transducer, see Section 3.1.2. The correlation is conveniently performed in conjunction with the nulling out of positive frequencies. The two preprocessing steps are performed as follows:

[7] Acoustics and electrical engineering use different sign conventions for Fourier transforms. Due to these differences, there is a risk of confusion when discussing positive or negative frequencies. See Appendix 3.A.2 for comments on the sign conventions used in the FFT:s

1. To avoid aliasing, zero-pad the data in all three dimensions:

$$s_{zp}(x_m, y_n, Z_0, t_i) = \begin{cases} s(x_m, y_n, Z_0, t_i) & \text{for } \begin{cases} m \in [0, N_x - 1] \\ n \in [0, N_y - 1] \\ i \in [0, N_t - 1] \end{cases} \\ 0 & \text{for } \begin{cases} N_x \leq m \leq N_{x,zp} \\ N_y \leq n \leq N_{y,zp} \\ N_t \leq i \leq N_{t,zp}, \end{cases} \end{cases} \tag{3.25}$$

   where $N_{x,zp}$, $N_{y,zp}$ and $N_{t,zp}$ are the numbers of points in the x-, y- and z-directions after zero padding. For a discussion on the aliasing effects and how to choose the number of appended zeros, see Appendix 3.A.4.

2. For each nonzero A-scan in the data cube, i.e., for $m = 0 \ldots N_x - 1$ and $n = 0 \ldots N_y - 1$, correlate the A-scan with the transducer impulse response and at the same time null out positive ω. This is done by first computing the discrete Fourier transform of $s_{zp}(x_m, y_n, Z_0, t_i)$ with respect to time

$$S(x_m, y_n, Z_0, \omega_s) \leftarrow \mathrm{FFT}_t \left\{ s_{zp}(x_n, y_n, Z_0, t_i) \right\}, \tag{3.26}$$

   yielding values at discrete $\omega_s \in [-\frac{\pi}{\Delta t}, \frac{\pi}{\Delta t}]$, in steps of $\Delta\omega = \frac{2\pi}{N_{t,zp}\Delta t}$, followed by the correlation combined with nulling out the positive side of the spectrum

$$P_C(x_m, y_n, Z_0, \omega_s) = \begin{cases} S(x_m, y_n, Z_0, \omega_s) H^*_{tr}(\omega_s) & \text{if } \omega_s < 0 \\ 0 & \text{otherwise,} \end{cases} \tag{3.27}$$

   where $H^*_{tr}(\omega_s)$ is the complex conjugate of the Fourier transformed $h_{tr}(t_i)$.

   At this stage we can reduce the data set in size by removing all frequency components outside the transducer frequency pass band, thus, leaving us with a data cube of size $N_{x,zp} \cdot N_{y,zp} \cdot \frac{BN_{t,zp}}{2\mathrm{Fs}}$, where $B = f_{high} - f_{low}$ is the bandwidth of the transducer and $\mathrm{Fs} = 1/\Delta t$ is the temporal sampling frequency

   Note that the data is usually acquired using a time gate which means that the time between transmission and the start of the measurement, t_0, is usually non-zero, and this must be taken into account in the processing. This is done by phase shifting each A-scan in the frequency domain, which can be combined with the correlation, and equation (3.27) then becomes

$$\begin{aligned} P(x_m, y_n, Z_0, \omega_s) &= \\ &= \begin{cases} S(x_m, y_n, Z_0, \omega_s) H^*_{tr}(\omega_s) \exp(-j\omega_s \cdot t_0 \cdot \mathrm{Fs}) & \text{if } \omega_s < 0 \\ 0 & \text{otherwise.} \end{cases} \end{aligned} \tag{3.28}$$

In summary, the preprocessing results in a 3D array, $P(x_m, y_n, Z_0, \omega_s)$, of size $N_{x,zp} \cdot N_{y,zp} \cdot \frac{BN_{t,zp}}{2\mathrm{Fs}}$ and this array is the input to the two algorithms. They both reconstruct an 3D image of the ROI that starts at depth z_{min} and has thickness $(N_z - 1)\Delta z$. The image planes obtained at each depth are below enumerated by p.

Algorithm 1

1. Apply a 2D FFT on $P(x_m, y_n, Z_0, \omega_s)$ along both x and y:

$$P(k_x, k_y, Z_0, \omega_s) \leftarrow \mathrm{FFT}_{xy} P(x_m, y_n, Z_0, \omega_s) \tag{3.29}$$

yielding values at discrete $k_x \in [-\frac{\pi}{\Delta x}, \frac{\pi}{\Delta x}]$ in steps of $\frac{2\pi}{N_{x,zp}\Delta x}$, and $k_y \in [-\frac{\pi}{\Delta y}, \frac{\pi}{\Delta y}]$ in steps of $\frac{2\pi}{N_{y,zp}\Delta y}$.

2. If the first z-value in the ROI is $z_{min} \neq 0$ and belongs to the l:th layer, use eq. (3.21) to migrate the data so that when the iteration over z^p starts, the initial z-value is z_{min}. The calculation should be done for triplets (ω_s, k_x, k_y) that satisfy $\frac{4\omega_s^2}{c^2} - k_x^2 - k_y^2 \geq 0$:

$$P(k_x, k_y, z = z_{min}, \omega_s) = P(k_x, k_y, Z_0, \omega_s)\alpha_l(k_x, k_y, z_{min} - Z_{l-1}, \omega_s) \prod_{q=1}^{l-1} \alpha_q(k_x, k_y, d_q, \omega_s) \tag{3.30}$$

3. Set $z^1 = z_{min}$ and do the following for all $p = 1 \ldots N_z$:

   (a) Calculate, for the same values of k_x, k_y and s as in item 2,

   $$P(k_x, k_y, z^{p+1}, \omega_s) = P(k_x, k_y, z^p, \omega_s)\alpha_l(k_x, k_y, \Delta z, \omega_s) \tag{3.31}$$

   where $z^{p+1} = z^p + \Delta z$.

   (b) Calculate the field $p(x, y, z^{p+1}, t = 0)$ by first summing $P(k_x, k_y, z^{p+1}, \omega_s)$ over ω_s,

   $$P(k_x, k_y, z^{p+1}, t = 0) = \sum_{\omega_s \in \Omega} P(k_x, k_y, z^{p+1}, \omega_s), \tag{3.32}$$

   where $\Omega = [-2\pi f_{high}, -2\pi f_{low}]$, followed by a 2D inverse Fourier transform:

   $$p(x_m, y_n, z^{p+1}, t = 0) \leftarrow \text{IFFT}_{k_x,k_y} \left\{ P(k_x, k_y, z^{p+1}, t = 0) \right\}, \tag{3.33}$$

   and assign $p(x_m, y_n, z^{p+1}, t = 0)$ for $m = 1...N_x$ and $n = 1...N_y$, to the $(p + 1)$:th image cross section.

Algorithm 2

In algorithm 2, the frequency components are processed in sequence, instead of processing the entire data cube at the same time and the contributions from each frequency component are accumulated. In this way, the 3-dimensional data cube is broken down into a set of 2-dimensional matrices which reduces the memory requirements considerably. The disadvantage is that the computations become more time consuming.

The algorithm can be described as follows:

1. Allocate a three-dimensional array with zeros of size $N_{x,zp} \cdot N_{y,zp} \cdot N_z$ for the reconstructed data cube:

   $$Res = \text{zeros}(N_{x,zp}, N_{y,zp}, N_z). \tag{3.34}$$

2. Loop over each frequency component $\omega_s \in \Omega$. For the current ω_s, extract the two-dimensional matrix of size $N_{x,zp} \cdot N_{y,zp}$ that contains the $x-$ and $y-$values for that frequency, and do the following:

   (a) Perform a 2-dimensional Fourier transform of the matrix:

   $$P(k_x, k_y, Z_0, \omega_s) \leftarrow \text{FFT}_{xy} \left\{ p(x_m, y_n, Z_0, \omega_s) \right\} \tag{3.35}$$

(b) If $z_{min} \neq 0$ and belongs to the l:th layer, use eq. (3.21) to migrate the data so that when the iteration over z^p starts, the initial z-value is z_{min}. The calculation should be done for $k_x \in [-\frac{\pi}{\Delta x}, \frac{\pi}{\Delta x}]$ and $k_y \in [-\frac{\pi}{\Delta y}, \frac{\pi}{\Delta y}]$, satisfying $k_x^2 + k_y^2 < 4\omega_s^2/c_l^2$:

$$P(k_x, k_y, z_{min}, \omega_s) = P(k_x, k_y, Z_0, \omega_s)\alpha_l(k_x, k_y, z_{min} - Z_{l-1}, \omega_s) \prod_{q=1}^{l-1} \alpha_q(k_x, k_y, d_q, \omega_s). \tag{3.36}$$

(c) Set $z^1 = z_{min}$ and do for all $p = 1 \ldots N_z$:

i. Calculate, for the same values of k_x and k_y as in item 2b

$$P(k_x, k_y, z^{p+1}, \omega_s) = P(k_x, k_y, z^p, \omega_s)\alpha_l(k_x, k_y, \Delta z, \omega_s) \tag{3.37}$$

ii. Calculate the contribution to the field from the frequency component ω_s by a 2D inverse Fourier transform

$$p_s(x_m, y_n, z^{p+1}, t = 0) \leftarrow \mathrm{FFT}_{k_x,k_y}\left\{P(k_x, k_y, z^{p+1}, \omega_s)\right\}, \tag{3.38}$$

and accumulate this to the $(p+1)$:th image cross section in Res:

$$Res(:, :, p+1) \leftarrow Res(:, :, p+1) + p_s(x_m, y_n, z^{p+1}, t = 0) \tag{3.39}$$

Computational complexity

We here examine how the computational complexity grows with the size of the data sets. For simplicity we consider only the asymptotic behavior and ignore the proportionality factors since these, to a large extent, depend on the particular computer on which the computations are performed. The Big-O notation is used to express the rates of growth. In the following analysis we will use that, for a fixed chosen depth resolution, Δz, the number of image cross sections will be proportional to the number of recorded times samples, N_t. Similarly, the number of used frequency components will also be proportional to N_t.[8]

The computation times for the two algorithms described in section 3.2.2 are dominated by a few critical computations. In **Algorithm 1**, the most time consuming part is the phase shift in item 3a, where approximately 60 % of the computation time is spent, and evaluating the time this takes gives a good approximation for the overall computation time of the algorithm. The considered operation is an entry wise multiplication between two 3D arrays of sizes $N_{x,zp} \cdot N_{y,zp} \cdot \frac{BN_{t,zp}}{2\mathrm{Fs}}$ and it resides within a for-loop, with the number of iterations growing linearly with N_z. Using the proportional relation between N_t and N_z mentioned above, we get that the computational complexity of every iteration is $\mathcal{O}(N_{x,zp}N_{y,zp}N_z)$, and the whole algorithm will have complexity $\mathcal{O}(N_{x,zp}N_{y,zp}N_z^2)$.

In **Algorithm 2**, the operations that dominate the computation time are instead the large number of 2D Fourier transforms and the adding of contributions to the field in item 2(c)ii and of these two operations, the 2D Fourier transform has the largest complexity. The operations are found within a nested for-loop, one over ω_s that has a number of iterations that is proportional to N_z as discussed above, and one over z^p, thus, requiring N_z steps. This makes the total number of iterations proportional to N_z^2. The 2D FFT has complexity $\mathcal{O}(N_{y,zp}N_{x,zp}\log_2(N_{x,zp}N_{y,zp}))$, causing the time for each iteration to have complexity $\mathcal{O}(N_{x,zp}N_{y,zp}\log_2(N_{y,zp}N_{x,zp}))$ for large $N_{x,zp}$ and $N_{y,zp}$. Altogether, this means that the complexity of **Algorithm 2** is $\mathcal{O}(N_{x,zp}N_{y,zp}N_z^2\log_2(N_{y,zp}N_{x,zp}))$, which is a factor $\log_2(N_{y,zp}N_{x,zp})$ higher than for **Algorithm 1**.

[8] Although a fixed transducer frequency band width is considered, the number of frequency bins representing this band in the FFT will grow with growing N_t since the bins become more densely spaced for larger N_t.

3.2.3 Experiments

A number of experiments were performed to examine the performance of the algorithms in various aspects. The first experiment was performed using contact test data from the copper block with SDHs used earlier in Section 3.1.3. By using contact data, potential difficulties caused by refraction were avoided and this experiment partly served the purpose of verifying the 3D code. More importantly, the experiment served to illustrate how phase shift migration is typically unable of improving the resolution with scatterers residing in the nearfield or close to the nearfield-farfield limit of the transducer. Note that although 3D migration was performed, the setup was essentially that of a 2D scenario and conclusions about resolution improvement can only be drawn regarding the cross-hole direction, i.e., in the x-direction.

The second experiment was performed in immersion on the same block and it is rather similar to the experiment presented in 3.1.3, with the main difference being that 3D data and 3D migration is used rather than 2D. The experiment served the purpose of verifying that the extension to 3D introduced no unexpected computational artifacts. Moreover, a quantitative examination of the resolution in the x-directions is presented.

The two subsequent experiments aimed at analyzing the resolution improvements in both the x- and y-directions. The first of the two experiments was performed in immersion using data from an aluminium block with FBHs and the second used more challenging immersion test data from the copper block with FBHs that was used earlier in Section 3.1.3.

All processing in the above mentioned experiments were performed using **Algorithm 1**. The final experiment concerns computational aspects and the computation times for Algorithm 1 and 2 are compared to each other and matched to their respective predicted performances given by the above asymptotical complexity analysis.

Contact testing of a copper block with SDHs

In the first experiment, 3D migration was performed on data from a contact test with water acting as contact agent. The test object was the 74 mm thick copper block with 15 SDHs at descending depths, described earlier in Section 3.1.3. The holes were drilled 27 to 31 mm into the block. A circular planar contact transducer of diameter 15 mm and with a center frequency of 2.25 MHz and a bandwidth of 3.1 MHz was used in the experiment. It was scanned over an area of 230 mm in the x-direction, and 20 mm in the y-direction, with scanning steps $\Delta x = \Delta y$=1 mm. Approximately 12 mm of the holes' lengths were covered in the scan, see Figure 3.9, and 14 of the 15 holes were fully covered in x-direction. The front- and backwall echoes from the copper block were significantly stronger than echoes from the holes within the block and these were removed from the A-scans in order to avoid potential problems in the reconstruction caused by saturation in the A/D converter.

An envelope B-scan example extracted from the data cube at $y = 7$ mm is presented in Figure 3.10. The gathered data was processed with 3D phase shift migration and the result for $y = 7$ mm is shown in Figure 3.11, from which can be seen that the holes closest to the front surface of the copper block are not resolved as good as the holes deeper into the block. This is most probably associated with the holes with poorer resolution being in, or close to, the nearfield of the transducer. For a 2.25 MHz transducer with a diameter of 15 mm, transmitting into copper, we have a nearfield/farfield limit of 27 mm, see eq. (3.69) in Appendix 3.A.3, and we see that the holes at larger depths than this all have fairly uniform resolution.

Profile plots were created using both original and processed data for the same y-value, and these are shown overlaid in Figure 3.12. The halfpower resolution of the holes were estimated both before and after processing, and the results are summarized in table 3.1. In the profile

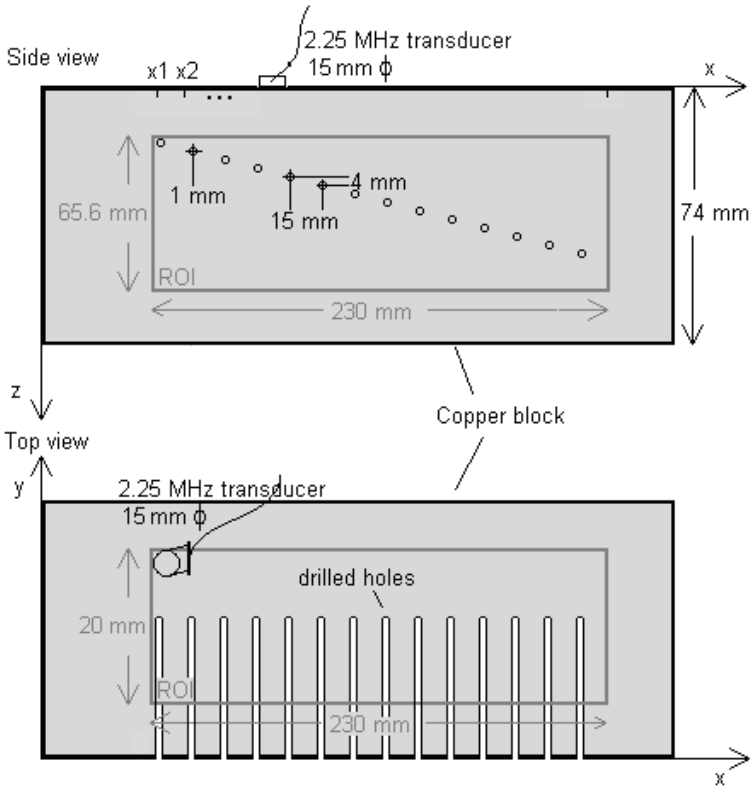

Figure 3.9: Experimental setup for contact testing of a copper block.

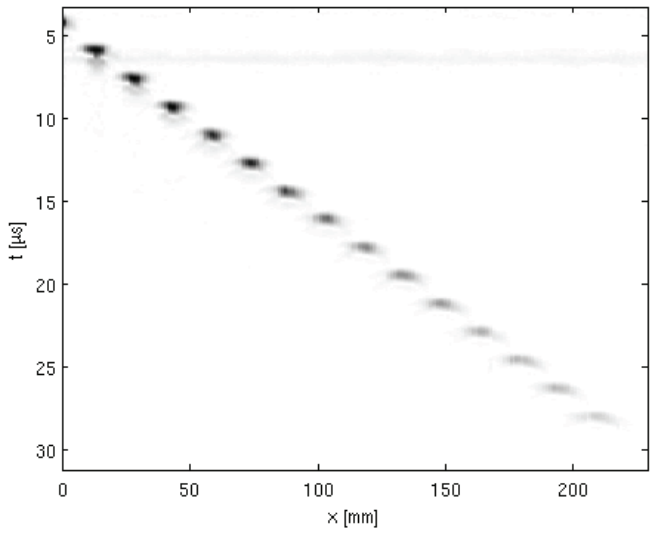

Figure 3.10: Original envelope B-scan of a copper block with 15 SDHs, of which 14 are fully covered by the transducer.

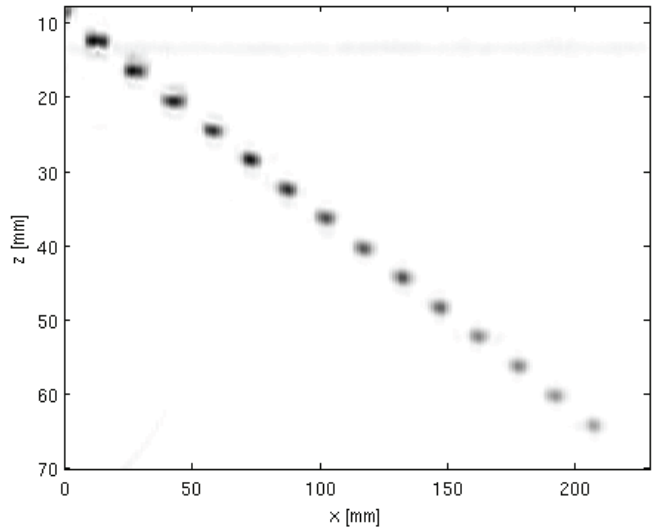

Figure 3.11: One cross-section of the results from 3D phase shift migration of the data collected from a contact scan of a copper block with SDHs.

plot, we see another example of the effects of having the scatterers residing in the nearfield of the transducer; the amplitudes of the profiles are not strictly decreasing with depth, as should be the case for scatterers in the farfield.

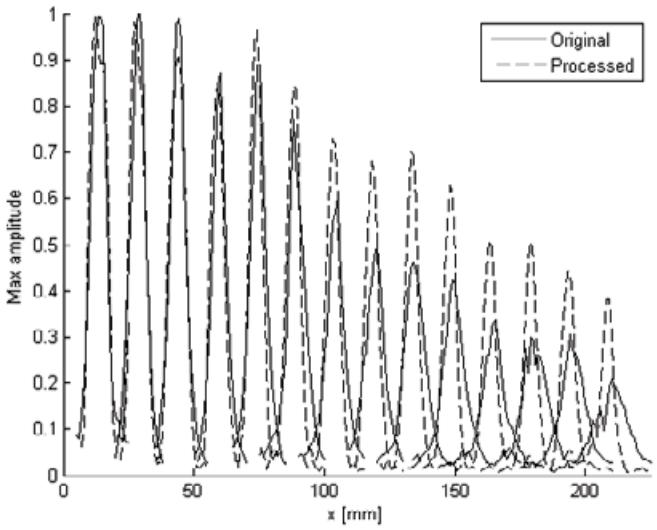

Figure 3.12: Profile plots for the original data in Figure 3.10 and the processed data in Figure 3.11

From table 3.1, it can be seen that the experimental resolution for the holes residing in the farfield is fairly close to the theoretically predicted resolution of $0.41D = 6.2$ mm.

Finally, C-scans were created using both sets of data. These are presented in Figures 3.13 and 3.14. By comparing these, we see that the improvement in resolution is most apparent in the x-direction and for the deeper holes. Although some improvement can be experienced also in the y-direction, we should note that the setup is not well suited for the evaluation of resolution improvement in this direction. One contributing fact is that the holes do not have flat bottoms and the ending points of the holes are therefore poorly defined.

Table 3.1: Estimated halfpower resolution in x-direction for SDHs in a copper block, each 1 mm in diameter, in the original data, and after processing with 3D phase shift migration. The theoretically predicted resolution is 6.2 mm.

Hole number	Original data $\delta_x[mm]$	After 3D phase shift migration $\delta_x[mm]$
1	7.6	8.5
2	6.9	7.4
3	6.8	7.9
4	6.3	6.6
5	6.9	6.1
6	7.2	6.2
7	7.2	6.3
8	8.5	6.1
9	9.7	6.0
10	9.3	5.9
11	8.8	5.9
12	11.2	5.7
13	9.7	6.3
14	14.3	5.3

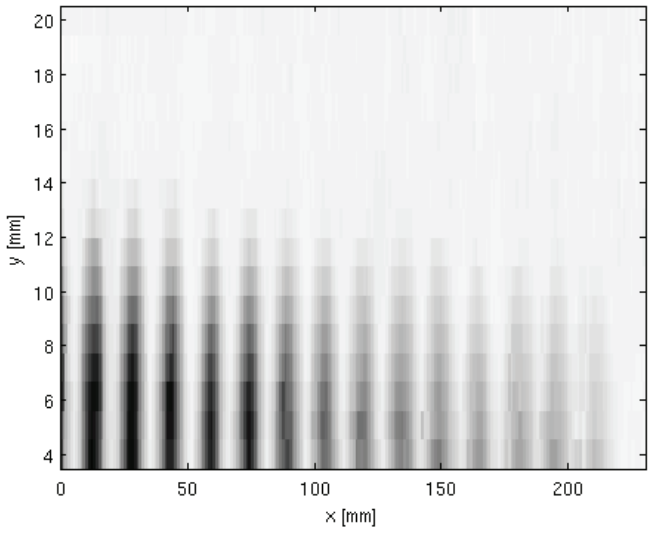

Figure 3.13: Original contact C-scan of a copper block with SDHs.

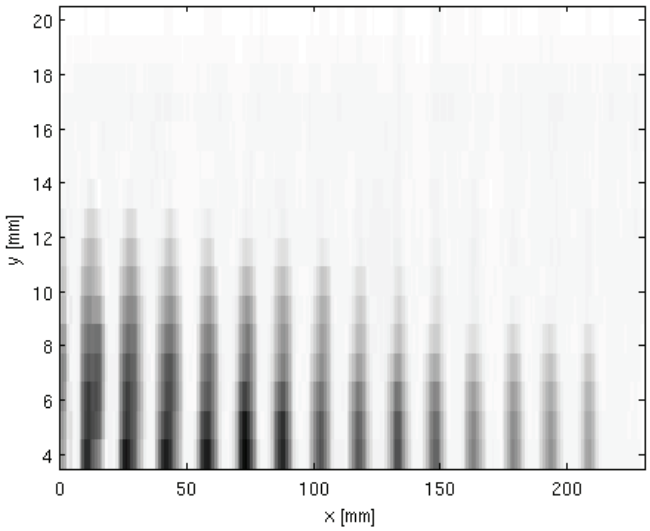

Figure 3.14: C-scan of a copper block with SDHs after 3D phase shift migration.

Immersion testing of a copper block with SDHs

In the second 3D experiment, the same copper block with SDHs as before was used but now the test was performed in immersion using the same transducer as in Section 3.1.3, with a diameter of 10 mm and a center frequency and bandwidth of, 2.25 MHZ and 1.5 MHz, respectively. The immersion setup is shown in Figure 3.15 and Figure 3.16 shows an example of an original envelope B-scan acquired at y=7 mm.

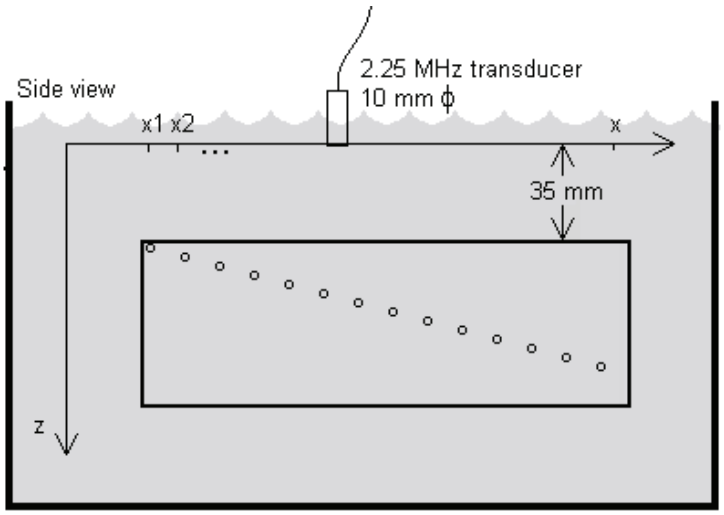

Figure 3.15: Setup for immersion testing of a copper block with 15 SDHs, of which 14 are fully covered by the transducer.

As discussed above, the setup with SDHs is not well suited for evaluating resolution in the y-direction and, therefore, we here present only results as cross sectional images in the zx-plane.

The gathered 3D data was processed and the result for the cross section at y=7 mm is shown in Figure 3.17. If we compare with the results presented in Figure 3.11 for the contact test, we note that the lateral resolution is fairly similar for holes at the different depth, in contrast to what we observed for the shallowest holes in the contact test. This observation further confirms the conclusion that the poor resolution of these holes is because they reside in the transducer nearfield.

As with the contact test, profile plots were made for both the original and the processed data, and these are shown overlaid in Figure 3.18. From these profile plots, the resolution in x-direction was estimated and the estimates are presented in table 3.2. There it can be seen that the experimental resolution is again fairly close to the theoretically predicted resolution of $0.41D$= 4.1 mm.

It can be seen in Figure 3.18, in this experiment the amplitude of the profiles is decreasing with depth, as would be expected as the holes reside in the farfield.

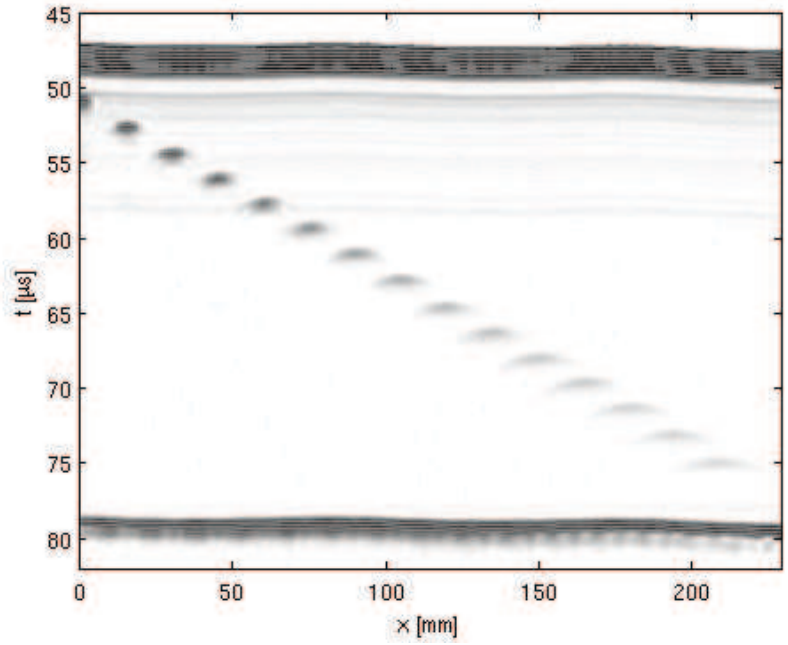

Figure 3.16: Original envelope B-scan from an immersion testing of a copper block with SDHs.

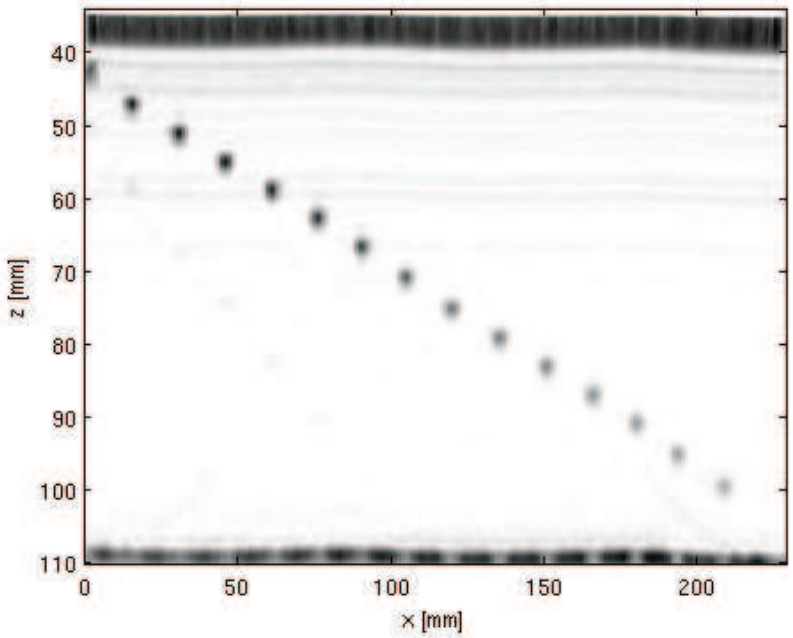

Figure 3.17: One cross-section of the results from 3D migration of the data collected in the experiment with an immersed copper block with SDHs.

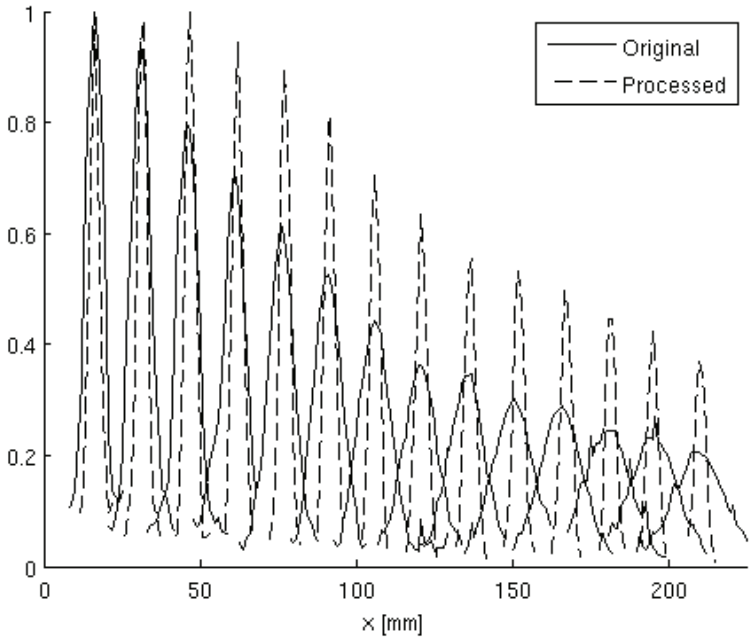

Figure 3.18: Profile plots for the original data in Figure 3.16 and the processed data in Figure 3.17

Table 3.2: Halfpower resolution in x-direction for SDHs in an immersed copper block, each 1 mm in diameter, in the original data, and after processing with 3D phase shift migration. The theoretically predicted resolution is 4.1 mm.

Hole number	Original data $\delta_x[mm]$	After 3D PSM $\delta_x[mm]$
1	7.1	4.1
2	8.0	4.2
3	8.1	4.2
4	8.3	3.7
5	9.4	4.1
6	11.3	4.2
7	12.4	4.2
8	12.9	4.4
9	13.5	4.4
10	15.2	4.3
11	16.1	4.3
12	17.9	4.1
13	16.3	4.2
14	21.2	4.3

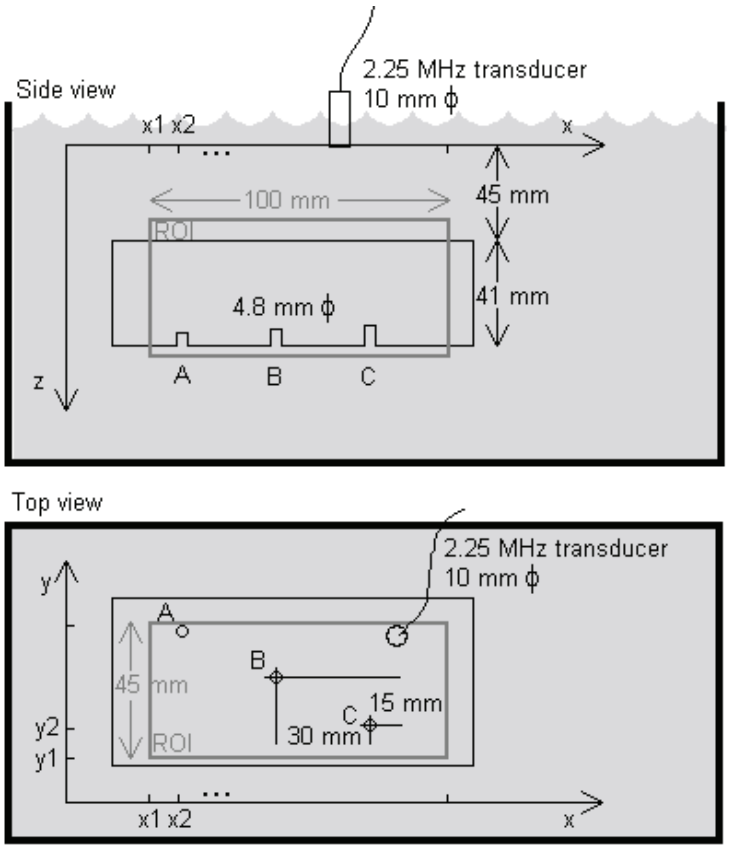

Figure 3.19: Experiment setup for immersion testing of an aluminium block with FBHs.

Immersion testing of an aluminium block with FBHs

To examine how resolution is affected, both in the x- and y-direction, when extending the frequency domain method from 2D to 3D, an immersion test was made on a 41 mm thick aluminium block illustrated in Figure 3.19. The block contained three FBHs, one (A) 2.6 mm into the block, (B) drilled 4.5 mm, and (C) drilled 8.3 mm. The holes all had a diameter of 4.8 mm.

Figure 3.20 shows a C-scan of the original data acquired in the experiment. The data was processed with 2D phase shift migration by processing the B-scans one by one along the x-axis, and a C-scan extracted from the result of this processing is shown in Figure 3.21. Figure 3.22 shows the results after 3D phase shift migration.

The resolution before and after the two different processings was estimated and the estimates are presented in table 3.3. from which can be seen that the resolution in y-direction after processing with the 3D algorithm is, as expected, much better than after processing with the 2D algorithm. In x-direction, the resolution after processing 2D data and 3D data is approximately the same. It can also be seen in the table that the hole named A has worse resolution than the other holes, which is due to that hole not being fully covered by the scan as seen in Figure 3.20, thus not benefitting from the full synthetic aperture as (B) and (C).

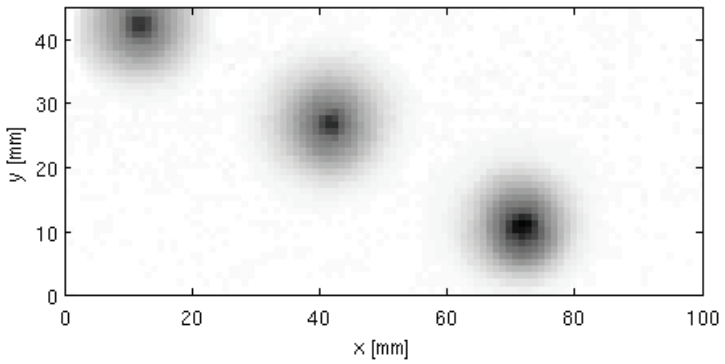

Figure 3.20: C-scan of the original data acquired from scanning an immersed aluminium block with FBHs.

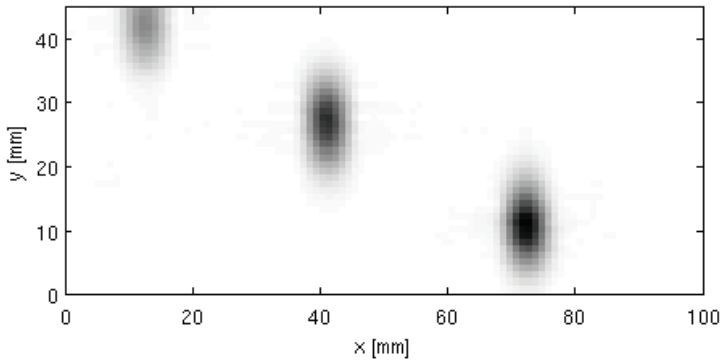

Figure 3.21: C-scan after 2D phase shift migration along the x-axis.

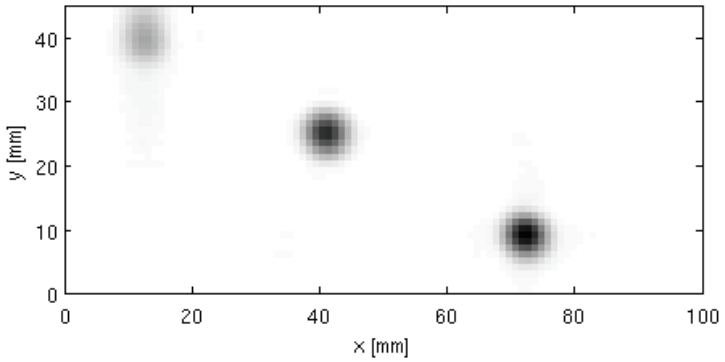

Figure 3.22: C-scan after 3D phase shift migration.

Table 3.3: Estimated halfpower resolution in x- and y-direction for FBHs in an aluminium block, each 4.8 mm in diameter, in the original data, and after processing with 2D and 3D phase shift migration. The theoretically predicted resolution is 4.1 mm.

Hole	Original data		After 2D PSM		After 3D PSM	
	δ_x [mm]	δ_y [mm]	δ_x [mm]	δ_y [mm]	δ_x [mm]	δ_y [mm]
A	8.3	8.5	6.1	10	5.9	7.3
B	8.9	9.2	5.4	10.9	5.4	5.4
C	7.8	8.7	5.3	9.9	5.4	5.4

Immersion testing of a copper block with FBHs

The aluminium block from the last section was fairly free from backscattering noise, with the FBHs clearly visible in the original data. To examine how the algorithm handles more challenging noisy data, an immersion test was done on the 60 mm thick copper block with four FBHs that was used in the experiments presented in Section 3.1.3 and is illustrated in Figure 3.5.

A C-scan was extracted from the original data acquired in the experiment, and is shown in Figure 3.23. In the C-scan, the 4 mm hole is clearly visible, and the 2 mm hole is discernable, though both are quite blurry. The 1 mm hole cannot be detected at all, and in the neighborhood of the nominal position of the 3 mm hole, there is a strong echo that does not originate from the hole, but is rather a contribution from the back surface echo. Since none of the holes are well defined in the C-scan, the estimates of resolution in the raw data image are very rough. The resolution for the 1 mm and the 3 mm holes could not be satisfactorily determined and they are not presented. The estimated resolution for the 2 mm and the 4 mm holes are presented in table 3.4.

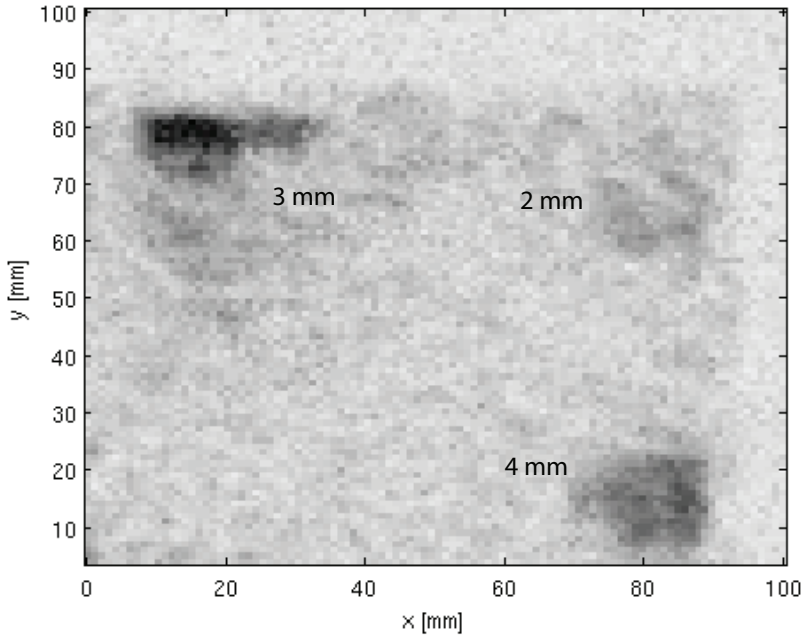

Figure 3.23: C-scan of the original data acquired from scanning an immersed copper block with FBHs.

The data acquired from the experiment was processed, both with 2D and 3D phase shift migration and the resulting C-scans after the respective processings are shown in Figures 3.24 and 3.25. It is obvious from the figures that the resolution in y-direction is significantly improved in the results after 3D migration compared to the results after 2D migration. The resolution, both in x- and y-direction was estimated for both results and presented in table 3.4.

It is worth noting that the strong contribution from the back surface echo in the original C-scan presented in Figure 3.23 is much less pronounced in the result after 2D processing, and still even weaker in the result after 3D processing. Although difficult to find in the original data, the 3 mm hole is clearly visible both in Figure 3.24 and Figure 3.25.

In order to more easily see how the relative noise level is changed after processing of the data, profile plots were made of the original data, as well as of the 2D- and 3D processed data by taking the maximum of the y-values covering the 4 mm hole for all x-values. The resulting

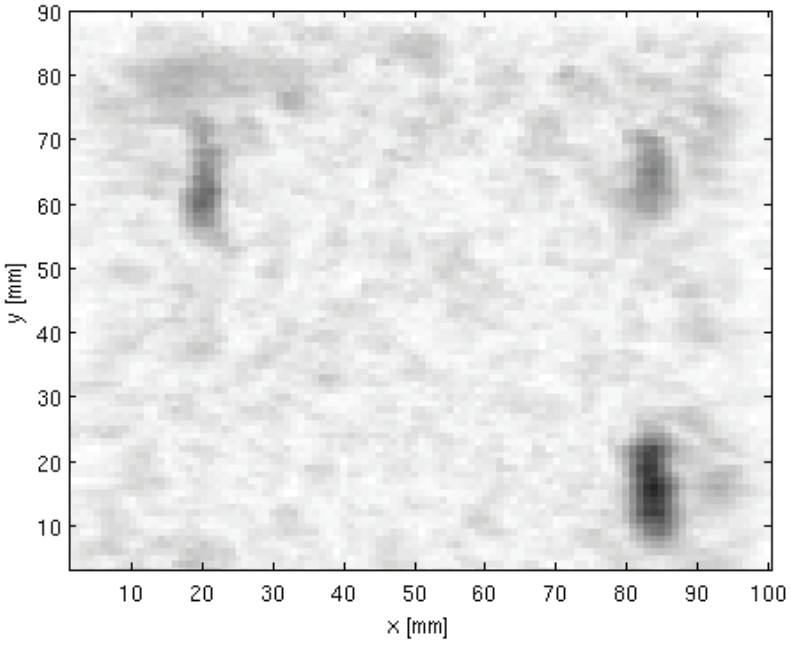

Figure 3.24: C-scan after 2D migration of data from the immersed copper block with FBHs.

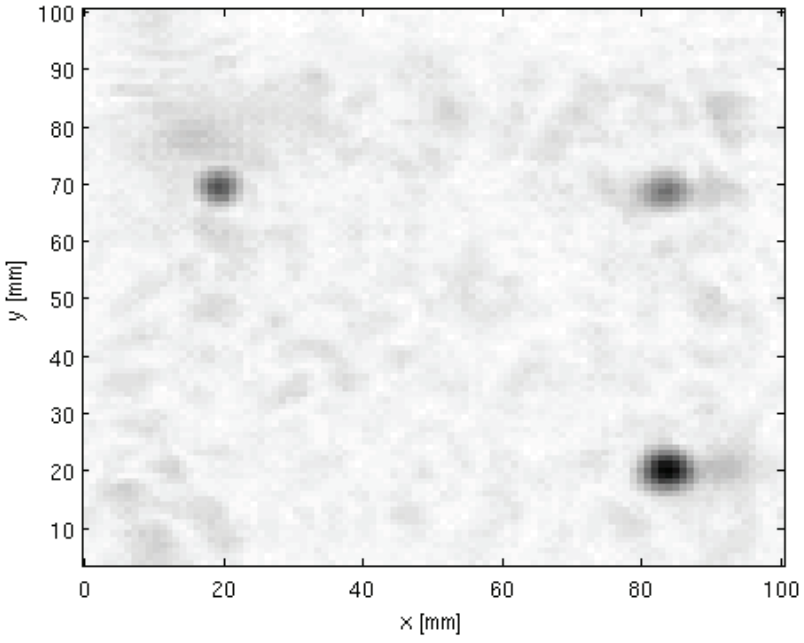

Figure 3.25: C-scan after 3D migration of data from the immersed copper block with FBHs.

plots are shown in Figure 3.26. It can be seen from the figure that the relative noise level drops from the original data to the 2D processed data, and drops further from the 2D processed data to the 3D processed data.

Table 3.4: The estimated halfpower resolution in x- and y-direction for FBHs in a copper block for the original data, and after processing with 2D and 3D phase shift migration. The theoretical resolution is 4.1 mm in both the x- and y-directions for the 3D processed data. For the 2D processed data this theoretical resolution holds only in the x-direction.

Hole	Original data		After 2D PSM		After 3D PSM	
	δ_x [mm]	δ_y [mm]	δ_x [mm]	δ_y [mm]	δ_x [mm]	δ_y [mm]
A: 3 mm	-	-	5.8	10	5.2	5.4
B: 2 mm	~ 15	~ 14	8.0	14.1	7	5.7
C: 1 mm	-	-	-	-	-	-
D: 4 mm	$\sim$17	$\sim$17	6.9	15.9	6.6	6.1

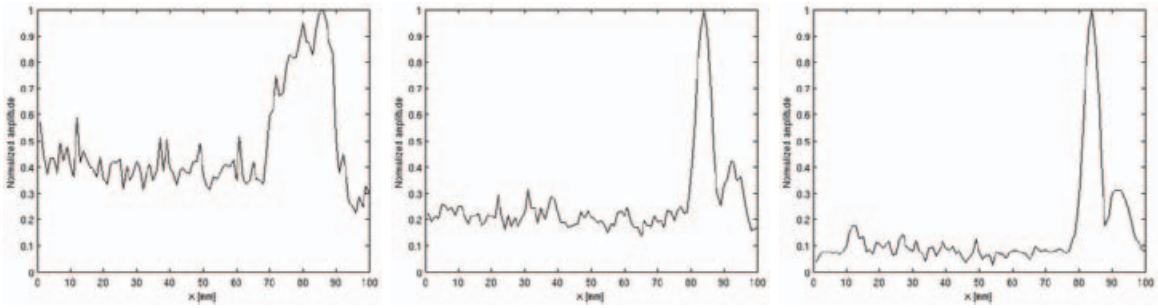

(a) The original data. (b) The 2D processed data. (c) The 3D processed data.

Figure 3.26: Profile plots of the 4 mm hole in the original data, the 2D processed data, and the 3D processed data.

Computational complexity

In a final experiment for the 3D algorithms, the computation times required by the two algorithms described in 3.2.2 were estimated and compared. All the processing for the 3D experiments presented earlier was performed using **Algorithm 1** on a high performance computer with a large internal memory. Unfortunately, this computer could not be used for an experimental examination on how the size of the data affects computation time, the reason being that other activity on the server disturbed the evaluation in an unpredictable way, making it impossible to compare the computation times from two different processings. Instead, the evaluation of computation times for the two 3D algorithms was made on a personal computer, with clock frequency 998 MHz, and 2.0 GB RAM. The performance of this computer was too poor to be able to run **Algorithm 1** with other than fairly small sets of data, which served little purpose. Therefore, the code was reduced to only contain a for-loop containing the critical, most time-consuming parts of the code[9], namely the phase shift in item 3a, as well as the summation over frequencies in item 3b. This reduced code could be run with larger sets of data. The same thing was done with the code for **Algorithm 2**, from which the nested for-loop was kept, with the code lines corresponding to item 2c.

The two reduced versions of the algorithms were run with dummy data, for a scenario that corresponds to a setup that takes measurements in a time interval between 25 and 53 μs, corresponding to 700 time samples at 25 MHz sampling. For a speed of sound of 4690 ms^{-1}, corresponding to copper, and a separation between depths cross-sections set to $\Delta z = 2 \cdot 10^{-4} m$, this corresponds to a reconstructed data volume of approximately 330 such cross-sections. The bandwidth of the pulses was set to 3.5 MHz.

The reduced version of **Algorithm 1** was empirically found to have a computation time that was approximately 60 % of the computation time for the whole algorithm for the same size of the data. In contrast, the reduced version of **Algorithm 2** had computation times that were approximately the same as those for the whole algorithm. Therefore, in order to be able to more fairly compare the computation times for the two algorithms, those from the stripped version of **Algorithm 1** were divided with 0.6.

Figure 3.27 shows the computation time as a function of the number of samples after zero-padding, $N_{x,zp}$ and $N_{y,zp}$, that, for simplicity, were set equal. The theoretical curves based on the discussion in section 3.2.2, with proportionality factors fitted to the experimental curves, are also plotted in the figure. The graph clearly shows that **Algorithm 1** outperforms **Algorithm 2** when it comes to computation time, and that there is a considerable difference in speed that grows fast with $N_{x,zp}$ and $N_{y,zp}$. Note, however, that **Algorithm 2** can be run on most commonly available computers, even for very large data sets.

We should note that at least **Algorithm 1** allows for a processing that can be made faster than the data acquisition for relatively large data sets. As a simple numerical example, with the data size parameters given above and for a scan over an area consisting of 100×100 scanning points, and assuming that zero-padding to about the double this data size in both x- and y- direction is required, we will get a processing time of approximately 3 minutes. The data acquisition time will be 10000 times the acquisition time of one A-scan. To compete with the processing time, we must acquire approximately 30 A-scans every second, which is somewhat unrealistic. This number should be compared to the acquisition time of about one second that the currently available equipment at our lab was capable of.[10]

[9] See section 3.2.2 for a discussion on asymptotical growth rates of the computation times.

[10] The main limiting factor is the mechanical scanner that is programmed to stop at every acquisition point. By allowing for measurements with a moving transducer, the acquisition time can be reduced significantly but will most probably still not be small enough to result in an overall acquisition time that is smaller than the processing

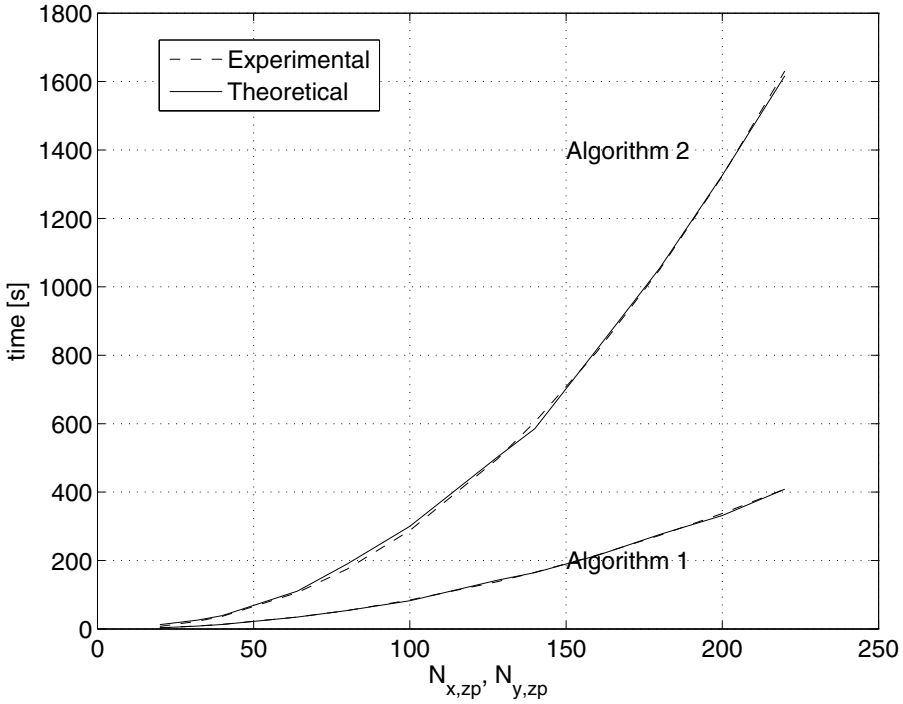

Figure 3.27: Theoretical and experimental plots of the calculation times for **Algorithm 1** (the lower curve) and **Algorithm 2** (the upper curve), as a function of $N_{x,zp}$ and $N_{y,zp}$ when $N_t = 700$.

3.2.4 Summary and discussion on 3D phase shift migration

In this section we have described how the phase shift migration can be used on 3D data sets and we have presented two alternative algorithms for doing this. **Algorithm 1** is suitable for high-performance computers and **Algorithm 2** is suited for computers with less internal memory. We should note that one obvious generalization of the work present here would be to combine the best of the two algorithms in the way that we iterate over the frequency components, as in **Algorithm 2**, but instead of only one component at a time, we use small bands and sum over all the frequency components in this band before performing the time consuming 2D Fourier transform, as is done in **Algorithm 1**. Although we have not implemented this, it is fairly obvious that this would give an algorithm with a performance somewhere in between the two algorithms that allows for trading smoothly between memory requirements and processing time and, thus, providing an algorithm that can be an optimized for the computer that is currently available for the user.

We have experimentally verified that the 3D algorithms, as expected, yield a resolution improvement in both x- and y-directions, compared to the improvement in a single direction which is the case for 2D reconstruction. Although we have not provided any detailed theoretical analysis of the expected resolution for the immersion case, which should take into account refraction effects and angle dependent transmission losses, we have seen that the resolution obtained in the experiments are well in agreement with the theoretically predicted resolution for the less general case of imaging of homogeneous isotropic media.

We have also noted that the theoretical resolution is only obtained when the targets are further away from the transducer than the nearfield/farfield limit. For targets residing in the nearfield, we typically should expect somewhat worse resolution than this.

---

time.

Since the resolution is determined by the aperture size, we should expect to obtain better resolved images by simply decreasing the diameter of the transducer. Of course, such improvement comes at a price. First, by making the transducer smaller we also obtain weaker signals and, thus, become more sensitive to electrical noise. This can be fought by using coded excitation techniques as described in [26] but this requires more advanced equipment that is capable of exciting the transducers with arbitrary waveforms. Second, by reducing the size of the transducer, we also need to reduce the scanning step in order to avoid spatial aliasing and this may lead to impractically long data acquisition times when scanning large areas.

3.3 Extension to array data

In Sections 3.1 and 3.2, phase shift migration was applied to monostatic data. The migration concept can also be carried over to multistatic data, i.e., data acquired using an array. The main benefit of using arrays is the increased coverage due to the parallel reception at several elements and, thus, a potentially increased data acquisition speed.

Array systems allow for flexible acquisition of ultrasonic data and the traditional use of phased arrays is to use electronic steering at transmit to create narrow beams, and dynamic focusing, or delay-and-sum, in receive to sequentially image the ROI, sector by sector. However, the method for acquiring data that is suitable for a subsequent processing using phase shift migration differs from this. Instead of focusing in transmit, we sequentially transmit a wide beam at one element at a time and receive at all array elements. For an array consisting of N_{tr} array elements, such a measurement results, in its most complete form, in a data set consisting of N_{tr} B-scans, each of size $N_t \times N_{tr}$, where N_t is the number of time samples. This so-called *full array data set* is then used for reconstructing a ROI beneath the array. Note, however, that such a full data set is not necessarily required for the reconstruction; using a subset of this may be sufficient and this will result in less computation as well as acquisition time. The cost of reducing the size of the data set will be poorer signal to noise ratio and potentially worse resolution.

We should note that, although this data acquisition mode differs from the traditional angle sweep, the full array data set contains all the information necessary to emulate the such a sweep of beams with focusing both in transmit and receive by post-processing the data. This can be done using the so-called synthetic transmit aperture (STA) technique, which is a delay-and-sum based method, described earlier in [26]. In fact, the phase shift migration algorithm for processing array data presented here share some similarities with STA. Note once again though that delay-and-sum is straightforward only for isotropic and homogenous objects but becomes cumbersome to use in cases when refraction is present, such as, in immersion tests, and this is the motivation for instead using phase shift migration.

The steps necessary to adapt phase shift migration to array data are described below in Section 3.3.1. A few experiments illustrating the concept are presented in Section 3.3.2 and conclusions and a discussion are given in Section 3.3.3

3.3.1 Phase shift migration for array measurements

Migration using a full array data set is in the geophysical community called *pre-stack migration* and numerous different versions and implementations of pre-stack migration have been proposed, see e.g. [27, 28]. It has also been adopted to the radar community and the version used here is based on the work presented in [29], which concerned ground penetrating radar. Migration using array data is somewhat more complicated than using monostatic data. Since the waves in the array case are transmitted and received at different positions, the exploding reflector model can no longer be used to simplify the theoretical development and wavefield extrapolation is required for both the received field and for simulating the transmitted field.

Compared to the version presented in [29], the version presented here has been somewhat modified to treat the problem of sound speed variations and refraction in a consistent way, by making use of frequency domain wavefield extrapolation both at transmit and receive.[11]

To develop the phase shift migration for a full array data set, let us first consider a single

[11] In the work presented in [29], time domain techniques were used for finding the forward propagation delays that are necessary in the imaging condition described below.

array B-scan obtained by transmitting only at the i:th element in the array and receiving with all elements. In radar terminology this is called a common-shot measurement and, as described in [29], the reconstruction of an image line in the ROI, using this single B-scan only, is obtained by extrapolating the measured field to the depth of interest, and applying an image condition to this extrapolated field. As described below, both these steps differ somewhat from those for the monostatic case.

Consider again the layered media illustrated in Figure 3.1, and suppose that the array is placed with elements regularly spaced in the x-direction at the level $Z_0 = 0$. Let $p(x, i, Z_0, t)$ denote the received field originating from the i:th transmission. As a preprocessing step, this field should have been correlated with the transducer element impulse response to compensate for undesired phase delays, c.f. Section 3.1.2. This preprocessed field can then be extrapolated to some arbitrary depth, z, residing in layer l, by first transforming the field to the (k_x, ω)-domain, yielding $P_1(k_x, i, \omega)$, and computing

$$P(k_x, i, z, \omega) = P_1(k_x, i, \omega)\alpha_l(k_x, z - Z_{l-1}, \omega) \prod_{q=1}^{l-1} \alpha_q(k_x, d_q, \omega), \tag{3.40}$$

where $\alpha(\cdot)$ now is defined as

$$\alpha_l(k_x, \zeta, \omega) = e^{-j\zeta\sqrt{\frac{\omega^2}{c_l^2} - k_x^2}}, \tag{3.41}$$

where, as in Section 3.1.2, c_l is the sound speed within the l:th layer. Note that, in contrast to the field extrapolation for the monostatic case, the array measurement can be considered as a direct field measurement, with no need to make the exploding reflector analogy. This means that the true sound speed should be used, and not the half speed.

$P(k_x, i, z, \omega)$ can be transformed back to the space-time domain by an inverse 2D Fourier transform to yield $p(x, i, z, t)$, which is the reflected field that would, hypothetically, be measured at an array placed at depth z resulting from a transmission at element i.[12] The imaging condition for the common-shot case is somewhat more complicated than for the monostatic case since it must take into account the propagation delay between the transmitter and the scatter of interest. If a point-like scatterer is present at depth z, the reflected field measured at the same depth would be optimally focused at this scatterer. However, if we define $t = 0$ as the time of array element excitation, the scattered field would appear after a time, $\tau(x, i, z)$, that corresponds to the propagation delay between the transmitter and the scatterer. As a consequence, the imaging condition relevant to the common-shot case is $t = \tau(x, i, z)$ rather than $t = 0$, and the read-out of an image line at depth z from the extrapolated field should be

$$Im(x, i, z) = p(x, i, z, \tau(x, i, z)), \quad \text{for all } x \text{ along the line at depth } z. \tag{3.42}$$

This can be computed in the frequency domain as

$$Im(x, i, z) = \int\int P(k_x, i, z, \omega) \exp(jk_x x) \exp(j\omega\tau(x, i, z)) dk_x d\omega. \tag{3.43}$$

By processing the B-scans separately, we obtain one reconstructed image for each transmission, $i = 1...N_{tr}$, and the final image recovered using the full array data set is then obtained by simply superimposing these images, which is in close analogy to the STA technique.

Note that, due to the delay $\tau(x, i, z)$ that depends on the x-position, the expression in eq. (3.43) cannot be efficiently computed for all x-positions along one image line using the IFFT

[12] Physically, this field would be a superposition of the incident and the reflected field. Recall, however, that we here only restrict our attention to the up-going waves, i.e., the reflected field.

as was the case for monostatic data. Instead, it must be computed separately for each x. For this reason, it is very difficult, perhaps even impossible, to implement phase shift migration for array data in a way that is as efficient as for monostatic data.

This far, we have not considered the problem of finding the delays $\tau(x, i, z)$ required in the processing. For a homogenous isotropic medium, these are trivial to compute but since our considered scenario involves refraction, and since one of the main reason for using phase shift migration in the first place was to avoid difficulties in computing propagation delays for such a scenario, the implementation of the above imaging condition should preferably be solved in an alternative way.

We here propose one such alternative that makes use of wave field extrapolation in a very similar form as that used in the phase shift migration, to compute the field arising from the transmitting array element. It is based on the following observation: For an impulsive excitation of the transducer array element, i, the observed field at a point (x, z), often referred to as a *spatial impulse response*, will essentially be a sharp pulse arriving after a propagation delay, $\tau(x, i, z)$, and by correlating this impulse with the migrated field at the point of interest, we obtain essentially the same effect as compensating the extrapolated field for this delay.

Say that the spatial impulse response at a point (x_m, z), resulting from an excitation at element i, is $p^{tr}(x_m, i, z, t)$. Then the correlation between the spatial impulse response and the extrapolated received field at the same point can be written as the time convolution

$$p_{corr}(x_m, i, z, t) = p^{tr}(x_m, i, z, -t) * p(x_m, i, z, t) \tag{3.44}$$

and the imaging condition consists, after the delay compensation, of reading out the delay compensated field, $p_{corr}(x_m, i, z, t)$ at $t = 0$.

The compensation and imaging condition steps can be performed in the frequency domain as, c.f., eq. (3.13),

$$P_{corr}(x_m, i, z, \omega) = \int [P^{tr}(x_m, i, z, \omega)]^* P(x_m, i, z, \omega) d\omega, \tag{3.45}$$

where superscript * denotes the complex conjugate.

The wave field extrapolation for computing the spatial impulse responses is nothing but a wave field simulation, and the only differences between this simulation and the extrapolation used for the received field are that we here consider down-going instead of up-going waves and that the boundary condition is different. In this case this condition consists of a field $p^{tr}(x, i, Z_0, t)$ that is zero for all x except for an impulse at $t = 0$ at the position of element i. The only consequence of considering down-going instead of up-going waves is that the phase shift factor will have a positive sign instead of the negative sign in eq. (3.41), which means that the simulation can be performed using the complex conjugate of the same phase factor $\alpha_l(\cdot)$ that is used in the extrapolation of the received field.

In summary, the simulation of the field at (x, z) can be performed as follows:

1. Fourier transform $p^{tr}(x, i, Z_0, t)$ with respect to x and t to obtain $P_1^{tr}(k_x, i, \omega)$.
2. Extrapolate the field to z by a multiplication with the corresponding phase shift factor as

$$P^{tr}(k_x, i, z, \omega) = P_1^{tr}(k_x, i, \omega) \alpha_l^*(k_x, i, z - Z_{l-1}, \omega) \prod_{q=1}^{l-1} \alpha_q^*(k_x, d_q, \omega). \tag{3.46}$$

3. The impulse responses for all point on a line at depth z are obtained by performing an inverse Fourier transform with respect to k_x:

$$P^{tr}(x, i, z, \omega) = \int P^{tr}(k_x, i, z, \omega) \exp(jk_x x) dk_x. \tag{3.47}$$

The above presented way of implementing the simulation of the transmitted field allows for a relatively efficient processing all B-scans along with the field simulations. First we note that the phase factor used in the processing of the common-shot B-scans are identical for all $i = 1...N_{tr}$; there is no dependence on transmitter element i in $\alpha(\cdot)$. Furthermore, there is a shift invariance in the x-direction in the simulation of the transmitted field in the sense that the simulated field at x_k, resulting from an excitation of element i, is identical to the field observed at x_{k+m}, resulting from an excitation of element $i + m$, provided that the image grid in x has the same resolution as the element spacing in the array.

We can now summarize the proposed algorithm, which combines the simulation of the transmitted field and the wave field extrapolation of the received field. We consider a general case where we use only a subset $i \in I$ of the transmissions for the reconstruction. The reconstructed image is then obtained as follows:

1. Initialize the transmitted field $p^{tr}(x, i_{sim}, Z_0, t)$ with all zeros, except for an impulse at the x-position for some arbitrarily chosen array element, i_{sim}. For all $i \in I$, initialize $p(x, i, Z_0, t)$ as the preprocessed common-shot B-scans, corresponding to the ith transmission.

2. Compute $P_1^{tr}(k_x, i_{sim}, \omega_s)$, assuming excitation at some arbitrary array element, i_{sim}, as

$$P_1^{tr}(k_x, i_{sim}, \omega_s) \leftarrow \mathrm{FFT}_{xt}\left\{p^{tr}(x, i_{sim}, Z_0, t)\right\}. \tag{3.48}$$

   and $P_1(k_x, i, \omega_s)$ for all $i \in I$ as

$$P_1(k_x, i, \omega_s) \leftarrow \mathrm{FFT}_{xt}\left\{p(x, i, Z_0, t)\right\}. \tag{3.49}$$

3. If the first z-value in the ROI is $z_{min} \neq 0$ and belongs to the l:th layer, extrapolate the fields so that when the iteration over z^p starts, the initial z-value is z_{min}. The calculations should be done for triplets (ω_s, k_x, k_y) that satisfy $\frac{4\omega_s^2}{c_l^2} - k_x^2 - k_y^2 \geq 0$:

$$P(k_x, i, z_{min}, \omega_s) = P_1(k_x, i, \omega)\alpha_l(k_x, z_{min} - Z_{l-1}, \omega_s) \prod_{q=1}^{l-1} \alpha_q(k_x, d_q, \omega_s) \tag{3.50}$$

   for all $i \in I$ and do the same for the simulated transmitted field:

$$P^{tr}(k_x, i_{sim}, z_{min}, \omega_s) = P_1^{tr}(k_x, i_{sim}, \omega_s)\alpha_l^*(k_x, z_{min} - Z_{l-1}, \omega_s) \prod_{q=1}^{l-1} \alpha_q^*(k_x, d_q, \omega_s) \tag{3.51}$$

4. Set $z^1 = z_{min}$ and do the following for all image lines $p = 1 \ldots N_z$:

   (a) Prepare for the imaging condition by first applying the inverse FFT to the received extrapolated fields:

$$P(x_m, i, z^p, \omega_s) \leftarrow \mathrm{IFFT}_{k_x}\left\{P(k_x, i, z^p, \omega_s)\right\} \tag{3.52}$$

   for all $i \in I$, yielding values for all m. Similarly, for the transmitted field

$$P^{tr}(x_m, i_{sim}, z^p, \omega_s) \leftarrow \mathrm{IFFT}_{k_x}\left\{P^{tr}(k_x, i_{sim}, z^p, \omega_s)\right\} \tag{3.53}$$

(b) Apply the imaging condition for all m:

$$Im(x_m, i, z^p) = P_{corr}(x_m, i, z^p, t = 0) = \sum_s [P^{tr}(x_{m'}, i_{sim}, z^p, \omega_s)]^* P(x_m, i, z^p, \omega_s), \tag{3.54}$$

where $m' = m - i + i_{sim}$.

(c) Compute fields at the new depth, z^{p+1}, by applying phase shifts:

$$P(k_x, i, z^{p+1}, \omega_s) = P(k_x, i, z^p, \omega_s)\alpha_l(k_x, \Delta z, \omega_s) \tag{3.55}$$

and

$$P^{tr}(k_x, i_{sim}, z^{p+1}, \omega_s) = P^{tr}(k_x, i_{sim}, z^p, \omega_s)\alpha_l^*(k_x, \Delta z, \omega_s) \tag{3.56}$$

where $\Delta z = z^{p+1} - z^p$.

5. Sum over $Im(x_m, i, z^p)$ to obtain the final reconstruction result for depth z^p:

$$Im(x_m, z^p) = \sum_{i \in I} Im(x_m, i, z^p). \tag{3.57}$$

3.3.2 Array experiments

The copper block with side drilled holes used earlier in Sections 3.1.3 and 3.2.3 was used also for the illustration of the phase shift migration array and the experiments were performed a 32 element array. The properties of the array placed some constrains on what kind of experiments could be performed and before presenting the experiments we therefore describe the array and explain the restrictions in some more detail in the subsection below. This is followed by an step-by-step illustration of the algorithm and a comparison of the results obtained with different subsets of a full array data set. Finally, the reconstruction results from a longer section of the copper block are presented.

The array properties

In the experiments, a 3.5 MHz, 32 element array from Imasonic was used. The array's strip like elements has an inter element pitch of 1 mm and 0.15 mm inter element spacing and the strips have length 20 mm and are cylindrically focused with a radius 45 mm. The array geometry is shown in Figure 3.28

This array has not been developed with synthetic aperture applications in mind and this limited somewhat what experiments could be performed. The main limitation is the cylindrical focusing and the experiments should preferably be performed with the scatterers residing not too far away from the focal zone, which is at about 45 mm in water. Otherwise, we will obtain reconstructed images that are unnecessarily blurred. If we take into account that the focal depth decreases in a situation when the sound enters an object with higher sound speed, the measurements must be performed with the array quite close to the test block to have the geometrical focus at least a few millimeters inside copper.[13] However, by doing this we obtain a strong secondary echo that has traveled between the array and the front surface twice. This echo will mask echoes arriving at about the same time and, since it arrives relatively early, this may limit the available size of the ROI.

[13] As a rule of thumb, every depth unit in the faster material should be counted a factor c_2/c_1 larger, where c_1 and c_2 are the sound speeds in the slow and the fast material, respectively. For instance, focusing 10 mm inside copper using a transducer focused at 45 mm in water, requires us to place the transducer at approximately 15 mm above the surface since the 10 mm in copper is counted approximately as 30 mm.

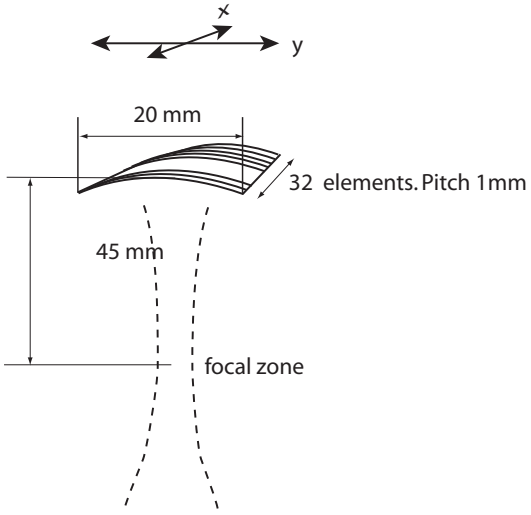

Figure 3.28: Illustration of the array used in the experiments.

Another issue that should be mentioned is that the array is spatially under-sampled, i.e., the element spacing is larger than required by the Nyquist criterion. As a consequence, the array will have grating lobes and we may experience spatial aliasing if there are interfering targets in these grating lobe directions. Note though, that if we actively avoid having targets residing in these directions, the spatial aliasing can be avoided.

Finally, an analysis of the theoretical resolution is more complicated in the array case than in the monostatic case. This resolution depends both on the receiving and transmitting apertures, where we in the latter case mean the set of transmitting elements used to create the data. In STA, an analysis using the so-called *effective aperture* is usually made, see [26] for a description of this. It is unclear, however, that this analysis technique of using the effective aperture is applicable to phase shift migration reconstructions in general. The curved elements of the array further complicates the analysis and we here simply leave out a theoretical analysis of the resolution and restrict our attention to a limited empirical examination. Without the theoretical analysis, we note though, see Appendix 3.A.3, that the theoretical resolution of a single focused array B-scan is approximately equal to the element width, which is twice as much as the theoretical resolution in the monostatic case. We should expect the final resolution to be in the neighborhood of this.

Algorithm illustration

The first experiment serves to provide some intuitive understanding of the algorithm by showing a number of partial results in the sequence leading to the reconstructed image. The illustration is made using a full array data set acquired above two of the SDHs residing at depths 16 and 20 mm below the front surface.

The data set from the copper block is visualized in Figure 3.29. The two SDHs are seen very faintly as hyperbolas that extend laterally over approximately 20 mm.

The B-scans presented in Figure 3.29 represent different field measurements and, as an illustration, these are extrapolated down to 20 mm inside the copper block which is at the same depth as the rightmost hole. The extrapolated fields are presented in Figure 3.30. The extrapolation corresponds to focusing and we see that the responses from the holes are far better

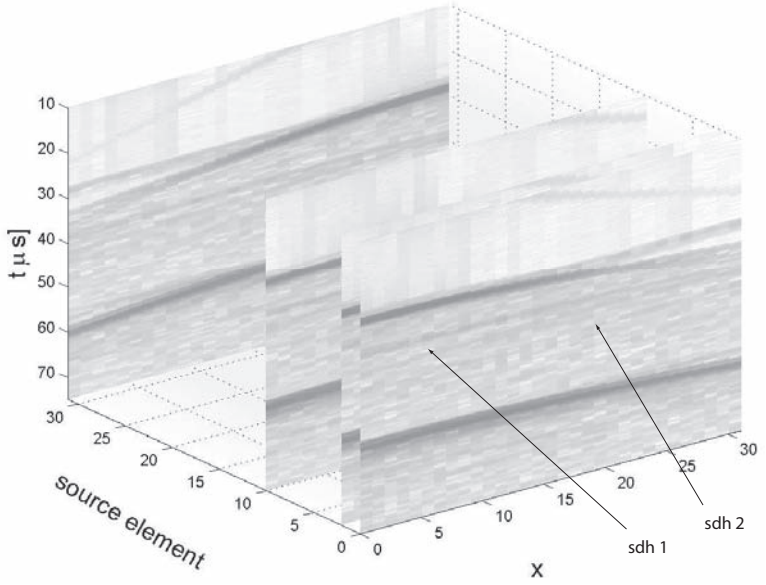

Figure 3.29: Visualization of a full array data set acquired using a 32 element array. The elements are fired one by one, resulting in a set of common-shot B-scans. The B-scans obtained from firing elements $i = 0$, 2, 10, and 31 are shown

concentrated than in the raw data. Note however that no imaging condition has yet been applied to these extrapolated fields.

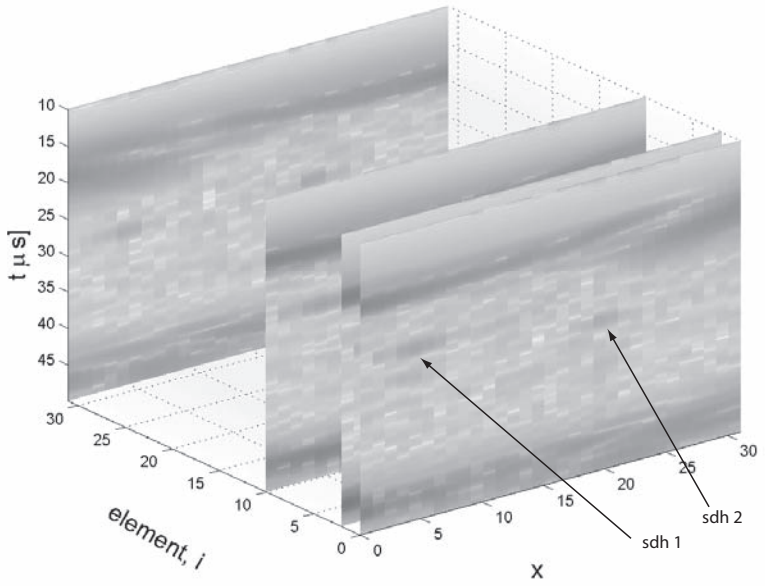

Figure 3.30: The array B-scans extrapolated to the depth 20 mm inside the copper block. The data is presented in the same way as in Fig. 3.29.

The fields are sequentially extrapolated to the different depths in the ROI and the imaging condition is applied, i.e., the fields are correlated with the respective simulated fields from the transmitting element, i, and the result at $t = 0$ are read out. In this way we obtain the partial reconstructed images, one for each i. These are shown in Figure 3.31.

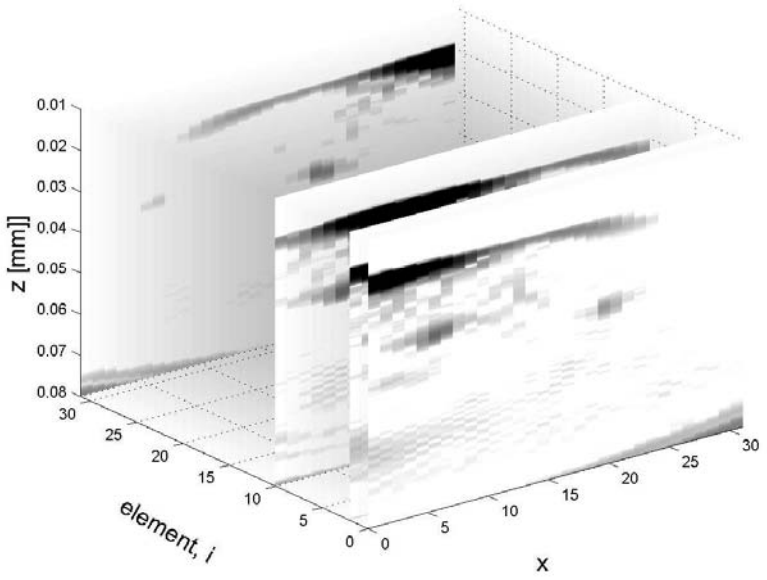

Figure 3.31: The reconstructed images obtained by applying the image condition to all points in the ROI, for each common-shot B-scan.

Note that the all these 32 reconstructed images are geometrically correct in the sense that the SDHs appear at the correct (x, z) coordinates. However, since the response from a target in general is strongest when the transmitting element is close, the relative strength of the SDHs are different in the different images. This is particularly apparent for the front surface that shows a very strong contribution at x close to the transmitting element.

By superimposing these partial images we obtain the final reconstructed image that is presented in Figure 3.32. Due to the superposition, the above mentioned differences in strengths

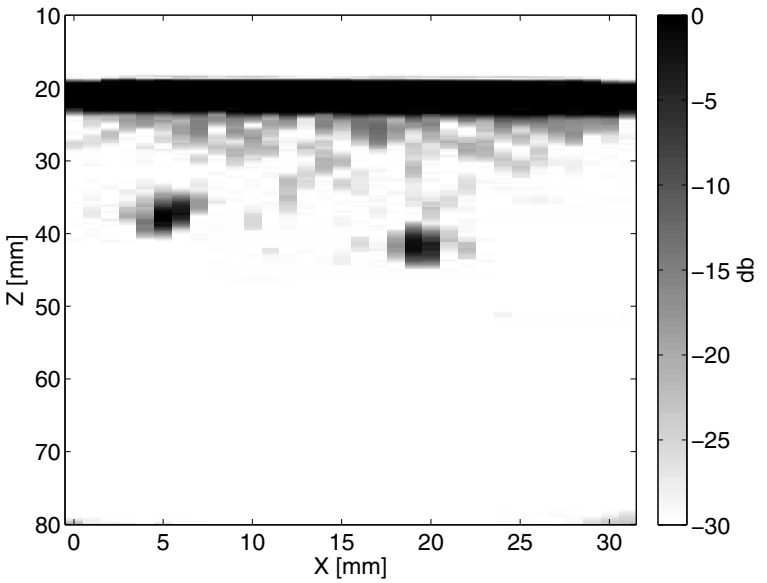

Figure 3.32: The final migrated image obtained by superimposing the results presented in Figure 3.31.

between results from different transmission are averaged out and the result is an image that fairly well represent the reflectivity of the targets in the medium.

Reconstruction using subsets of the full array data set

As described in Section 3.3.1, the reconstruction can be performed using a subset of the received B-scans. The advantage of this is a reduced data acquisition as well as computation time but the cost is worse signal-to-noise ratio and, potentially, worse resolution. Here we examine the effect of using only a subset of the full array data set.

The comparison was done using the same data set as in the algorithm illustration. Figures 3.33 to 3.37 show the reconstruction results obtain using an decreasing amount of data, starting with every second transmission in Figure 3.33 to the extreme of using only the outermost elements, $i = 0$ and 31, in Figure 3.37. These images should also be compared to that in Figure 3.32, which is at the other extreme, i.e, a reconstruction obtained by using all transmissions.

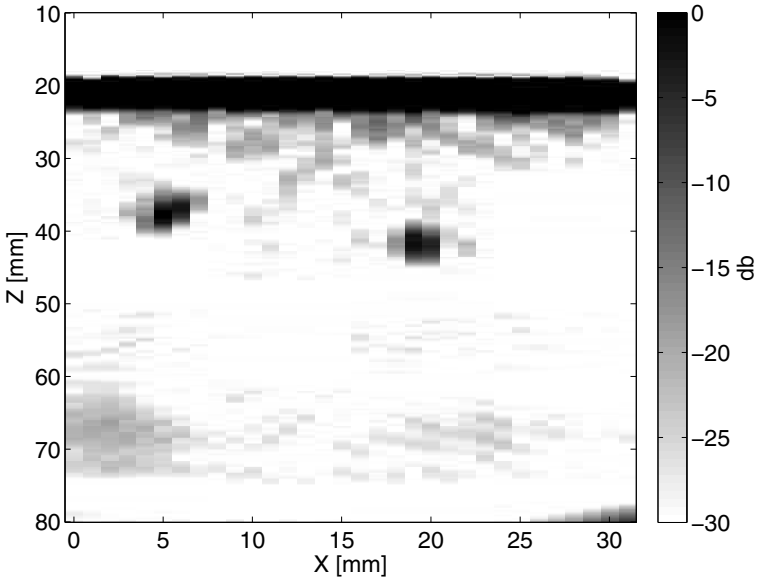

Figure 3.33: The reconstructed image using every second array B-scan in the full data set. Sixteen B-scans were used.

The intensities in the reconstructed images are shown in dB with their darkest point normalized to have 0 dB at the maximum amplitude at the leftmost hole. This normalization was done to get a fair comparison between the different levels of noise in the images.

We note that the reconstructed images get an increasing level of noise as the number of B-scans used for the reconstruction decreases. This would create difficulties when trying to detect weak targets. However, the resolution does not deteriorate in the same way and we appear to obtain images of approximately the same resolution regardless of the number of B-scans used. It is fairly similar for all reconstructed images, except for a slight deterioration for the last, in which only B-scans associated with the two outermost elements were used.

This is further verified in table 3.5, in which the average of the estimated half power resolution for the two holes is presented for the presented reconstructions. We note that the resolution is somewhat larger than the element width.

A full reconstruction of the copper block with SDHs

Finally, we present the reconstruction of a 125 mm long section of the copper block. The block was inspected with the array placed 20 mm above the block. With the restrictions caused by the array mentioned above, we chose to restrict our attention to only the upper part of the test

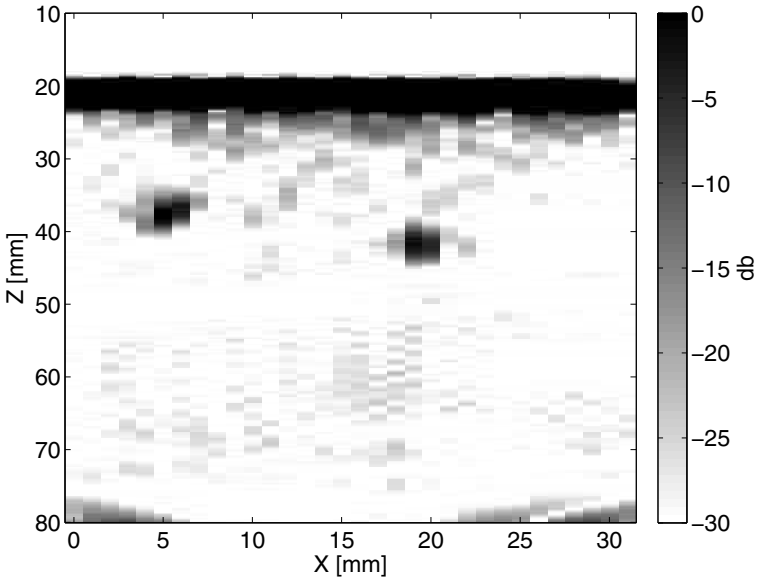

Figure 3.34: The reconstructed image using every third array B-scan in the full data set. Eleven B-scans were used.

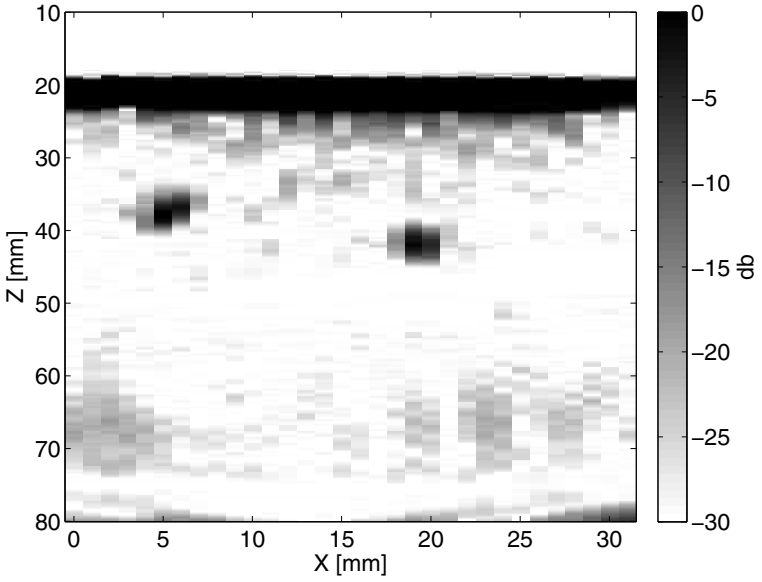

Figure 3.35: The reconstructed image using every fourth array B-scan in the full data set. Eight B-scans were used.

block. Since the array only covers 32 mm, several reconstructed images were used to build up the complete image. This was here done by performing a full array measurement every 12:th mm. The reconstruction of these yielded 32 mm long segments that were overlapping. For each x-position, the reconstruction corresponding to the array position that was most favorable was chosen for the building up of the final image. This array position was considered to be the one that had the particular x-position maximally centered under the array.

The reconstructed image obtained in this way is shown in Figure 3.38. In the figure we see eight of the overall 15 SDHs in the block. As mentioned above, the secondary reflection from the array masks the back surface echo. This secondary echo is what causes the strong indicating seen at $z = 80$ mm in the figure, not the back surface echo that should appear at about 94 mm

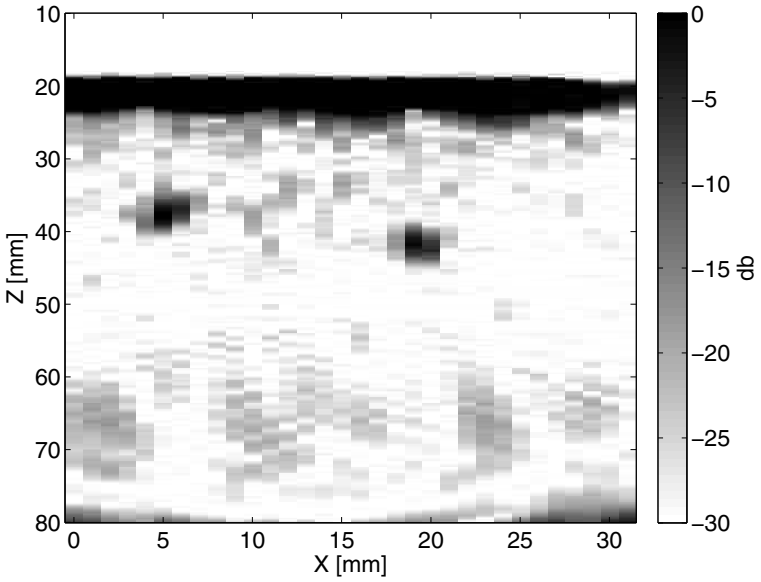

Figure 3.36: The reconstructed image using every eighth array B-scan in the full data set. Four B-scans were used.

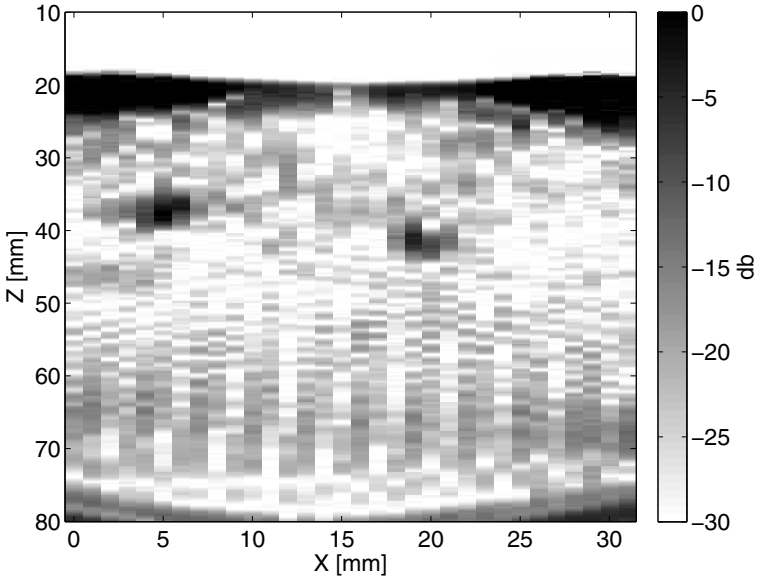

Figure 3.37: The reconstructed image using only the first and last array B-scan in the full data set. Two B-scans were used.

but that here was not included in the ROI.

The resolution of the holes can be further examined in the profile plot in Figure 3.39 and rough estimates of the half power resolution are presented in table 3.6. We note from the figure and the table that the resolution, in contrast to the results for the monostatic case, deteriorates as the depth increases. As discussed above, this is most probably caused by the fixed geometrical focusing in the y-direction, causing the more deeply buried targets to become more blurred since they are far away from the geometrical focus. We also note that the resolution of the uppermost SDHs, which are those closest to the geometrical focal point, is approximately the same as the array element width.

Table 3.5: Average of estimated halfpower resolution in x-direction for the reconstructed SDHs in a copper block, each 1 mm in diameter. The processing was performed with different subsets of the common-shot B-scans

Separation between transmitting elements [mm]	Average resolution after PSM δ_x [mm]
1	2.0
2	1.9
3	1.9
4	1.9
8	1.9
31	2.3

Table 3.6: Estimates of halfpower resolution in x-direction for side drilled holes in a copper block, each 1 mm in diameter, after processing with array phase shift migration using full array data sets.

Hole number	Resolution after PSM $\delta_x[mm]$
1	1.5
2	1.8
3	1.9
4	2.5
5	2.2
6	2.6
7	2.3
8	2.5

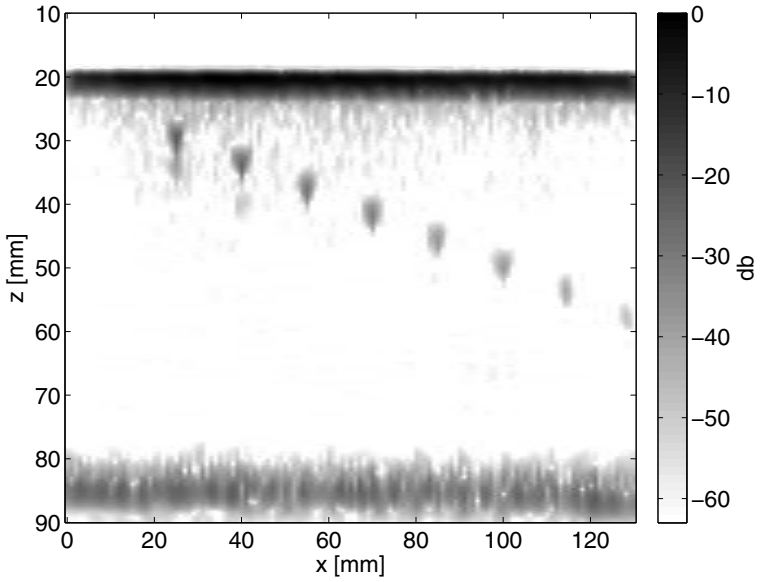

Figure 3.38: The reconstructed image from the copper block array data set. The image has been obtained by contatenation from a number of overlapping reconstructions using full array data sets.

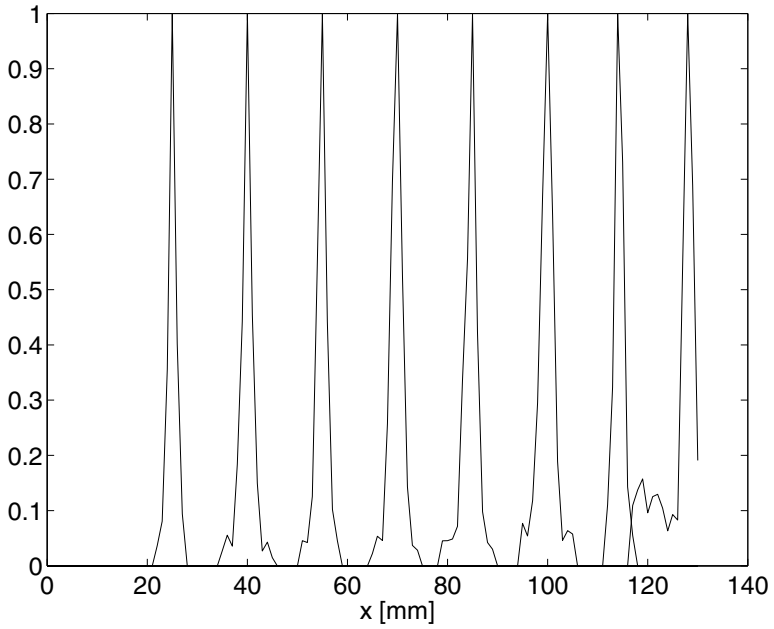

Figure 3.39: Profile plots from the holes in the reconstructed image from the copper block array data set.

3.3.3 Conclusions and discussion

We have shown how to extend the concept of phase shift migration to treat also data acquired using an array, thus enabling focusing through refracting layers and we have shown that the proposed method can yield reconstructed images with a resolution that is in the order of the element width.

The presented implementation uses frequency domain wave field extrapolation to handle both the extrapolation of the received fields as well as to implement the imaging condition. Despite the extensive use of FFTs, and the fact that the method makes efficient reuse of the

computed phase shift factors, the method is quite computationally demanding. In contrast to the monostatic case, for which the time bottle-neck is the data acquisition, the phase shift migration for arrays at this stage requires more time[14] than the data acquisition will require for a system that is dedicated for the considered measurement mode. As an example, the reconstruction of the 32 channel full array data set used in the illustration of the algorithm was performed in approximately two minutes.

We should note though that code has not been carefully optimized and we expect to be able to gain some factor in performance if such an optimization is performed. Note also that the algorithm is well suited for parallel processing, meaning that a significant increase in speed should be possible if the algorithm is implemented on a parallel computer or utilizing a graphical processing unit.

[14]This holds if computations are performed on a standard computer.

3.4 Robustness to non-horizontal front surfaces

All versions of phase shift migration presented in this chapter share a common problem that may cause the resulting images to have poorer quality than necessary. The problem is associated to the fact that phase shift migration, in its basic form, requires the sound speed to be a function of depth only. As a consequence, the data must be acquired along a line that is parallel to the front surface of the test object. Otherwise, since depth is measured in the normal direction from the scanning axis, this requirement of the sound speed being constant in the lateral direction will be violated.

The reconstruction results are sensitive to such tilts and it may unfortunately be difficult in practical applications to avoid some slight tilting. Moreover, tilted front surfaces may occur by necessity if we have large objects with slightly curved surfaces. In such a case, we can divide the data set into smaller sections, in which the surfaces can be well approximated as being planar, and process these separately. For a curved object, some of the sections will however be tilted with respect to the scanning plane.[15]

The problem is illustrated in Figure 3.40 that shows a scenario with a tilted test object and an example of the sound speed at a distance to the scanning axis that is between the minimum and maximum distances to the front surface. Because of the tilt, there is a step change in the sound speed for x between the scanning end points and the sound speed obviously depend on both z and x.

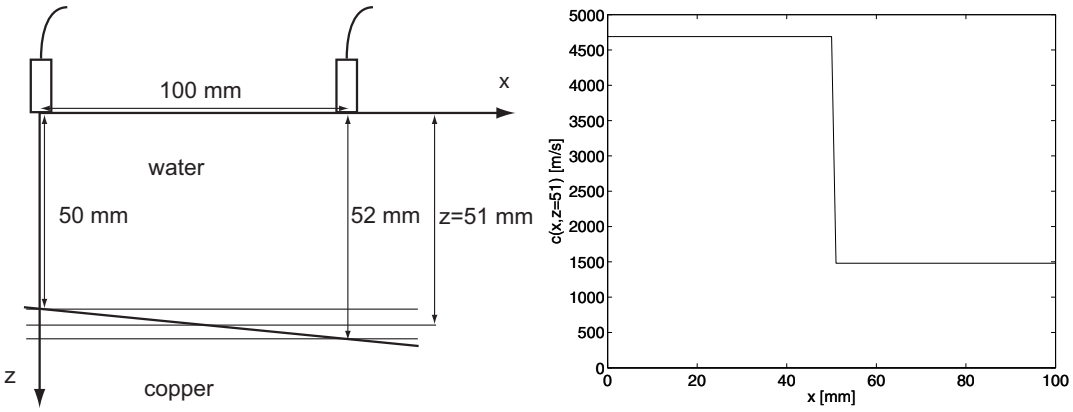

(a) (b)

Figure 3.40: (a) A scenario with a tilted test block. The depth measured from the scanning axis is 50 mm and 52 mm at the beginning and end points of the scan, respectively. (b) The sound speed as a function of x at the depth $z = 51$ mm.

Regardless of the cause of the tilted surfaces, it is important to have means to treat it. Modified versions of phase shift migration have been developed to treat more general cases with the sound speed varying with both x and z [20, 30]. These methods rely however on the sound speed being a smooth function of x and they are therefore not appropriate for this scenario. Here we instead propose to solve the problem using the same wave field extrapolation technique that is the basis for phase shift migration.

The idea is to extrapolate the measured field to a set of new points placed on a line that is parallel to the front surface of the object. This transformed data set fulfils the required assumptions of the front surface and scanning plane being parallel, and standard phase shift

[15] This is of course provided that the scan is performed along a straight line, which is to prefer here since phase shift migration is based on such a linear scan.

migration can subsequently be applied to this data.

In the presentation below, we only consider the tilt compensation for the case of 2D reconstruction using monostatic data, but the concepts can be straightforwardly extended both to 3D and to the array case. In Section 3.4.1, the problem is outlined in some more detail and the solution based on wave field extrapolation is presented. In Section 3.4.2, an experiment illustrating the concept is presented and conclusions and a discussion are finally given in Section 3.4.3.

3.4.1 Problem description and a solution through wave field extrapolation

Consider a transducer that is scanned along the x-direction at depth $z = 0$, with a scanning step Δx. The scan is performed over an object with a planar surface that is tilted with an angle θ relative to the scanning line.

As mentioned above, the idea is to compensate for the tilt by extrapolating the measured field to a set of new positions that are placed on a line that is parallel to the object's front surface. In other words, we wish to express the field in a new, rotated, coordinate system. The scenario is depicted in Figure 3.41 in which the original coordinate system is indicated by x and z and the rotated system is indicated by x' and z'.

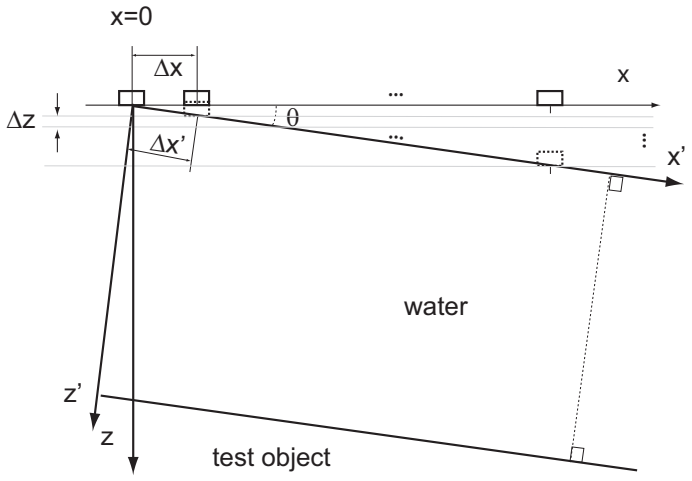

Figure 3.41: A scan over an object with a non-horizontal front surface.

The original scanning positions are found at the N_x positions (x_i, z_i) for $i = 0...N_x - 1$ where $z_i = z_0 = 0$ and with x_i given by

$$x_i = i\Delta x. \tag{3.58}$$

The position to which we wish to extrapolate the field are, expressed in the original system, (x_i^{new}, z_i^{new}) with $x_i^{new} = x_i$ and z_i^{new} given by

$$z_i^{new} = i\Delta z \quad \text{where } \Delta z = \Delta x \tan\theta. \tag{3.59}$$

In the rotated system, these points are expressed as (x_i', z_i') with $z_i' = 0$ for all i and with

$$x_i' = i\Delta x', \quad \text{where } \Delta x' = \frac{\Delta x}{\cos\theta}. \tag{3.60}$$

For an acquired B-scan, represented by $p(x_i, z_0, t)$, the perhaps most straightforward way to find the extrapolated field at these points is to apply the wave field extrapolation as described

in Section 3.1.2, repeatedly with a Δz-step in depth and, for each iteration, compute the field by an 2D inverse Fourier transform to obtain the field at depth z_i^{new} and then extract the field at x-coordinate x_i^{new}. Let $\tilde{p}(x_i', z_i', t)$ denote the compensated field expressed in the rotated coordinate system. We obtain this field for all x_i' and z_i' as follows:

1. Since the first A-scan position requires no extrapolation, we simply store $\tilde{p}(x_0', z_0', t) = p(x_0, z_0, t)$.

2. Perform a 2D Fourier transform of the measured field with respect to x and t:

$$P(k_x, z_0, \omega) \leftarrow \mathrm{FFT}_{xt}\left\{p(x, z_0, t)\right\}. \tag{3.61}$$

3. For $i = 1...N_x - 1$:

   (a) Compute $P(k_x, z_i^{new}, \omega)$ through the phase shift

$$P(k_x, z_i^{new}, \omega) = P(k_x, z_{i-1}^{new}, \omega) \exp\left(-j\Delta z\sqrt{\frac{4\omega^2}{c^2} - k_x^2}\right), \tag{3.62}$$

   for $\omega < 0$ and $k_x^2 < \frac{4\omega^2}{c^2}$. Set the remaining components to zero. Note that (i) the field extrapolation is carried out for one medium only, typically water, so we need to consider only one sound speed, c and (ii) the phase shift factor is the one used for monostatic data. For array data, we should instead use the exponent $\left(-j\Delta z\sqrt{\frac{\omega^2}{c^2} - k_x^2}\right)$.

   (b) Compute $p(x_k, z_i^{new}, t)$, for all k, by a 2D inverse Fourier transform

$$p(x_k^{new}, z_i^{new}, t) \leftarrow \mathrm{IFFT}_{k_x,\omega}\left\{P(k_x, z_i^{new}, \omega)\right\} \quad \text{for all } k, \tag{3.63}$$

   and store $\tilde{p}(x_i', z_i', t) = p(x_i^{new}, z_i^{new}, t)$.

This preprocessing results in a B-scan that is compensated for the tilt angle, θ and phase shift migration can be applied straightforwardly on this B-scan. We should note though that we in this migration must use $\Delta x'$ as the scanning step and that the image grid at the reconstruction is defined in the rotated coordinate system.

In practice, the angle θ can typically be estimated from the raw data, manually or automatically, by detecting the arrival times of the front echo at, say, the starting and ending points of the scan. Let these arrival times be denoted by t_{start} and t_{end}, respectively. Then it can be shown from simple geometrical arguments that θ can be estimated as

$$\theta = \arctan\left(\frac{c(t_{end} - t_{start})}{2(N_x - 1)\Delta x}\right). \tag{3.64}$$

3.4.2 Illustration of the tilt compensation concept

To illustrate the concept, we again used the copper block with SDHs that was used in several earlier presented experiments. The block was tilted approximately 2^o with respect to the scanning axis as illustrated in Figure 3.42. The acquired data, which is presented in Figure 3.43, was compensated as described above, where θ was estimated by eq. (3.64) to be 1.98^o. This compensated B-scan is presented in Figure 3.44.

The resulting reconstructed image obtained by applying phase shift migration on the compensated data is shown in Figure 3.45. This image can be compared to the results obtained from the same, but non-tilted, block. We see that the reconstructed image shows very little difference from the image in Figure 3.46 that was reconstructed under such more ideal conditions.

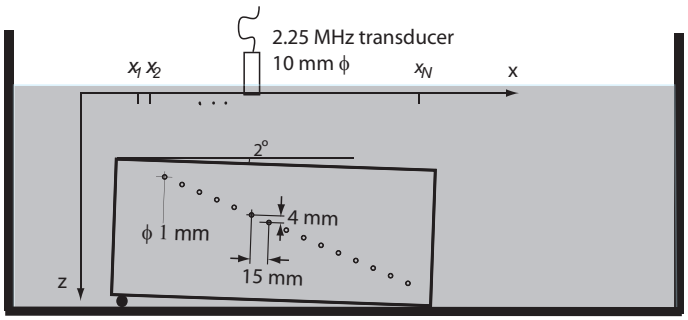

Figure 3.42: Setup for the experiment from the tilted copper block.

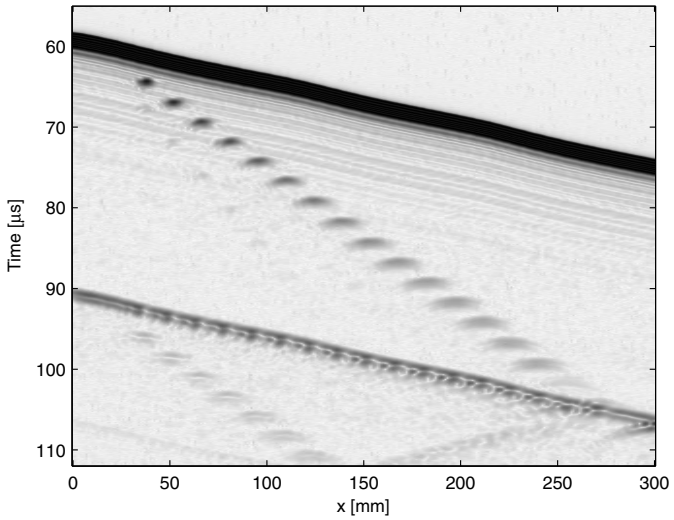

Figure 3.43: The raw data from a slightly tilted block.

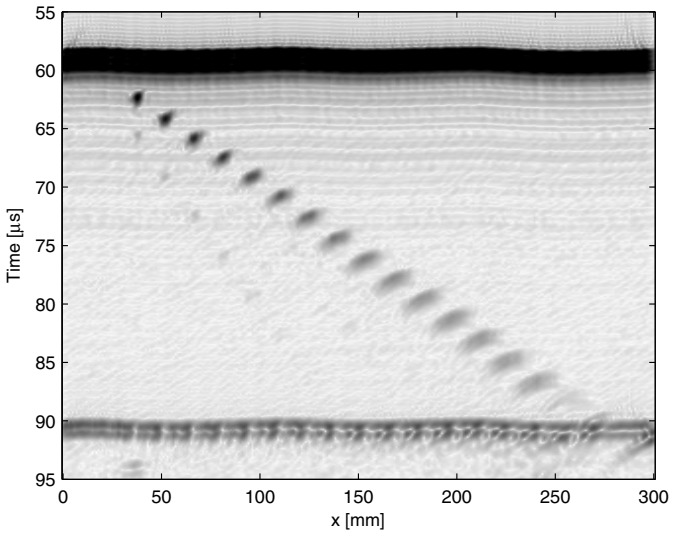

Figure 3.44: Data that has been compensated for the tilt using wave field extrapolation.

3.4.3 Discussion

In this section we have presented a method for compensation for objects having front surfaces that are tilted relative to the scanning axis. This compensation has the benefit of providing

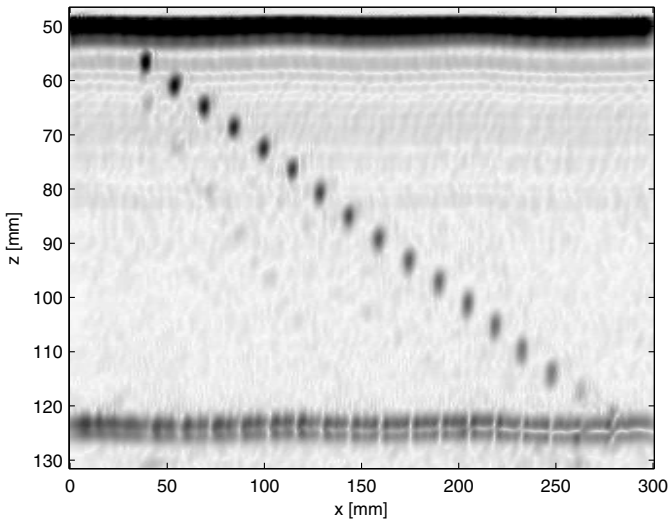

Figure 3.45: The results of phase shift migration applied to tilt compensated data.

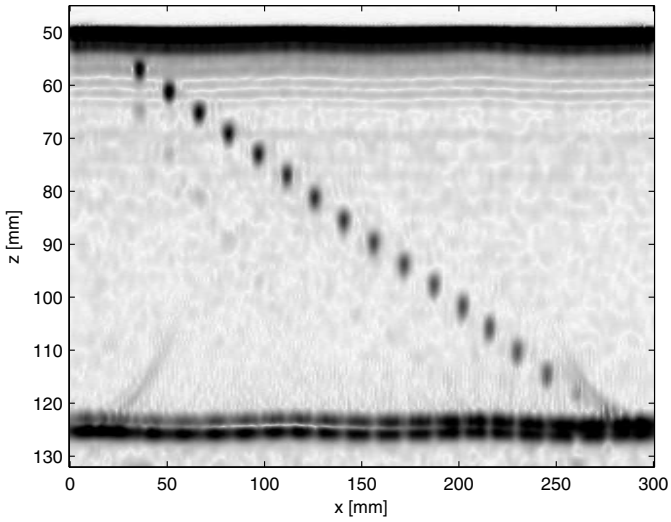

Figure 3.46: The results of phase shift migration applied to data from the non-tilted block.

data that can be processed straightforwardly using phase shift migration. Front surfaces that are tilted may occur either through simple misplacement of the object or because of processing of sections of data acquired from large objects that have slightly curved surfaces.

Although we have an accurate method for performing the compensation, it is still to be recommended to avoid such tilts as far as possible. One reason for this is that the method requires some additional processing time. Another reason is that the risk of experiencing spatial aliasing increases with increasing θ. One contributing factor is the slight increase in spatial sampling step when going from Δx to $\Delta x'$. In most cases this is however a minor contribution. More importantly, the compensation transforms the data into a B-scan that can be interpreted as having been acquired along a line parallel to the front surface, but using a transducer that is tilted by θ relative the object's front surface. As discussed in Appendix 3.A.4, a transducer with finite aperture acts as a spatial lowpass filter, suppressing the plane wave components with high spatial frequency, k_x. Such components corresponds to plane waves with high frequency, ω, arriving at the transducer from a large incidence angle. By tilting the transducer, the suppression

of these components will becomes less pronounced for waves arriving from the transducer beam direction and this will increase the risk of spatial aliasing.

Bibliography

[1] T. Stepinski (editor), M. Engholm, and T. Olofsson. Inspection of copper canisters for spent nuclear fuel by means of ultrasound. Technical report, 09-28. Department of Engineering Sciences, Uppsala University, 2009.

[2] D. W. Prine. Synthetic aperture ultrasonic imaging. In *Proc. Eng. Appl. of Holography Symp.*, pages 287–288. SPIE, July 1972.

[3] R. C. Fairchild, B. H., Anderson, and J. R. Frederick. Synthetic aperture ultrasonic inspection of pressure vessels and piping. *American Society of Mechanical Engineers*, (77-PVP-23):8 –, 1977.

[4] K. Nagai. Fourier domain reconstruction of synthetic focus acoustic imaging system. *Proceedings of the IEEE*, 72(6):748 – 749, 1984.

[5] K.J. Langenberg, M. Berger, T. Kreutter, and K. Mayer. Synthetic aperture focusing technique signal processing. *NDT International*, 19(3):177–189, June 1986.

[6] K. Mayer, R. Marklein, K.J. Langenberg, and T. Kreutter. Three-dimensional imaging system based on fourier transform synthetic aperture focusing technique. *Ultrasonics*, 28(4):241 – 255, 1990.

[7] L.J. Busse. Three-dimensional imaging using a frequency-domain synthetic aperture focusing technique. *IEEE Transactions on Ultrasonics, Ferroelectrics, and Frequency Control*, 39(2):174 – 179, 1992.

[8] Z. D. Qin, A. Tauriainen, J. Ylitalo, E. Alasaareal, and W. Lu. Frequency Domain Compensation for Inhomogeneous Layers in Ultrasound Holography. *IEEE Transactions on Ultrasonics, Ferroelectrics and Frequency Control*, 36(1):73–79, Jan 1989.

[9] R. Stolt. Migration by fourier transform. *Geophysics*, 43(1):23–48, Feb 1978.

[10] T. Stepinski. An implementation of synthetic aperture focusing techniques in frequency domain. *IEEE Trans. on Ultrasonics, Ferroelectronics and Frequency Control*, 54(7):1399–1408, July 2007.

[11] S.R. Doctor, T.E. Hall, and L.D. Reid. Saft-the evolution of a signal processing technology for ultrasonic testing. *NDT International*, 19(3):163 – 7, 1986.

[12] E. Wennerström and T. Stepinski. Model-based correction of diffraction effects of the virtual source element. *IEEE Transactions on Ultrasonics, Ferroelectrics, and Frequency Control*, 54(8):1614 – 1622, August 2007.

[13] J. A. Johnson and A. Barna. The Effects of Surface Mapping Correction with Synthetic-Aperture Focusing Techniques on Ultrasonic Imaging. *IEEE Transactions on Sonics and Ultrasonics*, SU-30(5):283–294, Sept 1983.

[14] H. G. Kraus. Generalized synthetic aperture, focused transducer, pulse-echo, ultrasonic scan data processing for non-destructive inspection. *Ultrasonics*, 21(1):11 – 18, Jan 1983.

[15] A. Shlivinski and K.J. Langenberg. Defect imaging with elastic waves in inhomogeneous-anisotropic materials with composite geometries. *Ultrasonics*, 46(1):89 – 104, 2007.

[16] M.T. Taner and F. Koehler. Velocity spectra—digital computer derivation and applications of velocity functions. *Geophysics*, 34(6):859–881, December 1969.

[17] M. A. Haun, D. L. Jones, and W. D. O'Brien Jr. Adaptive focusing through layered media using the geophysical "time migration" concept. In *Proc. of the IEEE Ultrason. Symp.*, volume 2, pages 1635 – 1638, 2002.

[18] J. Gazdag. Wave equation migration with the phase-shift method. *Geophysics*, 43(7):1342–1351, December 1978.

[19] J. F. Claerbout. *Imaging the Earth's Interior*. Blackwell Scientific Publications, 1985.

[20] J. Gazdag and P. Sguazzero. Migration of seismic data by phase shift plus interpolation. *Geophysics*, 49(2):124 – 31, Feb 1984.

[21] F. Bertora, P. Pellegretti, A. Questa, C. Parodi, and A. Trucco. An alternative frequency domain beamforming. In *Proc. of the IEEE Ultrason. Symp.*, volume 3, pages 1749 – 52, 2004.

[22] D. Loewenthal, L. Lu, R. Roberson, and J. Sherwood. The wave equation applied to migration. *Geophysical Prospecting*, 24(2):380 – 99, June 1976.

[23] W.A. Schneider. Integral formulation for migration in two and three dimensions. *Geophysics*, 43(1):49–76, February 1978.

[24] D. Cassereau, D. Guyomar, and M. Fink. Time deconvolution of diffraction effects-application to calibration and prediction of transducer waveforms. *Journal of the Acoustical Society of America*, 84(3):1073 – 85, Sept 1988.

[25] L.J. Cutrona. Comparison of sonar system performance achievable using synthetic aperture techniques with the performance achievable by more conventional means. *Journal of the Acoustical Society of America*, 58(2):336 – 48, 1975.

[26] T. Stepinski (editor), T. Olofsson, and E. Wennerstöm. Inspection of copper canisters for spent nuclear fuel by means of ultrasound. Technical report, 06-47. Department of Engineering Sciences, Uppsala University, 2009.

[27] C. P. A. Wapenaar, N. A. Kinneging, and A. J. Berkhout. Principle of prestack migration based on the full elastic two-way wave equation. *Geophysics*, 52(2):151 – 173, 1987.

[28] A. J. Berkhout. Pushing the limits of seismic imaging, part i: Prestack migration in terms of double dynamic focusing. *Geophysics*, 62(3):937–953, 1997.

[29] K. Gu, G. Wang, and J. Li. Migration based SAR imaging for ground penetrating radar systems. *IEE Proceedings: Radar, Sonar and Navigation*, 151(5):317–325, October 2004.

[30] P.L. Stoffa, J.T. Fokkema, R.M. de Luna Freires, and W.P. Kessinger. Split-step fourier migration. *Geophysics*, 55(4), April 1990.

[31] J. Krautkramer and H. Krautkramer. *Ultrasonic testing of materials*. Springer, 1990.

[32] M. Soumekh. *Synthetic Aperture Radar Signal Processing with Matlab Algorithms*. John Wiley & Sons, 1999.

3.A Appendix

3.A.1 Comments on transmission losses at layer interfaces

In the modeling, the transmission losses at the layer interfaces were neglected and this will cause errors in the computed field as it is backpropagated through an interface. We should note, however, that as long as the effect of the transmission loss can be well approximated by a constant scaling, independent of angle of incidence and, thus, independent of k_x, the resulting effect on the reconstructed image will merely be an amplitude scaling that will be constant within each layer. Such a scaling will not influence the lateral resolution.

As an example, the circular transducer used in the experiments presented in 3.1.3 had a diameter of $D = 10$ mm and a center frequency $F_c = 2.25$ MHz and bandwidth of approximately $\Delta F = 1.5$ MHz. Thus, the lowest frequency at which the transducer operated was 1.5 MHz which yields a maximum wavelength of approximately $\lambda = 1$ mm in water.

The divergence angle for a circular transducer is given by [31]

$$\theta_{div} = \arcsin\left(1.22\frac{\lambda}{D}\right). \tag{3.65}$$

From this we have that the maximum beam divergence is $\theta_{div} \approx 0.122$ radians or 7°. Thus, we know that the sound enters into the copper object with angle of incidence of at most 7°. The echo transmittances [31] for longitudinal-longitudinal waves at a water-copper interface calculated for angles between 0° and 7° vary between 0.1345 for 0° and 0.1286 for 7°. Thus, the difference is maximally 6% and we can safely approximate them as being constant for all angles of interest.

Furthermore, the echo transmittance for transversal waves appearing as a result of mode conversion at the boundary is less than 7% of the echo transmittance of longitudinal waves at 7° and approximately 3% at 4.7° which is the divergence angle at the center frequency. As a consequence, the contribution of the transversal waves to the final image will be very small and this motivates neglecting these waves in the processing.

3.A.2 Comments on the sign conventions for FFT:s and the use of standard software packages

The decomposition of a field into plane harmonic waves, which is the basis for the theory presented in this chapter, is usually written in physics literature as

$$p(x,z,t) = \int\int\int P(k_x,k_z,\omega)\exp(j(k_x x + k_z z - \omega t)dk_x dk_z d\omega, \tag{3.66}$$

if we consider a 2D scenario. $P(k_x,k_z,\omega)$ represents the complex amplitude of a plane wave traveling in the direction $\mathbf{k} = (k_x,k_z)$.

Physically this is a convenient decomposition because the exponential term describes in a straightforward way how a constant wave phase travels. Say, for instance, that $k_x = 0$ and $k_z > 0$. Then, for a positive ω and increasing t, the phase is constant, C, if $k_z z - \omega t = C$, or $z = (C + \omega t)/k_z$. Thus, z will increase with time, which is in accordance with having a positive k_z. Note that we would have the same traveling direction if we switch sign for both k_z and ω.

The transform treats both positive and negative values for ω so if we wish to consider planar wave going in only one direction we must ensure that the combination of signs for k_z and ω will give a correct wave traveling direction. We consider *up-going* wave, which with our definition

of coordinate system becomes waves in the *negative* z direction. A proper combination is then to choose $k_z < 0$ and $\omega > 0$.

The plane wave decomposition in eq. (3.66) is essentially an *inverse* Fourier transform that has a corresponding direct Fourier transform of the field with respect to x, z, and t, as

$$P(k_x, k_z, \omega) = \int\int\int p(x, z, t) \exp(-jk_x x) \exp(-jk_z z) \exp(j\omega t) dx dz dt. \tag{3.67}$$

Please note the difference between this definition of Fourier transform and the one that is used in several other application fields, in particular electrical engineering, and which is generally the basis for the corresponding numerical software for FFT:s. There, the Fourier transform of a general three-dimensional function, $f(x, y, z)$ is defined as

$$F(\Omega_x, \Omega_y, \Omega_z) = \int\int\int f(x, y, z) \exp(-j\Omega_x x) \exp(-j\Omega_y y) \exp(-j\Omega_z z) dx dy dz, \tag{3.68}$$

i.e., a negative sign is consistently used in complex exponential for all variables whereas in the plane wave decomposition, the time variable is treated differently.

Since the implementations used in this work uses standard matlab packages for computations of 2D or 3D FFT:s, the difference in sign convention must be accounted for. This has been done by simply, in the matlab implementation, using only the negative frequencies instead of the positive that are prescribed by the physics. This is the reason for seeing statements, such as, "the positive frequencies are nulled out" in Section 3.2.2. The positive frequencies there simply refer to the "physically negative"

3.A.3 Theoretical resolution

Here predictions of the theoretically achievable resolution are given, both for the z-direction and the x- and y-direction, although the resolution in the two lateral directions in this work are of more interest since this resolution is generally poorer than in the range direction. Note that the expressions presented here should only be seen as rules of thumb, since they are not always straightforwardly applicable for the experimental setup used in this work. There are some major differences between the theoretical assumptions used here and the experimental setup. First, there is an assumption that the speed of sound, c, is constant, which is only true if there is a homogeneous isotropic medium. In many of the experiments in this work, the measurements have been acquired using an immersion setup, with the speed of sound depending on depth. Second, there is an assumption that a single frequency is used in transmission, whereas in the experiment relatively wide band pulses have been used. Finally, the analysis leading to the estimates of the lateral resolution is based on an assumption that the scatterers are located in the far field of the transducer [10] and we should therefore not expect the results to hold in the near field. The nearfield/farfield limit is approximately given by [31]

$$z_{nf} = \frac{D^2 f}{4c} \tag{3.69}$$

where f is the frequency and c the sound speed.

As a rough estimate, the resolution in depth is proportional to the wavelength λ of the pulses:

$$\lambda = \frac{c}{f}, \tag{3.70}$$

where c is the speed of sound and f is the center frequency of the pulse. However, since we consider pulse-echo measurements, it is more relevant to consider the effective wavelength which

Table 3.7: Resolving power in depth in different materials.

Material	Speed of sound $[ms^{-1}]$	Resolving power $[m]$
Water	1480	$1.64 \cdot 10^{-4}$
Copper	4690	$5.21 \cdot 10^{-4}$
Aluminium	6330	$7.03 \cdot 10^{-4}$

is

$$\lambda_{eff} = \frac{c}{2f}, \tag{3.71}$$

where the division of the speed of sound by two corresponds to the waves traveling the double path. The resolving capacity in depth is half the effective wavelength, giving the final expression [19]

$$\delta_z = \frac{c}{4f}. \tag{3.72}$$

The pulses used in the experiments all had a center frequency of around 2.25 MHz, and inserting that in equation (3.72) together with the speed of sound for the different materials used, gives the resolution power in table 3.7. These measures gives a guiding line in how to choose the separation, Δz, between image lines/planes since there is no benefit of choosing it significantly smaller than the resolving power in depth.

The resolution in x- and y-direction in the monostatic case is derived from the resolution of a physical array the same size as the synthetic aperture. The synthetic aperture has two times finer resolution than the physical array, again because of halving the speed of sound, which gives the effective halfpower beamwidth of the synthetic aperture with length L_{eff} as [10]

$$\delta_{x,y} = \frac{R\lambda}{2L_{eff}}, \tag{3.73}$$

where λ is the wavelength and R is the distance of the scatterer from the synthetic aperture.

The synthetic aperture for a certain aperture is obtained as

$$L_{eff} = R\sin(\theta_{div}) \tag{3.74}$$

where θ_{div} is the divergence angle of the aperture.

For a transducer having a uniform 1D aperture of D, the divergence is given by

$$\theta_{div} = \arcsin(\frac{\lambda}{D}), \tag{3.75}$$

and for a uniform circular aperture we have the divergence given in eq. (3.65).

If we combine these divergence expressions with eqs. (3.74) and (3.73), we obtain

$$\delta_{x,y} = \frac{D}{2} \tag{3.76}$$

for the uniform linear aperture, which is the commonly used expression, and

$$\delta_{x,y} = \frac{D}{2 \cdot 1.22} \approx 0.41D \tag{3.77}$$

which is a modified expression for the uniform circular aperture.

Worth noting about the lateral resolution is that both δ_z and $\delta_{x,y}$ are independent of depth[16].

[16]This only holds if attenuation can be neglected.

3.A.4 Comments on the use of the discrete Fourier transform and aliasing

All Fourier transforms involved in the algorithm are performed using discrete data and the fast Fourier transform has been used for all calculations. Aliasing may then appear both spatially and temporally. Both the temporal and spatial sampling must fulfil the Nyquist criterion, stating that the sampling frequency must at least be twice that of the highest frequency component appearing in the signals. For the temporal sampling, this requirement is fulfilled with a large margin in all the experiments presented in the chapter. As an example, the experiments presented both in Section 3.1 and 3.2 were performed with a sampling frequency of 25 MHz whereas the center frequency of the transducer was 2.25 MHz and with a bandwidth of about 1.5 MHz.

The spatial sampling can be more critical. Let us here for simplicity consider the problem for the 2D case and consider the spatial coordinate x only.[17] In its conventional form, in which a a scenario with constant velocity and point-like transducers are considered, the spatial sampling theorem states that the distance between two sampling points on the x-axis, Δx, should be separated by no more than $\lambda_{min}/4$ for pulse-echo measurements, where λ_{min} is the minimum wave length appearing in the measurements. As an example: If we use a transducer with an upper frequency of 3 MHz for the measurements in water, having a velocity of 1500 m/s, we have that $\lambda_{min} = 0.5$ mm and $\Delta x < 0.125$ mm which is a quite small separation that will result in impractically long acquisition times if large areas are to be scanned.

The requirement $\Delta x < \lambda_{min}/4$ is, however, quite overpessimistic and does not take into account the transducer's directivity. If this is done, we arrive at the much less restrictive result [32], stating that when a transducer of aperture D is used, the spatial sampling must be performed at steps no longer than $\Delta x < D/4$. For a transducer of diameter 10 mm we thus have that $\Delta x < 2.5$ mm which is fulfilled in the experiments presented in Sections 3.1 and 3.2.

Aliasing can occur also at the inverse transform back to spatial coordinates. The Fourier coefficients represent a function that is periodic both in t and x, and especially the periodicity in the spatial coordinate may cause problems in the reconstruction. Let N_x denote the number of spatial samples taken in the x-direction, separated by Δx. Then an inverse transform back from the discrete Fourier domain is periodic with a periodicity $N_x \Delta x$, equal to the synthetic aperture. Phase shifts along x caused by the processing in the frequency domain then may wrap around to the opposite side of the resulting image. This will be particularly apparent if there is a strong reflector close to one of the endpoints of the scan. This wrap around effect can be avoided by zero-padding in the x-direction and we illustrate in Figures 3.47 and 3.48 how this is achieved and what amount of zero-padding that is necessary in order to do so.

Figure 3.47 illustrates a transducer with divergence angle θ_{div} that is scanned over a region of interest. Below the beginning point of the scan, a scatterer (A) is present at depth z_A. This scatterer will appear in the raw data as one half of a hyperbolic pattern, peaking exactly at the leftmost side of the B-scan and the extension of the right side of the hyperbola in the x-direction will be $z_A \tan \theta_{div}$. Consider now the reconstruction of another point (B) that is found on the same depth as (A) but on the opposite side of the ROI. In the processing for recovering the reflectivity of point (B), data is summed along a hyperbola that has a lateral extension determined by the divergence angle and depth, which is the same as for point (A).

The hyperbolic signature of (A) is indicated in Figure 3.48 as a solid line and the data that is used for reconstructing (B) is shown as a dashed line. Due to the processing being performed in the frequency domain, the summation along the dashed hyperbola will take place over a periodic continuation of the B-scan.[18] Without zero-padding, this summation will therefore

[17] The extension to 3D is straightforward; the problem of avoiding aliasing can be treated independently for x and y.

[18] The periodic continuation is in the figures shown only in the x-direction.

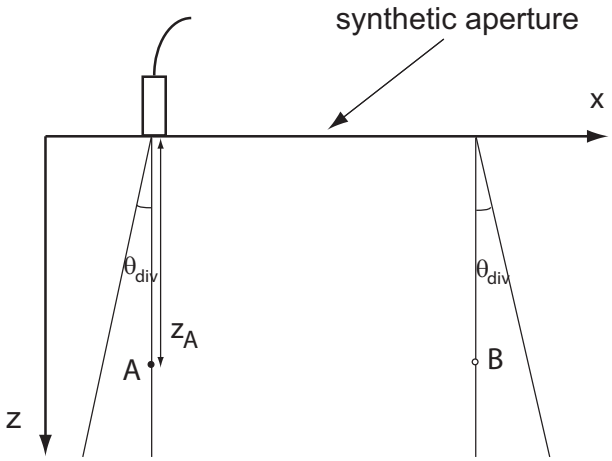

Figure 3.47: A transducer with divergence angle θ_{div} is scanned over a scatterer (A) just below the beginning point of the scan. The data from this scan is used for reconstructing an image of the region of interest. In particular, we consider the reconstruction of a point (B) which is on the opposite side of the scan and at the same depth.

wrap around and involve points along the hyperbola corresponding to (A). If we instead pad with $z_A \tan\theta_{div}/\Delta x$ columns of zeros, the summation over the part of the hyperbola not covered by the scan will take place over zeros only and will not contribute to the result.

We realize from the example illustrated in Figures 3.47 and 3.48 that the amount of aliasing caused by the processing in the frequency domain is depth dependent as is illustrated in Figure 3.49 and the zero-padding provides a margin. Since the required margin will depend on depth we should choose the margin for the worst case, which is for the deepest endpoint in the ROI. In this way we protect against aliasing for all depths. This is illustrated in Figure 3.50.

If we choose the ROI to have the same start and end point in the x-dimension as the scan and with z_{max} being the deepest point in the ROI, we will need a margin of $z_{max}\tan\theta_{div}$ to avoid aliasing and the minimum total size of the zero-padded data set in the x-direction will become

$$N_{x,zp} = \left\lceil N_x + \frac{z_{max}\tan\theta_{div}}{\Delta x} \right\rceil \tag{3.78}$$

where $\lceil . \rceil$ denotes the ceiling operator.

More generally, for a ROI of that has length W_x in the x-direction that is not equal to $N_x\Delta x$, it can be shown that the minimum $N_{x,zp}$ required to avoid aliasing is given by [29]

$$N_{x,min} = \left\lceil \frac{\frac{W_x}{2} + z_{max}\tan\theta_{div} + \frac{N_x\Delta x}{2}}{\Delta x} \right\rceil \tag{3.79}$$

Finally, we should not that the computational efficiency of the FFT is in general optimal for transforming sequences with lengths that are powers of 2. Therefore, the number of appended zeros should preferably be rounded up so that the overall number of samples after zero-padding becomes a power of 2.

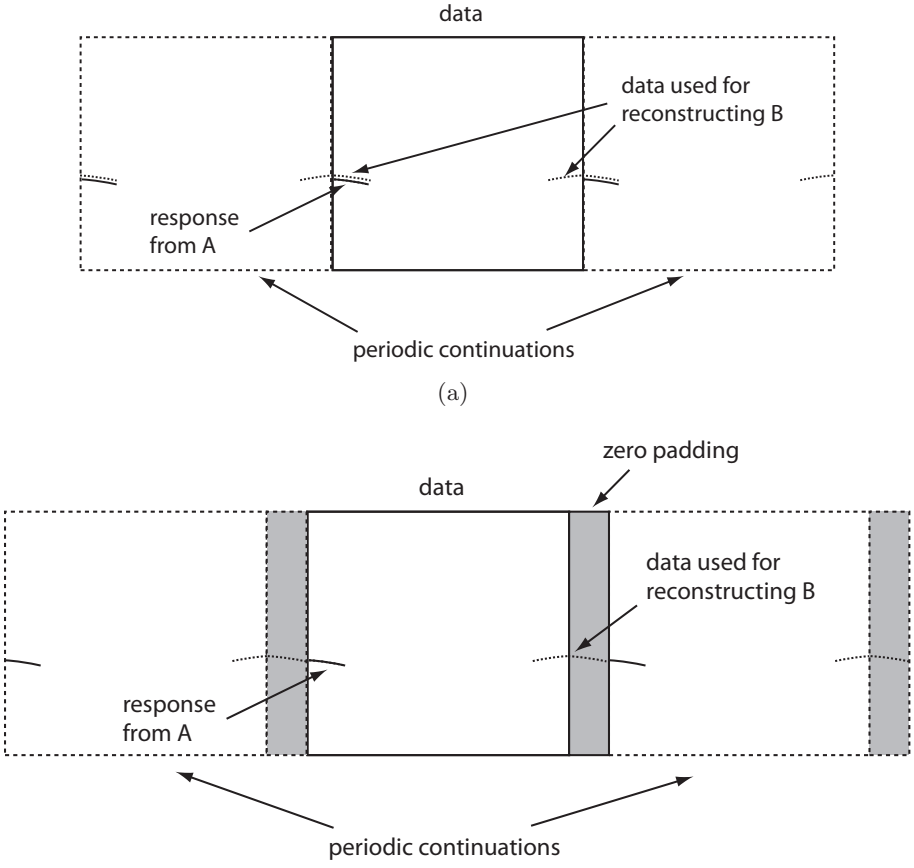

Figure 3.48: The periodic continuation of the B-scan acquired from the setup shown in Figure 3.47. The hyperbolic footprint of the scatterer (A) is shown solid and data along the hyperbola that is used in the reconstruction of (B) is shown as a dashed line. Due to the processing being performed in the frequency domain, the summation along the dashed hyperbola will take place over a periodic continuation of the B-scan. Without zero-padding as in (a), this summation will involve points along the (A) hyperbola. If we instead pad with $z_A \tan\theta_{div}/\Delta x$ columns of zeros, the summation over the part of the hyperbola not covered by the scan will take place over zeros only and will not contribute to the result.

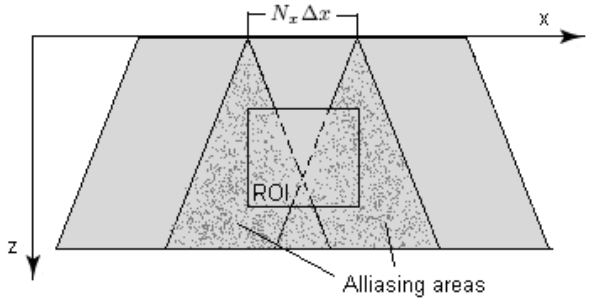

Figure 3.49: For data that is not zero-padded, aliasing will occur in the areas where periodic continuations of the fan-shaped insonified region overlap.

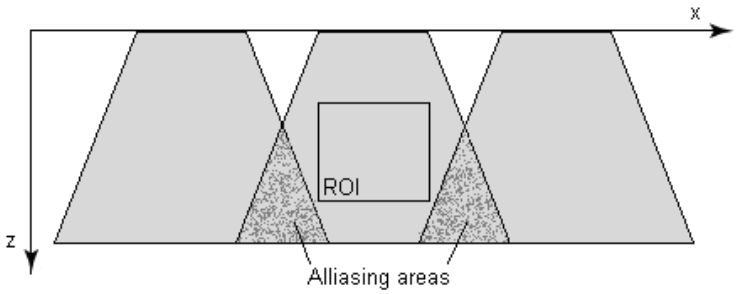

Figure 3.50: With enough zero-padding to avoid aliasing for the deepest positions, aliasing is avoided in the entire ROI.